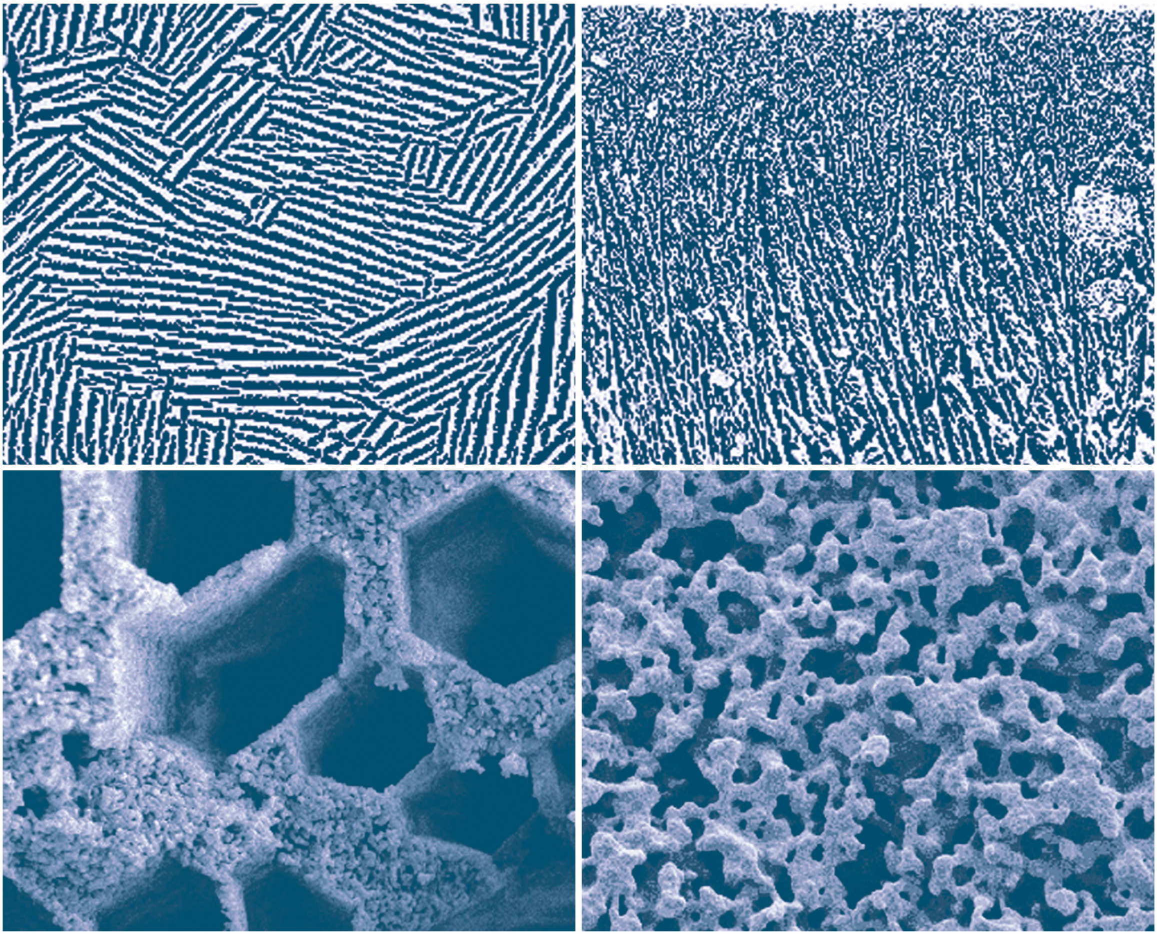

Thermomechanical Characterization of Advanced Ceramic Membrane Materials

Ying Zou

Energie & Umwelt / Energy & Environment
Band / Volume 404
ISBN 978-3-95806-288-7

Mitglied der Helmholtz-Gemeinschaft

JÜLICH
Forschungszentrum

Schriften des Forschungszentrums Jülich
Reihe Energie & Umwelt / Energy & Environment Band / Volume 404

Forschungszentrum Jülich GmbH
Institut für Energie- und Klimaforschung
Werkstoffstruktur und -eigenschaften (IEK-2)

Thermomechanical Characterization of Advanced Ceramic Membrane Materials

Ying Zou

Schriften des Forschungszentrums Jülich
Reihe Energie & Umwelt / Energy & Environment Band / Volume 404

ISSN 1866-1793 ISBN 978-3-95806-288-7

Bibliografische Information der Deutschen Nationalbibliothek.
Die Deutsche Nationalbibliothek verzeichnet diese Publikation in der
Deutschen Nationalbibliografie; detaillierte Bibliografische Daten
sind im Internet über http://dnb.d-nb.de abrufbar.

Herausgeber und Vertrieb: Forschungszentrum Jülich GmbH
Zentralbibliothek, Verlag
52425 Jülich
Tel.: +49 2461 61-5368
Fax: +49 2461 61-6103
zb-publikation@fz-juelich.de
www.fz-juelich.de/zb

Umschlaggestaltung: Grafische Medien, Forschungszentrum Jülich GmbH

Druck: Grafische Medien, Forschungszentrum Jülich GmbH

Schriften des Forschungszentrums Jülich
Reihe Energie & Umwelt / Energy & Environment, Band / Volume 404

D 82 (Diss., RWTH Aachen University, 2017)

ISSN 1866-1793
ISBN 978-3-95806-288-7

Abstract

Ceramic based oxygen transport membranes (OTM) have attracted much attention for alternative production concepts to generate high purity oxygen at low energy consumption, particularly if good thermal integration in high-temperature industrial process is realized. For a practical application relevant design, an asymmetric membrane consisting of a thin dense membrane layer supported by a porous substrate was in the focus of the current research. To ensure long-term operation and lifetime, the membrane must maintain both its mechanical stability and functional property. However, strength of the mechanically supporting substrate material usually decreases with increasing total pore volume even though high porosity may enhance the functional properties, such as permeability. Besides, differences in thermo-mechanical behavior, in particular creep, of dense and porous membrane material may also lead to structure instability. Hence, the main purpose of the present work is to study the porosity dependency of thermal-mechanical properties of selected oxygen transport membrane materials, and the mechanical compatibility of the porous / dense membrane layers in the asymmetric membrane design.

Due to its long-term chemical stability under application relevant environments along with good permeation values, the perovskite $La_{0.6}Sr_{0.4}Co_{0.2}Fe_{0.8}O_{3-\delta}$ (LSCF) was chosen as most suitable and furthermore, representative OTM material in this study. In particular, aiming towards an advanced characterization of different microstructures and potential associated effects onto thermo-mechanical behaviour, LSCF porous supports with different microstructures were produced by different synthesis methods, including dry pressing, tape- and freeze-casting. Elastic and plastic behaviour at room- and high-temperature were investigated with bending and compressive test setup, respectively, especially concentrating onto the anisotropic behaviour of freeze-casting materials and the ferro-elastic behaviour the rhombohedral phase. The results of porous samples were compared and discussed along with that of dense LSCF. In terms of materials stability, the apparent rhombohedral – cubic phase transition was investigated in detail with HT-XRD. In particular a potentially operation relevant surface degradation was observed and studied in further detail with respect to temperature and stress effects.

As an alternative substrate material, 3 mol% Y_2O_3 doped ZrO_2 (3YSZ) produced by freeze-casting and pressing & sintering was also investigated focusing onto the porosity dependency of mechanical behaviour. In fact, 3YSZ was chosen due to its high mechanical / chemical stabilities compared to other OTM materials. Overall, the effect of porosity (between 45% and 65%) and pore morphology (lamellar and spherical) on bending strength and gas permeability was investigated on the basis of 3YSZ.

Overall, the work for LSCF was mainly concentrated on the effect of the porous structures on the creep behavior; for 3YSZ was focused on the correlation of mechanical parameters and functionally important gas permeability. The combination of both studies offers a wider view, considering a broad range of mechanical properties from room temperature to application relevant temperatures, on the relationship between different pore arrangements and gas permeability which should be optimized to warrant a high permeation of the layered membrane arrangement.

Kurzfassung

Keramikbasierte Sauerstofftransportmembranen (OTM) haben als alternative Produktionskonzepte um bei niedrigem Energieverbrauch hochreinen Sauerstoff zu erzeugen viel Aufmerksamkeit erregt, insbesondere wenn eine gute thermische Integration im Hochtemperatur-Industrieprozess beabsichtigt wird. Für ein für praktische Anwendungen relevantes Design stand eine asymmetrische Membran, bestehend aus einer dünnen, dichten Membranschicht, die von einem porösen Substrat getragen wurde, im Fokus der aktuellen Forschung. Um langfristigen Betrieb und Lebensdauer zu gewährleisten, muss die Membran sowohl ihre mechanische Stabilität als auch ihre funktionelle Eigenschaft beibehalten. Jedoch nimmt die Festigkeit des mechanisch tragenden Substratmaterials gewöhnlich mit zunehmendem Gesamtporenvolumen ab, obwohl hohe Porosität die funktionellen Eigenschaften, insbesondere die Permeabilität, verbessern kann. Daneben können auch Unterschiede im thermomechanischen Verhalten, insbesondere Kriechen, von dichten und porösen Membranmaterialen zur Strukturinstabilität führen. Der Hauptzweck der vorliegenden Arbeit besteht daher darin, die Porositätsabhängigkeit von thermisch-mechanischen Eigenschaften ausgewählter Sauerstofftransport-Membranmaterialien und die mechanische Kompatibilität der porösen / dichten Membranschichten im asymmetrischen Membrandesign zu untersuchen.

Aufgrund seiner langzeitigen chemischen Stabilität unter anwendungsrelevanten Umgebungen mit guten Permeationswerten wurde der Perovskit $La_{0.6}Sr_{0.4}Co_{0.2}Fe_{0.8}O_{3-\delta}$ (LSCF) als am besten geeignet und weiterhin repräsentatives OTM-Material für diese

Studie ausgewählt. Insbesondere mit dem Ziel einer weiterentwickelten Charakterisierung unterschiedlicher Mikrostrukturen und potenziellen Wirkungen auf das thermomechanische Verhalten, wurden LSCF-poröse Träger mit unterschiedlichen Mikrostrukturen durch unterschiedliche Syntheseverfahren, einschließlich Trockenpressen, Band- und Gefrierguss, hergestellt. Das elastische und plastische Verhalten bei Raum- und Hochtemperatur wurde mit Biege- und Kompressionsversuchen unter Berücksichtigung des anisotropen Verhaltens von Gefriergusswerkstoffen und des ferro-elastischen Verhaltens der rhomboedrischen LSCF Phase untersucht. Die Ergebnisse der porösen Proben wurden mit denen des dichten LSCF verglichen und diskutiert. Weiterhin wurde der offenbar rhomboedrisch-kubische Phasenübergang des LSCF im Detail mit HT-XRD untersucht. Insbesondere wurde auch eine potenziell betriebsbedingte Oberflächenschädigung beobachtet und hinsichtlich Zusammenhang zwischen Temperatur- und Spannungseffekten näher untersucht.

Als alternatives Substratmaterial wurde zusätzlich auch 3 Mol-% Y_2O_3-dotiertes ZrO_2 (3YSZ), das durch Gefriergießen und Pressen & Sintern hergestellt wurde, mit der Fokussierung auf die Porositätsabhängigkeit des mechanischen Verhaltens untersucht. Hierbei wurde 3YSZ aufgrund seiner hohen mechanischen / chemischen Stabilität im Vergleich zu anderen OTM-Materialien gewählt. Insgesamt wurde dabei die Auswirkung der Porosität (zwischen 45% und 65%) und der Porenmorphologie (lamellar und sphärisch) auf Biegefestigkeit und Gaspermeabilität ermittelt.

Insgesamt konzentrierte sich die Arbeit für LSCF vor allem auf den Effekt der porösen Strukturen auf das Kriechverhalten; im Fall von 3YSZ lag der Fokus auf der Korrelation von mechanischen Parametern und funktionell wichtiger Gaspermeabilität. Die Kombination beider Studien bietet eine erweiterte Betrachtung unter Berücksichtigung einer breiten Palette von mechanischen Eigenschaften von Raumtemperatur bis zu anwendungsrelevanten Temperaturen, insbesondere hinsichtlich der Beziehung zwischen verschiedenen Porenanordnungen und der Gaspermeabilität, die optimiert werden sollte, um eine hohe Permeation der Schichtmembrananordnung zu gewährleisten.

Acknowledgements

In the beginning, I would like to express my appreciation to all the people made this doctoral thesis possible and an unforgettable experience for me.

I would like thank Prof. Dr. Lorenz Singheiser for giving me the chance to work in the Institute of Energy and Climate Research, Microstructure and Properties of Materials (IEK-2), Forschungszentrum Jülich GmbH. I would like to express my gratitude to Dr. Jürgen Malzbender for the inspiring discussions, careful corrections, constant encouragements and continuous contribution to the activities within the project during the entire PhD period.

I would like to thank all the institute colleagues for introductions and consistent support of the experimental equipment: Dr. Egbert Wessel and Dr. Daniel Grüner for the comprehensive SEM studies, Mr. Mirko Ziegner for the high-quality XRD measurement campaigns, Mr. Volker Gutzeit and Mr. Jörg Bartsch for the important support in metallographic investigations, Ms. Tatjana Osipova and Mr. Ralf Küppers for the continuous vital support in thermo-mechanical testing.

A significant scientific and project support was provided by the colleagues from IEK-1: Dr. Falk Schulze-Küppers, Dr. Madhumidha Ramasamy, Dr. Stefan Baumann, Dr. Uwe Sebold, Prof. Dr. Wilhelm Albert Meulenberg. Also project partners from Universidad Politécnica de Valencia, Institute of Chemical Technology (ITQ), Valencia, Spain: Dr. Cyril Gaudillere, Dr. María Balaguer, Prof. Dr. José M. Serra. From Saitama University, Japan: Prof. Dr. Wakako Araki.

I would also like to say many thanks to my group colleagues who played an important role in the scientific everyday life: Anna Böhm, Vahid Ebrahimzade, Masood Fakouri Hasanabadi, Sebastian von Helden, Juliane Nonemacher, Rafael Oliveira Silva, Goran Pećanac, Vanessa Stournari, Viacheslav Vasechko, Jianping Wei, Gang Yan and Xiaoyan Yin.

Finally, I would like to explain my profound gratitude to my family and my friends, especially Yuan Feng, for their constant caring, support and encouragement.

Contents

List of Figures

List of Tables

Introduction

Global warming and climate change, which have already caused an observable sea level rising, glacier retreat and arctic shrinkage, are increasing challenging issues for human subsistence [1]. One of the major causes for global warming is attributed to the emission of greenhouse gases. The main greenhouse gases in the Earth's atmosphere are water vapor, carbon dioxide, methane, nitrous oxide, and ozone [2,3]. Energy production and industrial sectors including cement production are both considered as major sources of human made CO_2 emissions. To reduce the atmospheric and marine accumulation of greenhouse gases, which are released by burning fossil fuels, an artificial carbon sequestration process has been proposed as a way to mitigate or defer global warming [4]. Oxyfuel combustion is one of the most appropriate concepts to produce a CO_2 rich flue gas ready for sequestration and at the same time also increase combustion efficiency.

Furthermore, Oxygen is one of the most important commercial gases for industrial applications. Global oxygen production is reported to be approximately 100 million tons per year [5]. Considering the development of clean and sustainable energy technologies, for instance, pre-combustion solid fuel gasification and oxyfuel approaches [6,7], which require the use of pure oxygen, the demand for pure oxygen is expected to increase even more in the future. Nowadays, most of the oxygen that is separated from air for industrial applications is produced by using cryogenic distillation and pressure swing adsorption [5]. In the last 30 years, an appealing alternative for oxygen production has emerged, which is based on the development of the ceramic based oxygen transport membrane (OTM) materials [5–9]. OTM is supposed to be able to generate high purity oxygen at low energy consumption, particularly if good thermal integration in high-temperature industrial process is realized. With respect to application relevant membrane designs, an asymmetric membrane consisting of a thin dense membrane layer supported by a porous substrate was suggested to ensure high permeation rate and relative higher mechanical stability [10–15].

For application as membranes in power plant, the materials should exhibit high oxygen conductivity, chemical and structural stability in long-term operation, compatibility of thermal expansion with metallic structures, and a high resistance to mechanical failure (e.g. fracture stress). The present work focuses on the mechanical properties of membrane layers and potential substrate materials based on in-house experience and literature. Mechanical data, in particular temperature dependencies of strength, elastic modulus and creep as well as creep rupture tests were carried out to supply basic materials characteristics needed for modeling of room and elevated temperature lifetime under application relevant stress levels. The effect of membrane layers on the mechanical stability of substrate materials as well as the effect of the substrate constraints on the mechanical stability limits of the membrane coating are assessed. Materials tested with respect to permeation and chemical stability at the partners facilities were characterized with respect to effects of operation relevant conditions on the mechanical stability.

Chapter 1.

Literature Review

Mixed ion-electron conductivity (MIEC) materials with high oxygen permeation are currently exploited as promising oxygen transport membranes (OTMs) for gas separation. Perovskites like $Ba_{0.5}Sr_{0.5}Co_{0.8}Fe_{0.2}O_{3-\delta}$ (BSCF) and $La_{0.6}Sr_{0.4}Co_{0.2}Fe_{0.8}O_{3-\delta}$ (LSCF) have been proposed for OTM application, since they exhibit strong oxygen permeation at elevated temperatures. In this chapter, the functional and designing principles of the OTM are reviewed. Mechanical properties important for long-term reliability of OTM materials under application conditions are introduced. Considering the asymmetric membrane design, with a dense membrane layer on porous support, the specialties of porous ceramics are emphasized. At the end, information on the materials investigated in the present work is reviewed and summarized in details.

1.1. Oxygen transport membrane (OTM)

An oxygen transport membrane can be described as a barrier between two enclosures, which preferentially allows oxygen ions to permeate under the action of an electrical potential gradient or a chemical potential gradient (i.e. oxygen partial pressure) as driving force [8]. Since oxygen is transported in an ionic form through the membrane material, there must be a simultaneous electron flux in the opposite direction to compensate the oxygen ion flux and to maintain electric neutrality [8,9]. Therefore, a suitable membrane material is not only an ionic but also an electronic conductor, hence also called Mixed Ionic–Electronic Conducting (MIEC) membrane (Figure 1.1).

Essentially, OTMs consist of a thin, dense ceramic membrane where oxygen ions diffuse across the membrane, usually via interstitials or vacancies triggered by the stoichiometry of the material. Among the MIEC materials, most of the high oxygen permeation materials belong to the fluorite or perovskite type ceramic. These structures have a high tolerance of non-stoichiometry that permits them to obtain a high number of oxygen vacancies and/or interstitial sites and consequently enhance the oxygen ionic conduction [16].

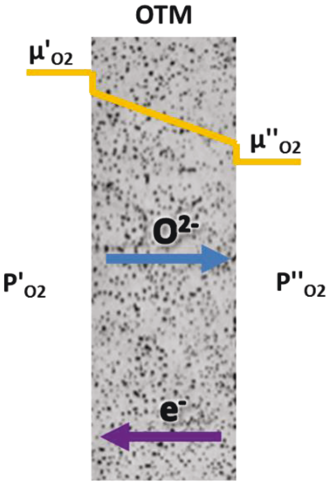

Figure 1.1 Single phase mixed ionic-electronic conducting (MIEC) membrane.

1.1.1. Transport mechanism

The transport of oxygen through a dense mixed ionic–electronic conducting material involves three successive steps (Figure *1.2*) [17,18]:

(i) the surface-exchange reaction on the feed side, i.e. dissociation of oxygen molecules into oxygen anions at the high partial pressure side. This process can be described by:

$$\frac{1}{2}O_2\,(g) + 2e^- + V_O^{**} \rightarrow O_O^x \tag{1.1}$$

(ii) the simultaneous lattice diffusion of oxygen ions and electron/electron holes in the bulk phase.

(iii) the surface-exchange reaction on the sweep side; recombination of oxygen anions into oxygen molecules on the low partial pressure side of the membrane. This step can be described by:

$$O_O^x \rightarrow \frac{1}{2} O_2\,(g) + 2e^- + V_O^{**} \tag{1.2}$$

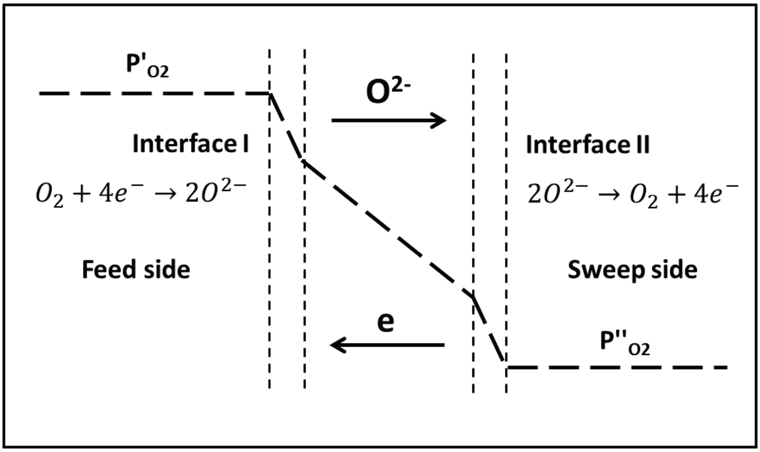

Figure 1.2 Different steps involved in oxygen transport during oxygen permeation.

The oxygen permeation rate is determined by the slowest process. Each mechanism has the potential to become the rate-controlling step and the slowest process will limit the overall permeation flux. For relatively thick membranes (thickness > 100 μm), solid state diffusion commonly controls the process and oxygen flux can be described by the Wagner equation [19]:

$$J_{O_2} = \frac{RT}{16F^2L} \int_{P''_{O_2}}^{P'_{O_2}} \frac{\sigma_{el} \cdot \sigma_{ion}}{\sigma_{el} + \sigma_{ion}}\, d(\ln P_{O_2}) \tag{1.3}$$

where J_{O_2} is the oxygen permeation flux, R is the gas constant, F is the Faraday constant, L is the membrane thickness, P'_{O_2} and P''_{O_2} are the oxygen partial pressures at the high-pressure side and low pressure side, respectively, σ_{el} is the electronic conductivity, and σ_{ion} is the ionic conductivity.

1.1.2. Asymmetric membrane

The overall oxygen permeation of an oxygen transport membrane depends on several factors such as material composition [20], powder preparation method [21], sintering temperature [22,23], membrane shape [24] and thickness. As stated by Wagner's equation [19,25], the flux through a dense membrane is proportional to the inverse of the membrane thickness. Reducing membrane thickness results in higher oxygen fluxes [26–30] until other mass transport or surface kinetic phenomena start to limit the permeation process. For practical applications, high permeation fluxes are essential and the optimized membrane thickness should be in the range of several microns (10 – 50 μm) [15]. Therefore, for practical applications, where high oxygen fluxes are necessary, thin membranes are required to increase the flux of oxygen by minimizing the ion diffusion limitation. Recently, with respect to application relevant membrane designs, an asymmetric membrane consisting of a thin dense membrane layer supported by a porous substrate was suggested [10–15], as shown in Figure *1.3*. The aim of asymmetric membranes is not only to boost the gas transport but also to enhance the mechanical stability of the entire thin layer membrane structure, which therefore renders the mechanical properties of the porous substrate critical for the reliability of the whole component [31–33], hence being the focus of various recent studies [31,32,34–36].

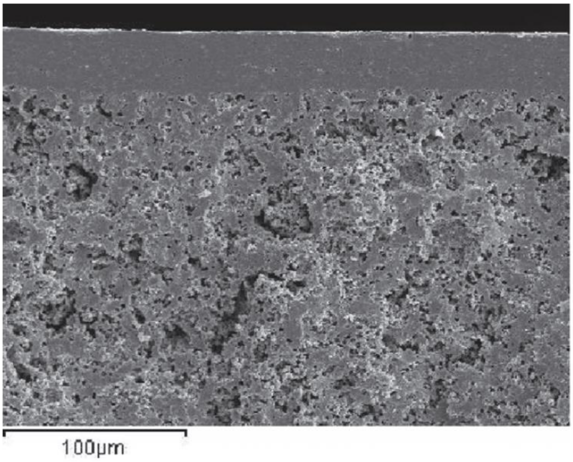

Figure 1.3 Fracture cross-section (SEM image) of an asymmetric membrane assembly consisting of porous support and dense membrane layer from $La_{0.6}Sr_{0.4}Co_{0.2}Fe_{0.8}O_{3-\delta}$ [15].

However, during operation at high temperatures, this approach brings mechanical stability issues due to the high thermal expansion coefficient (CTE) observed in most of OTM ceramic materials [37]. A CTE mismatch between the dense layer and the substrate may generate cracks that could compromise performance. To avoid this problem, the porous substrate may be fabricated from the same material as the dense layer, or the CTEs of the two materials should be matched.

In addition, the introduction of a porous substrate also generates a source of resistance to the oxygen flow. Since gas diffusion through the pores is the main transport mechanism through the support, the architecture of the pore structure should provide a compromise between maximizing gas flow and mechanical properties. All of these resistances (surface exchange, solid state diffusion across the membrane, and gas diffusion through the porous structure) are intrinsic to the process and thus cannot be eliminated. As a result, it is critical to understand the controlling mechanisms and ameliorate them as a function of membrane composition, membrane architecture, and operation conditions.

The support engineering is then crucial and the substrate has to fulfill certain mechanical, microstructural and physio-chemical requirements, which are [38]: (i) to confer a good mechanical integrity on the porous support/dense top layer assembly and to avoid possible damage under harsh conditions, (ii) to minimize the pressure loss through the support in order to allow the membrane to operate at high flow rates and (iii) to provide a high mixed electronic and ionic conductivity and a high density of Triple Phase Boundary (TPB) where ion, electron and gas can meet for the oxygen reduction reaction. Indeed, due to the limited reaction site density at the interface porous support/dense layer, it is necessary that the porous support has a high TPB density, where the gaseous oxygen (in the case of O_2 separation) and the electronic and ionic conductive phases contact.

1.1.3. Membrane materials

Although in the past decades, significant developments have been achieved, there are still several issues in mixed conducting ceramic membranes, such as chemical and mechanical stability problems and the necessary too high operating temperature to obtain application relevant oxygen permeation fluxes [19]. Overall, the criteria for the membrane material selection can be summarized as follows [8,16]:

- considerable high oxygen permeation flux under high temperature operation condition;
- stability for long-term operation under the application relevant temperature, oxygen partial pressure range, and corresponding working atmosphere;
- sufficient mechanical strength;

- compatibility with the other cell components;
- considerably low cost of the materials and fabrication;
- suitable high temperature sealing of the membranes.

From an economic point of view, it has been suggested that a sufficiently high oxygen permeation flux of at least 1 ml (STP)/cm^{2}min (7.44×10^{-2}mol/cm^{2}s) should be reached, although a higher value of 3.5 ml (STP)/cm^{2}min (2.604×10^{-6}mol/cm^{2}s) would be needed to match the requirements of current technological applications [16,39].

Among ceramic membranes with mixed ionic-electronic conducting characteristics, most of the best compounds in terms of oxygen permeation properties are fluorite-type (AO_2) and perovskite-type (ABO_3) [8]. As driving force, sufficiently low or high values of oxygen partial pressure are necessary to obtain required mixed ionic-electronic conduction, where electronic defects are generated for charge compensation of the excess of ionic defects relative to the stoichiometric composition.

The ideal fluorite structure consists of anions in simple cubic packing with half of the interstices occupied by cations, as shown in Figure *1.4*(a), and is termed after the CaF_2 structure. Oxygen-deficient fluorite-related structures such as ZrO_2 and CeO_2 doped with CaO or Y_2O_3 are important solid oxide electrolytes materials [8]. More recently, it has been an interesting research direction to introduce enhanced electronic conduction in fluorite matrices in the form of dual-phase membranes. Notable examples include yttria-stabilized zirconia doped with either titania [40] or ceria [41]. This type of structure tends to have cations occupying all cation sites, while leaving many of the oxygen anion sites empty, leading to a high oxygen deficiency [42,43].

The perovskites oxides of the type ABO_3 (rare earth metal ions at A sites and transition metal ions at B sites), such as LSCF ($La_{0.6}Sr_{0.4}Co_{0.2}Fe_{0.8}O_{3-\delta}$) and BSCF ($Ba_{0.5}Sr_{0.5}Co_{0.8}Fe_{0.2}O_{3-\delta}$) have attracted much attention in the last decades due to its high permeation fluxes and excellent stabilities [12,16,19,44,45]. Perovskite is a structural family of inorganic materials with the structure of $CaTiO_3$ [46]. The ideal perovskite has cubic symmetry with the space group Pm3m, as shown in Figure 1.4(b). The transition metal ions (B) are located in the center of the cube, forming an octahedral with 6 nearest oxygen ions. The angles between the six equal B-O bonds are 90 °. A-ions are located at the corners surrounded by twelve equidistant oxygen ions. The perovskite structure is preserved if the tolerance factor (t) as given in the following equation is between 0.8 and 1 as stated by Goldschmidt [47]:

$$Tolerance\ factor\ (t) = \frac{r_A + r_O}{\sqrt{2}(r_B + r_O)} \tag{1.4}$$

where r_A, r_B and r_O are the ionic radii units of the A site cation, B site cation and oxygen. If the bond length is roughly assumed to be the sum of two ionic radii, the t value of an ideal cubic perovskite should be equal to 1.0. However, Goldschmidt found that, as an experimental fact, most cubic perovskites have t values in the range of 0.8–0.9, and distorted perovskites occur in somewhere wider range of t [48]. In fact, almost all known perovskite compounds have t values in the range of 0.75–1.00 [49]. Hayashi et al. [49] suggested that A site cation should have large ionic radii to obtain large free volume and B site cation should be selected to regulate the tolerance factor to approximately 0.96.

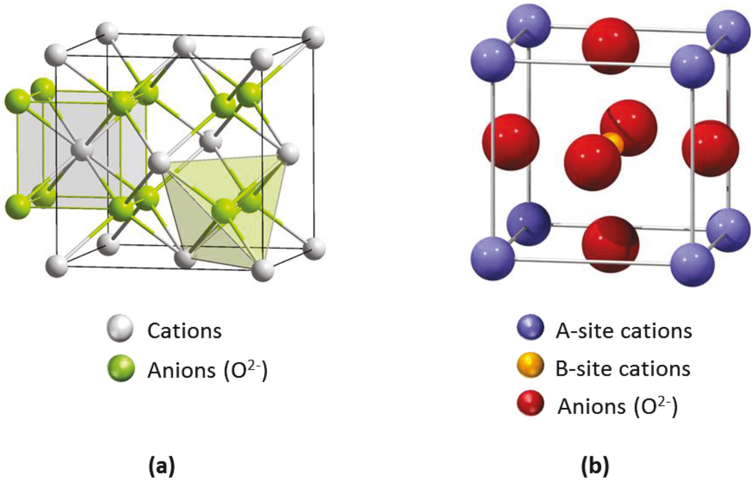

Figure 1.4 The ideal structure of (a) fluorite [50] and (b) perovskite [51].

1.2. Mechanical characteristics

Under application conditions, different stresses will be induced into the membrane materials by different operation condition factors, such as high pressure difference between the two sides of the membranes, thermal and chemical gradients, thermal expansion incompatibilities with other parts of the membrane module, as well as tensile, compressive or bending stresses from stacking and joining into integration modules [8,19,52]. To guarantee the robustness of the membrane modules over long operation periods, risks of mechanical failure need to be estimated and reduced to tolerable levels. Knowledge of deformation and fracture behavior of the membrane materials is necessary for the assessment of the mechanical stability of the membrane components. For long-term application under high temperatures and stress, creep deformation and creep damage can be critical and need to be investigated.

In the following sections, basic principles and theoretical backgrounds of the mechanical investigations performed within the present study are introduced.

1.2.1. Elastic behavior

Experimentally, the respond of solid materials with low strain ε is proportional to the applied stress σ. This phenomenon is described by Hooke's law [53]:

$$\sigma = E\varepsilon \tag{1.5}$$

where E is Young’s or elastic modulus, a quantity used to characterize the resistance of a material to elastic deformation under uniaxial load. ε is the strain of the material defined as:

$$\varepsilon = \frac{L - L_0}{L_0} \tag{1.6}$$

where L is the length under the applied stress, and L_0 is the original length.

When the stress is increased above the reversible elastic strain limit either direct fracture without significant plastic deformation or plastic deformation and then fracture follows [54].

Elastic moduli can be determined with different static or dynamic methods. For brittle materials, uniaxial and biaxial bending tests are widely used. As macroscopically non-destructive method, micro-indentation is also often used. The three-point bending test [55] is a widespread method for analyzing material behavior, where brittle materials associated clamping problems do not permit tensile testing [55]. The alignment is easily achieved and specimens with simple geometric shapes can be used.

The biaxial ring-on-ring bending test is also frequently used. Stress distribution is symmetrical and homogeneous around the center of disc-shaped specimen. Stresses across the disc thickness vary from compressive (at the loading-ring side) to tensile (at the supporting-ring side). But in this test, specimen unevenness and frictional effects can have a huge influence on stress distribution [56].

Although mostly bending tests are possible, the uniaxial compression test is also frequently performed to obtain stress-strain behavior for different temperatures for brittle materials. The deformation rate (or loading rate) can be controlled. With small deformations, the stress distribution is uniaxial. Therefore, elastic parameters, such as Young's modulus, permanent deformation or Poisson's ratio can be easily determined from the stress-strain curves.

Micro-indentation test [57] is an easily operated and fast method for measuring elastic moduli. The advantage of this method is that it is macroscopically non-destructive and the use of a very small surface area during the investigation. The disadvantage is that the results from indentation test are strongly localized, i.e. the material need to be homogeneous. Typically, strength determination is not possible via micro-indentation.

The Impulse Excitation Technique (IET) is a non-destructive dynamic mechanical test for the investigation of Young's moduli. It is based on the natural frequency of the tested materials. This technique allows the determination of a quasi-continuous elastic modulus - temperature dependency under various atmospheres [58].

From an atomic view, the elastic modulus is directly related to bonding forces between atoms [53,54]. Hence, as the temperature increases, the elastic modulus generally decreases. An empirical relationship that fits the data for several ceramics is [54]:

$$E = E_0 - bT\ exp(\frac{-T_0}{T}) \tag{1.7}$$

where E_0 is elastic modulus at absolute zero; b and T_0 are empirical constants; and T_0 is about half the Debye temperature. As the temperature increases, the vibration frequency of the atoms (and hence the interatomic spacing) is enhanced and the bonding force is slightly decreased.

However, for polycrystalline ceramics there is an additional effect due to grain boundaries [54]. At high temperatures, due to the contribution of grain boundary sliding and grain boundary softening, a rapid decrease can occur in values of elastic moduli [54]. Besides, in real ceramic, microstructural effects, such as porosity and second phases, have also an influence on the mechanical constants. In particular, a detailed review of the influence of porosity on mechanical properties is given in Section 1.3.2.

1.2.2. Strength and fracture

Most ceramics are brittle at room temperature, which means, they fracture with very little plastic deformation. From atomic level, brittle fracture happens via separating two planes of atoms. But the calculated "theoretical" strength from this atomic principle is much larger than experiments data [53,54]. In the work of A. A. Griffith [59], it is suggested that the presence of preexisting cracks in the surface or inside the ceramic and/or the sharp corners, that might be introduced during processing, act as stress concentrators. The basic idea is an energy balance: the energy consumed in forming new surface as a crack propagates against the elastic energy released. The critical condition for fracture, then, occurs when the rate at which energy is released is greater than the rate at which it is consumed [53,54]. In another words, the stress intensity exceeds the critical stress intensity factor (or more commonly termed the fracture toughness) and then unstable crack growth occurs [53,54]. For a "Griffith" crack of length 2*c*, the fracture stress is given by the Griffith equation [54]:

$$\sigma_f = \sqrt{2E\gamma/\pi c} \tag{1.8}$$

where σ_f is the fracture stress, E the elastic modulus and γ the surface energy.

Hence, the Griffith equation shows that fracture stress depends on the [54]:

- elastic modulus (a property of the material);
- surface energy (a property of the material);
- crack length.

1.2.3. Weibull analysis

Since the fracture stress of a ceramic specimen depends on the crack length, it is usually analyzed on the basis of the so-called "weakest link" approach. The "weakest link" theory is to consider a chain the strength of which is determined by the weakest link [60,61].

Ceramics usually exhibit large scatter in measured fracture stresses. Hence, a probabilistic approach needs to be applied to present this scatter in a quantitative way so that these materials can be used safely. The most popular method is to use Weibull statistics, which are based on the weakest link approach.

According to the two-parameter Weibull statistics, the cumulative failure probability $P(\sigma)$ of a brittle material subjected to a stress σ is given by (see ASTM C1239-13) [62]:

$$P(\sigma) = 1 - exp\left[-\left(\frac{\sigma}{\sigma_0}\right)^m\right] \tag{1.9}$$

where σ_0 is a normalization factor known as the characteristic fracture strength or scale parameter, which corresponds to a failure probability of 63.21% and is hence a weak criterion for assessing the reliability of brittle materials; m is the Weibull modulus or shape parameter of the distribution, indicating how rapidly the fracture stress falls when approaching σ_0, and hence also being a measure of the fracture stress diversity.

Ceramic materials typically show a volume or surface area dependency of the strength. The reason is again related to the preexisting cracks. These cracks can be randomly distributed throughout the volume of the sample or in the surface or edges of the specimen due to machining effects. With a larger body, the probability of finding a larger crack increases. Consequently, the sample becomes weaker. In addition, the geometry and the loading condition of the sample will influence the stress distribution during loading. The term effective volume (V_{eff}) (effective area for surface defects that can be used equivalently) is used to indicate how “effectively” the body is being stressed. For uniaxial tension, V_{eff} is equal to the actual volume of the sample. The effect of effective volume can be expressed mathematically via the following Equation (1.10), where fracture stress values are connected to a certain failure possibility and also a specific effectively deformed area or volume [54,61]:

$$P(\sigma) = 1 - exp\left[-\left(\frac{V_{eff}}{V_0}\right)\left(\frac{\sigma}{\sigma_0}\right)^m\right] \tag{1.10}$$

In one sample, different kinds of defects might exist; for example, pores and inclusions introduced during sintering and surface flaws introduced during grinding. The different defect types may lead to different Weibull distributions and different Weibull moduli that superimpose and require careful deconvolution of the data, i.e. for a body with two different types of volume defects, the respective dual Weibull distribution is represented by the equation [54]:

$$P(\sigma) = 1 - exp\left[-\left(\frac{V_{eff,1}}{V_0}\right)\left(\frac{\sigma}{\sigma_1}\right)^{m_1} - \left(\frac{V_{eff,2}}{V_0}\right)\left(\frac{\sigma}{\sigma_2}\right)^{m_2}\right] \tag{1.11}$$

where for defect type 1, corresponds to effective volume $V_{\text{eff},1}$, characteristic fracture strength σ_1, and Weibull modulus m_1; for defect type 2, corresponds to $V_{\text{eff},2}$, σ_2, and m_2.

Furthermore, proof testing has become one of the standard practices in many engineering applications [63–65] in terms of warranting production orientated mechanical reliability. The typical reason for employing proof-testing is as follows: within a population, there may be specimens which are sufficiently weak, so that the function of the material and hence entire component is severely impaired. Proof-testing the population and hence the entire batch of components will necessarily remove these weak specimens. Furthermore, there is a guaranteed minimum strength and related time to failure for the remaining components, which ensures the successful operation of the material beyond that value [66]. In proof testing, ceramic components are loaded to stresses that exceed those expected in service in order to break the week components and thus truncate the lower end of the fracture stress distribution. In this manner, weak components are eliminated before they can be placed in service. When the material is loaded thereafter in service, the failure process is assumed to result from flaws which require stresses or times to failure in excess of the proof-load conditions [67,68]. Some of the important applications for proof testing include the various uses of aerospace industry [63], electrical porcelain insulators [64], and optical fibers [65].

1.2.4. Creep behavior

Creep occurs when a solid material is subjected to a stress at high temperatures for long time. It is a slow and continuous plastic deformation, for ceramic materials, typically when the temperature $T > 0.5T_m$, where T_m is the melting point in Kelvin [53]. Sooner or later, creep will lead to failure or structural instabilities already under low stress exposure, which will render the end of the lifetime of the ceramic components. In general, creep behavior is affected by extrinsic and intrinsic parameters, such as stress, temperature and grain size. The typical strain behavior associated with creep under constant stress over time is illustrated in Figure 1.5(a). Increasing the temperature and/or stress (Figure 1.5b) results in an increase in both the instantaneous strain and the steady-state creep rates and a decrease in the time to failure [53].

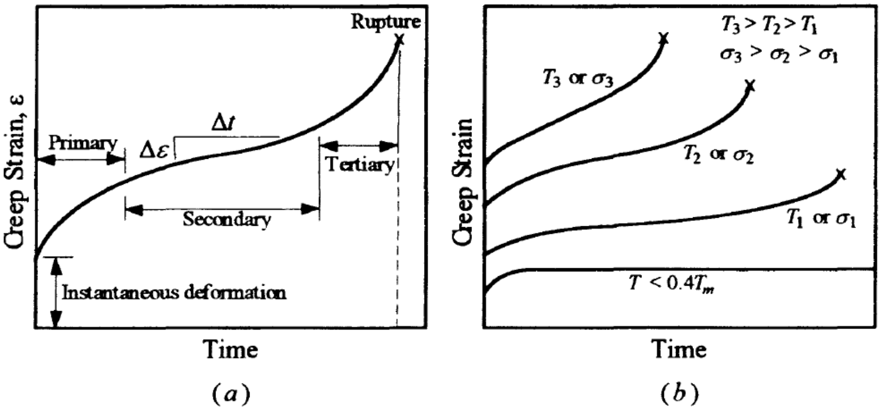

Figure 1.5 (a) Typical strain versus time creep curves with three distinct regimes. (b) Effect of increasing stress and or temperature on the creep response of the material [53].

In general, the creep response of a solid is determined by measuring the strain rate as a function of applied stress. This is done, simply by applying a load to the sample at elevated temperatures, and measuring its deformation as function of time. There are three distinct regimes in a general creep curve [53,54]:

Regime I: Primary or transient creep. At this stage, the creep rate decreases with time from an initially high value. This stage of creep is often represented by an equation of the form [53,54]:

$$\varepsilon = \beta T^{m} \tag{1.12}$$

where β is a constant, and m varies from 0.03 to 1.0 depending on the material, stress, and temperature.

Regime II: Secondary or steady-state creep. In this regime, the strain rate is constant and the deformation may continue for a long time. This is the most important regime. The equation for secondary creep is [53,54]:

$$\varepsilon = Kt \tag{1.13}$$

where K is a constant that depends on stress and temperature.

Regime III: Tertiary creep. The strain rate accelerates rapidly just prior to specimen failure. Formation of cracks or nucleation and growth of cavities is observed in microstructure. In ceramics, the tertiary creep stage is often very short or entirely missing [61].

Furthermore, in ceramics, many mechanisms, some of which are not sufficiently well understood, have been proposed [53,61]. The problem is further complicated by the fact that different mechanisms may be operative over different temperature and stress regimes. From a practical point of view, secondary creep is the most important stage and is the major concern for lifetime prediction. The mechanisms for this stage are discussed in the next sections.

In general, creep rate of the secondary creep regime is a convoluted function of stress, temperature, grain size and shape, microstructure, volume fraction and viscosity of glassy phases at the grain boundaries, dislocation mobility, etc. [53]. This complex dependence can often be represented mathematically in a general form as [69]:

$$\dot{\varepsilon} = A\left(\frac{1}{d}\right)^{m} {P_{O_2}}^{p}\sigma^{n} exp\left(-\frac{E_a}{RT}\right) \tag{1.14}$$

where A represents an empirical constant, d grain size, m grain size exponent, P_{O_2} oxygen partial pressure, p oxygen pressure exponent, σ applied stress, σ stress exponent, E_a apparent activation energy, R gas constant and T the absolute temperature.

There are mainly three categories of creep mechanism for ceramic materials: diffusion (Nabarro-Herring and Coble), viscous, or dislocation creep.

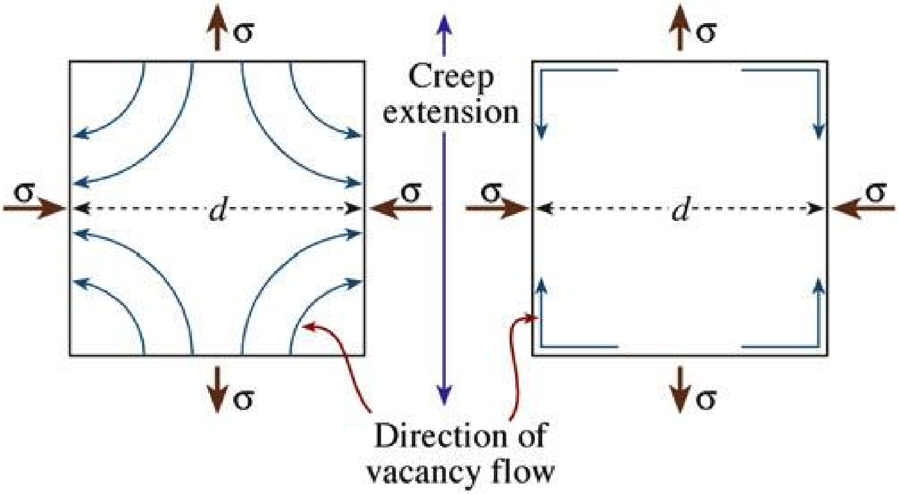

Figure 1.6 Nabarro-Herring creep [54].

Diffusion-controlled creep is due to atomic diffusion. Considering a single crystal as shown in Figure 1.6, vacancies would move from the faces under tension to those under compression and the atoms move in the contrary direction, resulting in a permanent shape change. This is the so-called Nabarro-Herring creep [70]; the diffusion path is through bulk material. It usually occurs at higher temperatures where bulk diffusion is faster than grain boundary diffusion [54]. However, at lower temperatures, or in the case of solids with very fine grains, grain boundary diffusion may be the faster path, which is known as Coble creep [71]. For both creep mechanisms, it is assumed that the grain boundaries are perfect sources or sinks for vacancies.

Viscous creep (also called "grain boundary sliding") is controlled by the viscous flow of intergranular glassy phases formed during fabrication which are present in many structural ceramics. If these phases softens at high temperature, then we get creep by grain boundary sliding. The creep rate is controlled by the viscosity of the glassy phase, which is a function of temperature [53,54].

Dislocation creep occurs by dislocation motion (i.e., glide and climb). This type of creep is typical for metals [53] and usually not relevant for ceramics.

All the creep mechanisms can be described by the general Arrhenius equation form, but the various creep mechanisms give different *m, p and n* values and some of these are summarized in Table 1.1. From the analysis of creep data, values of *m* and *n* might be obtained and thus, in principle, one can identify the predominant mechanism.

Table 1.1 Creep equation exponents and diffusion paths for various creep mechanisms [54,61].

Creep mechanism	***m***	***n***	***Diffusion path***
Dislocation creep mechanism			
Dislocation glide climb, climb controlled	0	4-5	Lattice
Dislocation glide climb, glide controlled	0	3	Lattice
Dissolution of dislocation loops	0	4	Lattice
Dislocation climb without glide	0	3	Lattice
Dislocation climb by pipe diffusion	0	5	Dislocation core
Diffusional creep mechanisms			
Vacancy flow through grains	2	1	Lattice
Vacancy flow along grain boundaries	3	1	Grain boundary
Interface reaction control	1	2	Lattice/grain boundary
Grain boundary sliding mechanisms			
Sliding with liquid	3	1	Liquid
Sliding without liquid (diffusion control)	2-3	1	Lattice/grain boundary

For a given ceramic, a specific creep mechanism may dominate at certain temperatures and stresses. This can be represented on a creep deformation map, as illustrated in Figure *1.7*. Such a map should be based on a large amount of experimental data. The creep behavior of a material can be analyzed in terms of experimental results with multi-linear fitting routines in order to obtain the creep parameters as illustrated in Figure 1.8.

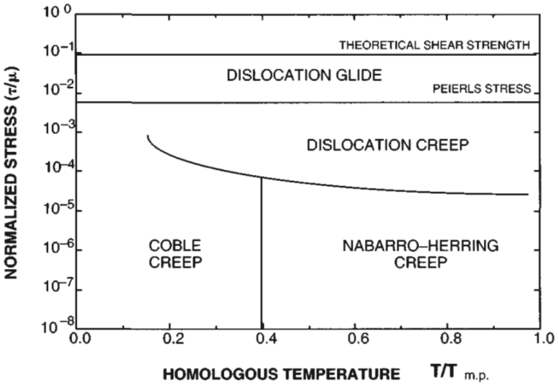

Figure 1.7 Schematic of a creep deformation map for a polycrystalline material (after Frost and Ashby, 1982)[61].

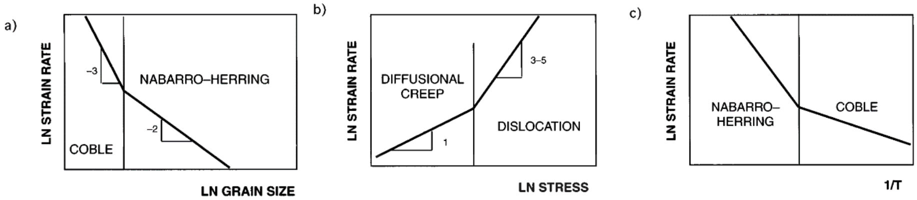

Figure 1.8 Various experimental approaches to determine mechanisms involved in secondary creep.

1.3. Porous ceramics

1.3.1. General description of a porous solid

Most materials, both naturally and artificially, are to some extent porous, their physical properties such as density, thermal conductivity and strength are all dependent on the different porous structures. A scheme of the dependency of different physical properties on porosity is shown in Figure 1.9. In certain applications such as filters, insulators or catalytic supports, pores enable functionality and are introduced deliberately. The introduction of porosity is therefore an extremely useful and powerful tool for greatly extending the range of properties offered by a ceramic component [72]. In an asymmetric membrane OTM design, the porous support supposes not only to boost the gas transport but also to enhance the mechanical stability of the entire structure of the thin membrane layer, which therefore renders the mechanical properties of the porous substrate critical for the reliability of the whole component [31–33].

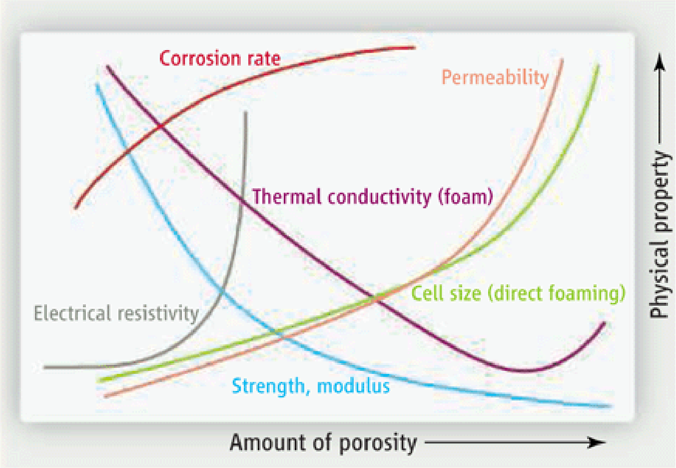

Figure 1.9 Dependency of physical properties on the amount of porosity [72].

Porosity of a solid is an overall characteristic, which is defined as the fraction of pore volume V_{pore} to the total volume V_{total} [73]. If the volume of solid material is denoted by V_{solid}, and the pore volume as $V_{pore} = V_{total} - V_{solid}$, the porosity can be defined as:

$$P = \frac{V_{total} - V_{solid}}{V_{total}} = \frac{V_{pore}}{V_{total}} \tag{1.15}$$

The porosity can be expressed either as a fraction or as a percentage. Different classifications of pores are quoted by different standards [74], for example the accessibility of the pores to an external fluid, the shape of the pores, or the pore size. Figure *1.10* shows typical kinds of pore types in a porous solid. With respect to the accessibility to an external fluid, the pores, which are absolutely isolated from other pores, as in region (a), are described as closed pores. On the other hand, the continual porous network connected to the external surface of the analyzed body, like (b) (c) (d) (e) and (f), is referred to as open pores. The pore volume used in Equation (1.15) can be either the volume of the open pores, which leads to the open porosity, or that of the strictly closed pores, which leads to the closed porosity, or that of both types of pores together, then leading to the total porosity.

According to their different shapes, pores can be cylindrical (like (c) and (f)), ink-bottle shaped (b), funnel shaped (d) or slit-shaped. Besides, the roughness of the external surface, like the area around (g), should be distinguished from porosity. A simple way to distinct it is that the pore depth is larger than its width.

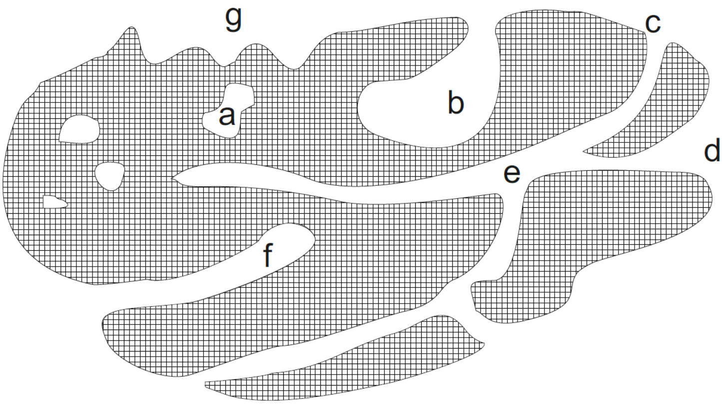

Figure 1.10 Schematic cross-section of a porous solid [74].

Pore size generally refers to pore width, which is the distance between two opposite walls of the pore, for example, the width of a slit-shaped pore and the diameter of a cylindrical pore. The pore classification according to pore size is recommended by IUPAC, which is defined as following [74]:

- Macropores: with width larger than 50 nm.
- Mesopores: with widths between 2 and 50 nm.
- Micropores: with widths smaller than 2 nm.

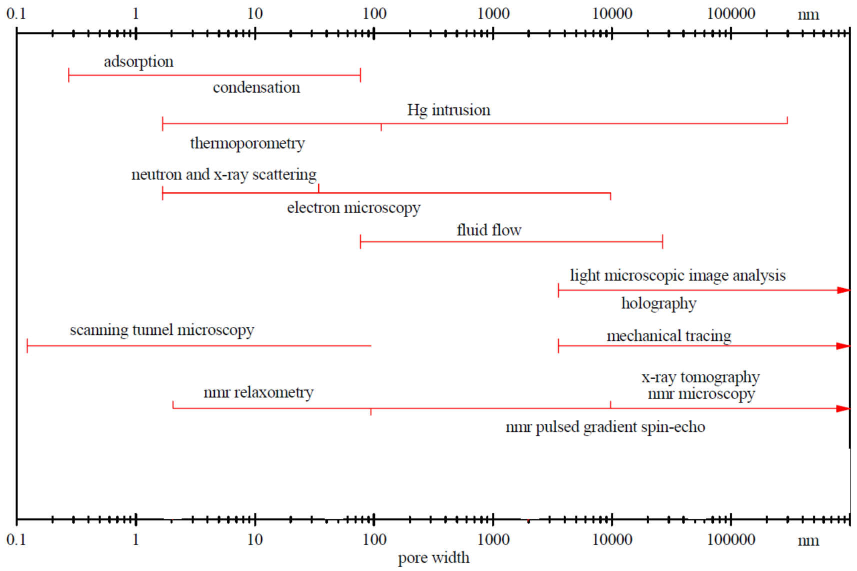

Figure 1.11 Measurement ranges of important characterizing methods of pores [73].

The complexity and variety of porous material has led to the application of many experimental techniques for their characterization. Large effort has been expended in the development and refinement of different porosity measurement methods. The principal techniques utilized for measuring porosity include image analysis method, fluid saturation method, mercury intrusion porosimetry, helium pycnometry and radiation scattering method [73]. Different methods rely on completely different physical principles, which leads to different advantages and limitations in application. Figure *1.11* gives an overview of commonly used methods and their range of validity with respect to different pore sizes.

Therefore, the results obtained by different methods cannot be directly compared to each other. Some methods have only access to open pores (i.e. methods using a fluid), while some others may have access to closed pores (i.e. methods using a radiation).

Even when a method is used, the obtained porosity value also depends on the experimental conditions, for instance, the size of the molecular probe (fluid displacement, adsorption) or the magnification (image analysis). Hence, for a record value of porosity, it represents not only a physical property of the material, but also the method used for the determination. Furthermore, comparisons and correlations between different methods helps to characterize the porous structure [75].

1.3.2. Porous structure and mechanical properties

Materials with a porous structure are common in nature. The most important parameter to describe a porous structure is its overall porosity. Moreover, there is the matter of the character of the porosity, namely, morphology. Some natural porous materials, such as wood and cork, have prismatic and unidirectional honeycomb-like cells, while others, such as trabecular bone and sponges have randomly oriented polyhedral cells [76,77]. In these cases, their properties are strongly linked to their microstructure (optimized during thousands of years) and the material.

Some properties of a material, such as lattice parameter and thermal expansion coefficient, have no dependency on porosity. These properties depend only on atomic scale phenomena and are not affected by the long range interference of the pores [78]. Some properties dependent only on the overall porosity, but not the character of porosity, such as density and heat capacity. Such properties can be characterized using a rule of mixtures for the pore volume (P) and the solid phase ($1-P$) [78]:

$$X = X_s(1-P) + X_pP \tag{1.16}$$

where X is the property of the porous material, X_s the same property of the referred to the solid, and X_p the property of the pore phase (usually zero, but there are some exceptions like the refractive index or the dielectric constant). At last, but not the least, the largest, most complex and important group of properties dependent on both the overall porosity and the character of porosity. Properties like mechanical properties, electrical and thermal conductivity and permeability, etc. require a more exhaustive description of the structure to fully characterize the material [79]. In these cases, different structural parameters need to be considered to describe the porous structure. Some of the most important structural parameters are [80]:

- Cell size and its distribution
- Strut thickness and its distribution
- Strut shape and morphology (i.e. dense or hollow struts)
- Cell window opening
- Degree of anisotropy (of porosity, pore size, etc.)
- Surface to volume ratio

Mechanical properties of porous ceramics are very important, not only with respect to a structural function, but also for other cases where the primary function is non-mechanical. Also in such non-mechanical applications, stresses can be induced into the materials and must be survived for the component to continue serving its desired non-mechanical functions.

Mechanical property - porosity dependencies have been characterized mainly experimentally in the last decades. First attempts to link the mechanical properties with porosity were done by Duckworth via fittings of different materials strengths from the work of Ryshkewitch on porosity [81]:

$$\sigma = \sigma_0 exp(-bP) \tag{1.17}$$

where σ is the effective material strength, σ_0 the strength of the solid material without porosity, P the porosity, b can be derived as the slope of $\ln \sigma$ vs. P. This relationship is not valid for porosity higher than 0.5. The values of the exponent b was specified by Knudsen [82]: b = 6 for cubic packing of grains, b = 9 for rhombohedral. The same equation was applied to elastic modulus by Spriggs [83] to fit the available data for materials with low to moderate porosity (P = 0.11 ~ 37.0 %) and a good agreement was obtained between experimental results and exponential fit. Rice modified and extended the application of the equation to higher porosities [84]:

$$E = E_0(1 - exp(-b(1 - P))) \tag{1.18}$$

A further extension with second-order term was proposed by Wang [85] to improve the accuracy of the calculated effective elastic modulus in the porosity range from 0 to 0.38, yielding:

$$E = E_0 exp(-(bP + cP^2)) \tag{1.19}$$

Rice summarized and discussed the **Minimum Solid Area** (MSA) concept based on a range of idealized pore structures by selecting and combining a series of existing models [79]. The minimum solid area model assumes that the idealized porous structure can be obtained by stackings of uniform solid spheres or pores (Figure 1.12a) in certain patterns. In case one, when the stacking element is solid particles, for a body to be a solid, it must have sphere-to-sphere contact. The limit is point contact between particles. The porosity of these models is ~< 50 %. In case two, when the stacking element is pores, the pores can vary from much smaller to much larger dimensions than the pores in case one. The minimum solid areas for stacked particles are the bond areas between them (Figure 1.12b); for stacked pores are the minimal web structure cross-section area between pores (Figure 1.12c). Rice states that the minimum areas of the solid cross-sections between pores will dominate the transmission of stress (i.e. strain, fracture toughness or strength) and the conductive flux (electrical conductivity, thermal conductivity, permeability, etc.) normal to the plane of the slab [79]. Therefore, the change of MSA will directly lead to the change of the related properties of interest.

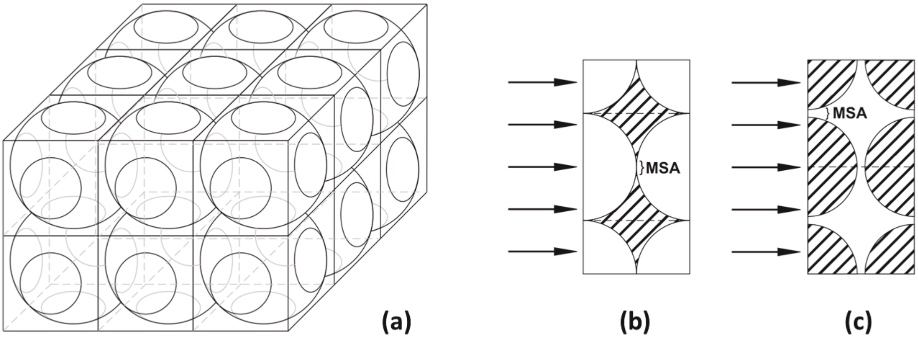

Figure 1.12 Example of idealized pore architecture with Minimum Solid Area modeling. (a) Idealized stacking of uniform solid spheres or pores in cubic array. (b) and (c) cross-sections of solid spheres or pores, respectively. Shadowed parts are regions of pores. Horizontal dashed lines indicate repeat cell structure and minimum sold areas (MSA) are designated [79].

From a certain model, a complete evaluation of the MSA values and the corresponding range of porosity can be done by incrementally changing the size of the pore or spherical particle. The plot of the MSA values (and hence the property of interest) over the corresponding porosity can be obtained as shown in Figure 1.13. At the initial part of the plots, it is a nearly linear decrease of the minimum solid area (and hence the property value of interest) on a semi-log plot versus porosity. And after a critical porosity value, the property of interest starts to decrease very rapidly to zero. The first part of the curves with the semi-log plots also explained the exponential forms of the above empirical equations (Equation (1.17)).

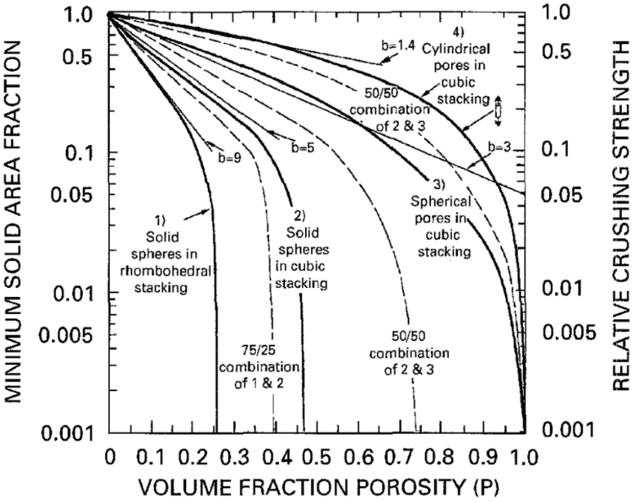

Figure 1.13 The relationship of ratios of calculated minimum bond area per cell to the cell cross-section and corresponding porosity for different solid sphere stacking configurations [79].

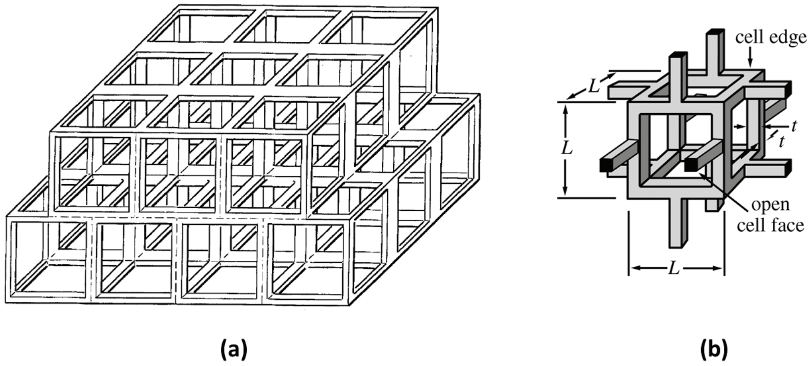

Figure 1.14 Idealized stackings in an open cell foam. (a) Stacking of open cells in orthorhombic array [79]. (b) The 3-dimensional structure of an open unit cell [86].

Another type of model based on the minimum solid area concept is the idealization of the microstructure of a porous material to a representative unit cell composed by an arrangement of struts, as shown in Figure *1.14*. In this model, Gibson and Ashby [77,86–89] assumed the mechanical properties (strength, elasticity, fracture toughness, creep rate, etc.) are determined by the properties of the material and dimensions of the struts. Parameters for calculation include the shape of the polyhedral unit cells (rectangular prism, hexagonal prism, etc.), the stacking arrays of the unit cells (cubic, orthorhombic, etc.) and modes of fracture (brittle crushing, plastic yielding, and elastic buckling). With different fracture modes, this approach can be applied to materials of different nature i.e. polymers, metals, and ceramics [77,86,88,89].

Analytical models have also been proposed to describe the porosity effect on steady-state creep derived on the basis of the creep rates of dense material and idealizations of the porous microstructure. For example, the stacking struts model of Gibson and Ashby [77,86–89] assumes that the deformation is solely controlled by the bending of the cell struts. Similarly the stacking struts model of Hodge and Dunand [90] assumes that the deformation is controlled by the strut compression parallel to the applied stress. Another approach is based on the nonlinear homogenization theory of Castañeda [91]. Here, a porous material is considered as a composite with a solid phase and an "empty" phase. Both approaches described briefly above predict that the stress exponent of the porous body should be identical to that of the dense materials [92,93].

1.4. $La_{0.6}Sr_{0.4}Co_{0.2}Fe_{0.8}O_{3-\delta}$ (LSCF)

The perovskite $La_{0.6}Sr_{0.4}Co_{0.2}Fe_{0.8}O_{3-\delta}$ (LSCF) has been mostly developed for the use as a cathode material in solid oxide fuel cells (SOFCs) and proposed for OTM application, since it exhibits a high oxygen permeation at elevated temperatures and in addition, possesses an excellent stability under application temperature and atmospheres [19,94–97]. Under application relevant conditions, an OTM is operated at high temperatures (~

850 °C) and is exposed to high pressure differences across both sides of the membrane. Under these conditions, the OTM must maintain its structural and geometrical stability over an operation time of several years. Concentrating on dense and selected tape-cast materials, mechanical properties have been studied systematically to estimate long term reliability under application relevant loads [98–102].

The $La_{1-x}Sr_xCo_{1-y}Fe_yO_{3-\delta}$ perovskites have a rhombohedral symmetry at low temperature, and transform at higher temperature to a cubic symmetry by a second order phase transition. The transition temperature depends on the amount of doping [103,104]. The transition temperature of LSCF is ~750 °C in air. Along with this transition, a significant increase of the mechanical characteristics was reported [45,98,100,103], for example the apparent Young's modulus increases by ~50% [100,103].

A non-linear deformation behavior as well as a hysteresis in stress–strain curves has been observed especially at low temperatures due to the ferro-elasticity behavior of the rhombohedral phase [98,105]. A typical non-linear stress–strain curve is schematically illustrated in Figure 1.15, which can experimentally be observed using an axial mechanical load [98]. At the beginning of the loading, the displacement increases almost linearly with stress. Above a critical stress σ_c, the strain should show a progressive increase with applied stress, a region in which some ferro-elastic domains are switched by the applied stress. After most possible (or achievable) domains are switched, the displacement will increase linearly with the stress whilst some possible remaining domains switch. At the beginning of unloading, the displacement decreases linearly with the stress due to elastic recovery deformation and then non-linearly due to domain back-switching. After removing the stress, a non-recoverable remnant strain might be observed. The stress–strain curve of the sequential cycle generally should show a hysteresis; however, there will be no hysteresis if the applied maximum stress is high enough to switch all domains completely [98].

Since there are two equivalent directions of the rhombohedral structure, a spontaneous reorientation of domains can occur under mechanical stress [106]. Ferro-elastic domain switching may increase the fracture toughness of materials [107], and cause stress relaxation in zones of higher stress. Hence, ferro-elasticity is an important non-linear deformation mechanism that needs attention to understand the mechanical behavior of LSCF perovskite. In fact, LSCF ferro-elastic domain switching has even been observed in-situ under compressive load application [101].

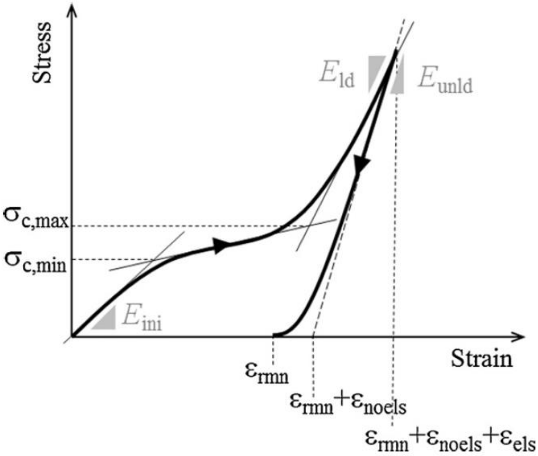

Figure 1.15 Typical stress–strain curve of ferro-elastic material. The symbols σ_c, E, and ε represent critical stress, apparent Young's modulus, and strain, respectively [98].

Due to the nonlinear behavior associated with the existence of the LSCF rhombohedral phase, elastic parameters, such as Young's, shear and bulk moduli and Poisson's ratio, cannot be simply evaluated from stress–strain curves of tensile or compressive tests [108]. Rather than having constant values, they will vary according to the thermo-mechanical loading path history [108]. In a recent work [108], the apparent Young's modulus of dense LSCF was evaluated from the slopes of different parts of the stress–strain curves, namely, the initial and the last parts of the loading curve and beginning part of the unloading curve. In fact, the unloading Young's modulus, which appears to be mainly related to the elastic response without significant energy consumed by domain reorientation, was generally higher than the loading ones.

A summary of elastic moduli of selected LSCF material variants with different porosity measured with different methods is given in Table 1.2. In general, elastic modulus decreases with increasing porosity and with increasing temperature below ~700 °C. A sudden increase of the elastic modulus occurs above ~700 °C due to the phase transition of LSCF perovskite from rhombohedral phase to cubic phase. The temperature dependency of elastic modulus measured by impulse excitation method is shown in Figure 1.16, as well as the internal friction, which is a measure of the damping of the resonance frequency. Overall elastic moduli measured with different test methods show significant differences especially at low porosity (below 10%). For all the measurements with porosity lower than 10%, nanoindentation method yielded the highest moduli compared to other methods.

Table 1.2 Reviewed elastic modulus data of selected LSCF materials.

Composition	E [GPa]	Porosity	T [°C]	Test method	Ref.
$La_{0.8}Sr_{0.2}Co_{0.2}Fe_{0.8}O_3$	161	0.041	RT	Resonance (IET)	Chou et al. [109]
$La_{0.6}Sr_{0.4}Co_{0.2}Fe_{0.8}O_3$	152	0.046			
$La_{0.4}Sr_{0.6}Co_{0.2}Fe_{0.8}O_3$	167	0.035			
$La_{0.2}Sr_{0.8}Co_{0.2}Fe_{0.8}O_3$	188	0.051			
$La_{0.58}Sr_{0.4}Co_{0.2}Fe_{0.8}O_{3-\delta}$	78	0.06	RT	Ring-on-ring bending	Huang et al. [100]
	62		200		
	63		400		

	67		600		
	70		700		
	115		800		
$La_{0.6}Sr_{0.4}Co_{0.2}Fe_{0.8}O_{3-\delta}$	164	0.02	23	Resonance (IET)	Kimura et al. [110]
	158		100		
	149		200		
	130		300		
	115		400		
	107		450		
	102		500		
	100		550		
	101		600		
	104		650		
	105		700		
	130		750		
	147		800		
	157		850		
	165		900		
$La_{0.6}Sr_{0.4}Co_{0.2}Fe_{0.8}O_{3-\delta}$	60	0.06	22	Ring-on-ring bending	Lipińska-Chwałek et al. [111]
	123		800		
	13	0.46	22		
	20		800		
$La_{0.6}Sr_{0.4}Co_{0.2}Fe_{0.8}O_{3-\delta}$	147	0.052	RT	Resonance (IET)	Chen et al. [112]
	174	0.052		Nano-indentation	
	122	0.152			Chen et al. [113]
	90	0.241			

	48	0.398			
	32	0.469			
$La_{0.58}Sr_{0.4}Co_{0.2}Fe_{0.8}O_{3-\delta}$	45 ± 20	0.041	RT	Ring-on-ring bending	Pećanac et al. [32]
$La_{0.6}Sr_{0.4}Co_{0.2}Fe_{0.8}O_{3-\delta}$	12 ± 4	0.46			
$La_{0.58}Sr_{0.4}Co_{0.2}Fe_{0.8}O_{3-\delta}$	121	0.06	20	Compressive test	Araki et al. [98]
	92		200		
	88		300		
	101		600		
	105		800		

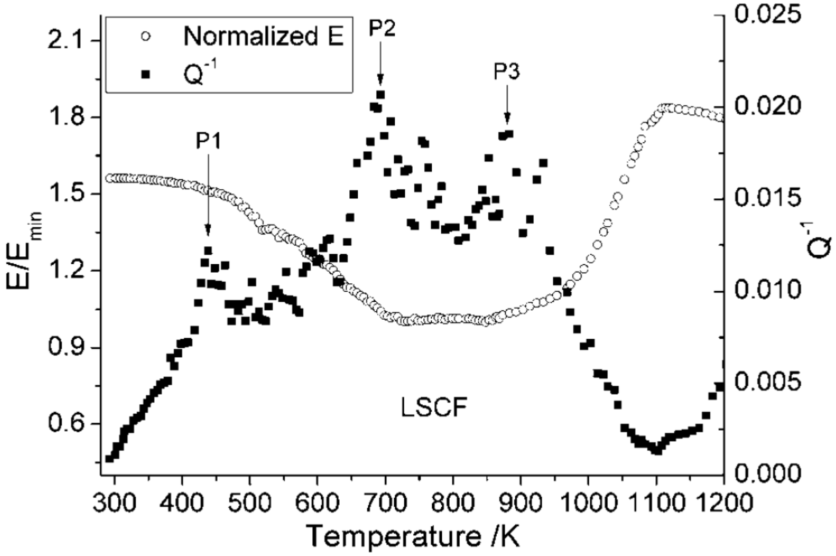

Figure 1.16 Young's modulus and internal friction of $La_{0.58}Sr_{0.4}Co_{0.2}Fe_{0.8}O_{3-\delta}$ (LSCF) as a function of temperature [45].

Considering the working conditions of membrane materials, elevated temperatures and high pressure, especially the creep behavior needs to be investigated, since it is one of the key parameters to define their lifetime limits. Creep rates of selected LSCF materials for membrane application are compiled in Table 1.3 and Figure 1.17 with the corresponding applied stresses and temperatures.

Table 1.3 Review of creep rates of dense LSCF [102].

Composition	Porosity	Grain size [μm]	Stress [MPa]	*T* [°C]	Creep rate [s^{-1}]	Ref
$La_{0.58}Sr_{0.4}Co_{0.2}Fe_{0.8}O_{3-\delta}$	0.034	0.6 ± 0.2	20	750	1.9×10^{-10}	Huang et al. [102]
				800	2.2×10^{-10}	
				850	9.3×10^{-10}	
				900	6.3×10^{-9}	
				950	4.2×10^{-8}	
			30	750	4.2×10^{-10}	
				800	5.3×10^{-10}	
				850	2.2×10^{-9}	
				900	1.5×10^{-8}	
			50	750	8.9×10^{-10}	
				800	1.8×10^{-9}	
				850	6.3×10^{-9}	
				900	5.3×10^{-8}	

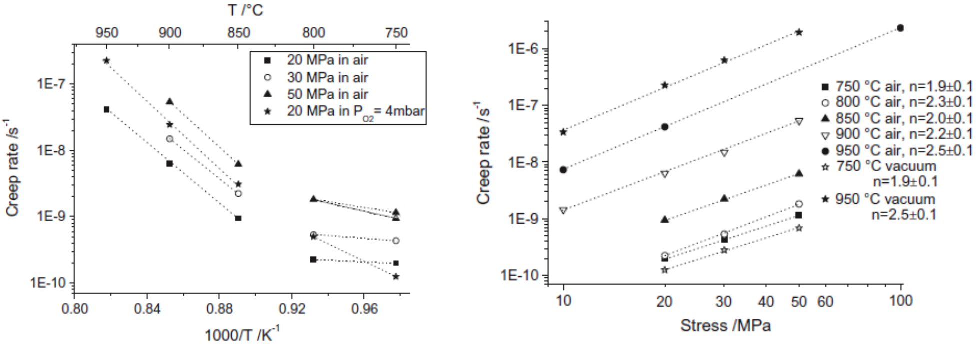

(a) (b)

Figure 1.17 Steady-state creep rate of LSCF under compressive stress in air: (a) creep rate as a function of 1/T, (b) creep rate as a function of the applied stress. [102]

Huang et al. [102] reported high temperature (750 to 950 °C) creep studies in air and vacuum (p_{O2} = 4mbar) on A-site deficient $La_{0.58}Sr_{0.4}Co_{0.2}Fe_{0.8}O_{3-\delta}$ (LSCF58) revealed an increase of the creep rate with decreasing oxygen partial pressure [102]. The creep rate in vacuum was about one order of magnitude higher compared to the creep rate in air although the same cubic structure exists. Furthermore, a transition in the apparent activation energy between 800 and 850 °C was reported for both air and vacuum. The apparent activation energy was ~ 250 kJ/mol in the temperature range 700 to 800 °C under vacuum and ~ 480 kJ/mol for the temperature range of 850 to 950 °C for both atmospheres. The stress exponent of the creep law was in the range 1.9 to 2.5 for all temperatures, which apparently excluded a transition of creep mechanism.

In order to evaluate the long-term performance of the membrane structure, a maximum tolerable creep deformation of 1 % per year (3.2×10^{-10} s^{-1}) in a compressive mode is suggested to warrant reliable long term operation [114–116]. Furthermore, this stress values are selected after calculations by Schulz et al. [52], who obtained 30 MPa for the loading state that can appear during membrane operation.

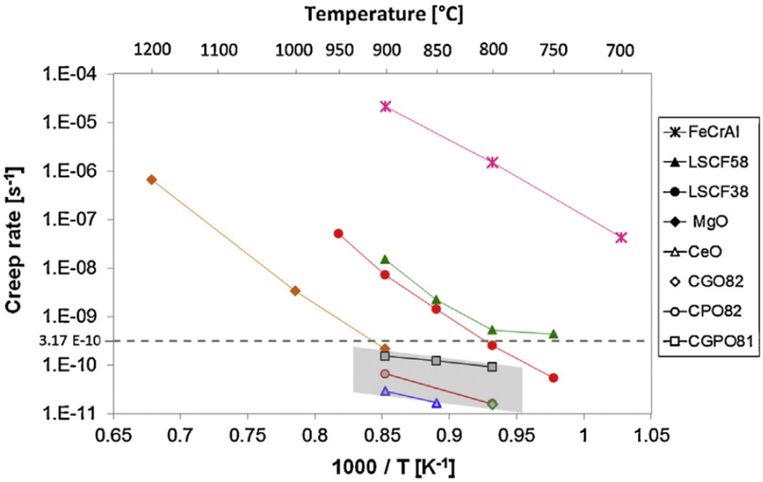

Figure 1.18 Comparison of steady-state creep rates of various membrane and substrate materials investigated under compressive stress of 30 MPa in air [117].

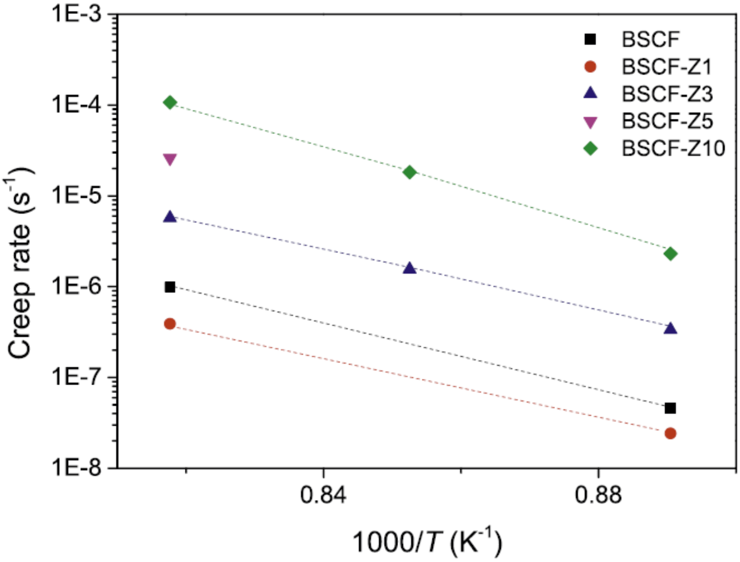

Figure 1.19 Steady-state creep rate of BSCF [115] and BSCF-Z100·X (cooling runs) [118].

Figure 1.18 illustrates a comparison of creep rates of different materials from literature [117]. The dashed line indicates the 1% creep strain per year limit. From the creep data, cerium oxides show the lowest creep rates and FeCrAlY alloy showed stronger creep deformations than the ceramics (in the case of a porous substrate even higher creep rates can be expected). The tests performed at 700 °C, 800 °C and 900 °C resulted in significantly higher creep rates than the tolerable 1% per year. The creep rates of LSCF38 and LSCF58 are all higher than the other ceramic membrane materials and higher than the 1% per year criteria, which can be critical for application. Therefore, a reduction of the application stresses or operation temperatures appears to be necessary. Figure 1.19 shows the creep rate of $Ba_{0.5}Sr_{0.5}Co_{0.8}Fe_{0.2}O_{3-\delta}$ (BSCF) [115] and $Ba_{0.5}Sr_{0.5}(Co_{0.8}Fe_{0.2})_{1-x}Zr_xO_{3-\delta}$ (BSCFZ) [118] upon cooling from literature. In fact, compared to the ceramic materials results in Figure 1.18, BSCF and BSCFZ have even higher creep rates when the temperature is higher than 850°C.

1.5. 3 mol% Y_2O_3 stabilized ZrO_2 (3YSZ)

Yttria-stabilized zirconia (YSZ) is widely used and studied due to its high ionic conductivity at elevated temperatures [119], high chemical inertness and its hardness [120]. Its applications include as electrolytes in solid oxide fuel cells [121], in chemical sensors [122,123], in thermal barriers coating [124,125], and to create optical devices like switchable mirrors or filters [126].

Pure zirconia (ZrO_2) has three different polymorphs, i.e., monoclinic (m), tetragonal (t) and cubic (c) phases, as illustrated in Figure 1.20. These phases can be obtained depending on temperature and compositional ranges under equilibrium conditions [127]. By doping zirconium oxide, ZrO_2, with yttrium oxide, Y_2O_3, a tetravalent ion (Zr^{4+}) is substituted by a trivalent one (Y^{3+}). Due to charge neutralization, oxygen vacancies are formed, increasing the ionic conductivity as well as stabilizing the desired tetragonal or cubic structures [128].

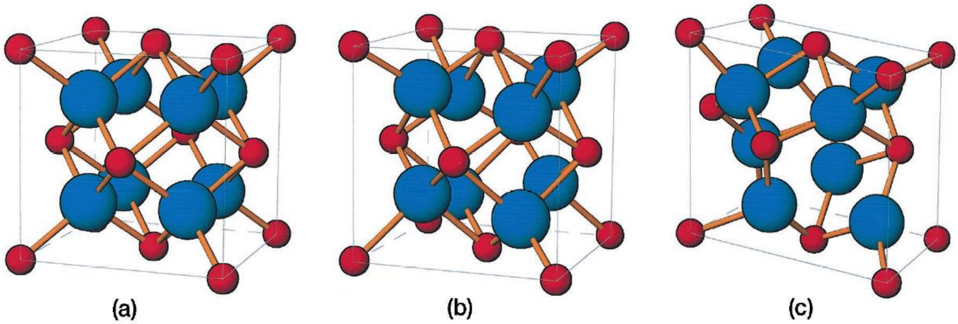

Figure 1.20 Schematic representation of the three ZrO_2 polymorphs: (a) cubic, (b) tetragonal, and (c) monoclinic. [129]

Overall, 8 mol% yttria stabilized zirconia (8YSZ) with cubic structure has the highest ionic conductivity and good chemical stability over wide temperature and oxygen partial pressure range [130], while the highest fracture toughness of ZrO_2 is achieved by doping with 3 mol% yttria [131], leading to its use as anode substrate material in solid oxide fuel cells [132]. According to ZrO_2–Y_2O_3 phase diagram [133], at concentration of 3–7 mol% Y_2O_3, both cubic and tetragonal phases can be retained in the microstructure. The microstructure of these ceramics consists of a cubic phase matrix in which tetragonal phase is dispersed, which is termed as partially stabilized zirconia (PSZ) [134]. In a crack-growth associated stress state, a transformation of the tetragonal phase to monoclinic phase occurs, which is the basics of the so-called transformation toughening [129,131,135].

In particular, 3 mol% yttria stabilized zirconia (3YSZ) exhibits an extremely fine grained microstructure, which yields excellent mechanical properties including high toughness, and strength and a composition containing only the tetragonal phase at room temperature, therefore, often being called tetragonal zirconia polycrystal (TZP).

Variations of elastic moduli (*E**) and shear moduli (*G**) of 3YSZ and 8YSZ with porosity as determined by impulse excitation technique (IET) are shown in Figure 1.21 [136]. The “zero porosity” elastic moduli from these experiments were 217 GPa for 3YSZ and 220 GPa for 8YSZ [136].

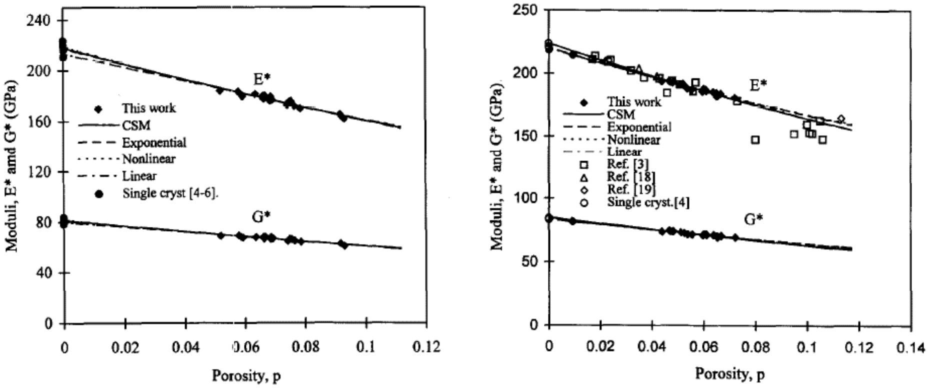

(a) (b)

Figure 1.21 Variation of elastic moduli (*E**) and shear moduli (*G**) with porosity of (a) 3YSZ and (b) 8YSZ [136].

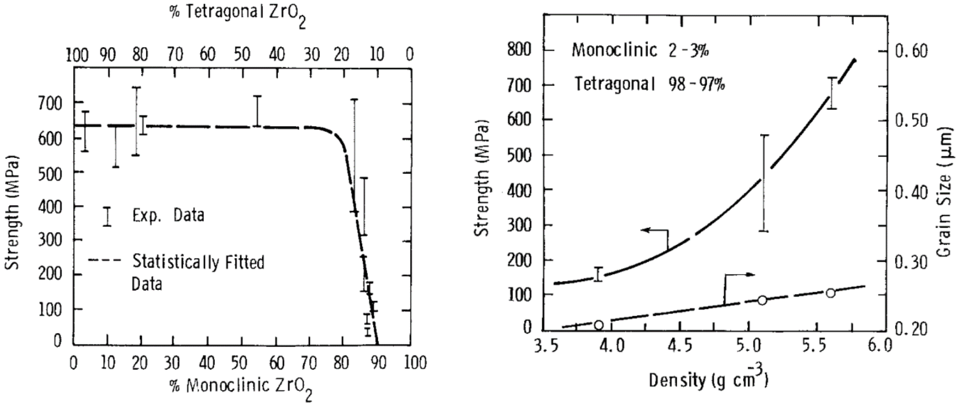

(a) (b)

Figure 1.22 Strength of ZrO_2 ceramics as measured by symmetrical biaxial flexure test: (a) strength versus tetragonal phase content (density 5.6 ± 0.1 $g\cdot cm^{-3}$), (b) strength and grain size as a function of density (tetragonal content ≥ 70%). [135]

The partially stabilized zirconia (PSZ) ceramics often show high strengths and in fact generally, high tetragonal phase containing ceramics possess a high strength, whereas high monoclinic phase containing ceramics exhibit a lower strength, as illustrated in Figure 1.22(a) [135]. When the zirconia specimens contain a monoclinic phase of ~ 90%, the strength is only about 100 MPa. When the tetragonal content is increased to ~ 30%, the strength increases rapidly and a final high strength about 700 MPa is maintained for tetragonal contents between 30 and 100%. Besides, the strength increases with increasing density as often observed for ceramic materials, see Figure 1.22(b) [135].

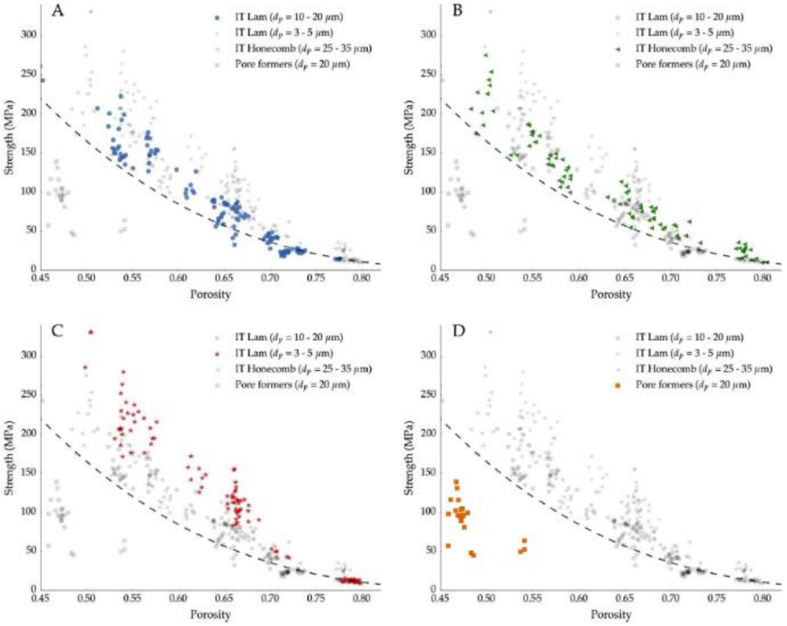

Figure 1.23 Compressive strength dependence on porosity in freeze-cast 3YSZ samples frozen at a rate of 2 K/min (A), 25 K/min (C), and with a honeycomb morphology (B). Isotropic samples by sacrificial method are also represented (D). The experimental points of the other conditions are represented in grey for comparison. [137]

In the work of Seuba et al. [137], the fracture behavior of undirectional porous freeze-cast 3YSZ ceramics was investigated with uniaxial compresive test. Their compressive strength dependence on porosity in different freeze-cast samples is shown in Figure 1.23. Samples with porosity of 45% revealed varying compressive strength between 50 – 300 MPa. In another work of Seuba et al. [138], they suggested that wall thickness is the key morphological influence parameter on mechanical reliability and strength of macroporous materials. Both Weibull modulus and strength tended to increase for smaller wall thicknesses and this was attributed to the reduced probability of finding a catastrophic defect in thinner walls. They also suggested that strength in a freeze-cast 3YSZ is mainly determined by the total porosity and the effect of morphological parameters like wall thickness is relatively weak.

The creep behavior of 3YSZ has been widely studied due to the fact that it was the first true polycrystalline ceramic shown to be superplastic with an elongation of > 100% [139–143]. A comparison of the creep strain rates measured at 1450°C from different publications is given in Figure 1.24a. The high temperature creep was reported to be related to a diffusion controlled behavior [140,141], with a change in the stress exponent from n ~ 2 at high stresses to n ~ 3 at low stresses [140,141,144] (Figure 1.24b) and the activation energy being essentially constant at ~ 550 $kJ{\cdot}mol^{-1}$ [141,145,146]. But in these studies, the test temperature was much higher than the working temperature of an OTM component.

In the frame of solid oxide fuel cells (SOFC) technology, the anode support usually consists of either nickel and 8 mol% yttria stabilized zirconia (Ni-8YSZ) or nickel and 3 mol% yttria stabilized zirconia (Ni-3YSZ). The creep behavior of such porous Ni-YSZ composites has been intensively studied [93,147,148] and a similar conclusion has been drawn based on the studies of Ni-3YSZ and Ni-8YSZ, which is that the overall creep behavior of the composites is primarily controlled by the ceramic matrix phase [147,148].

In a SOFC component, the material is under load at the similar working temperature (~ 800°C) as in an OTM module.

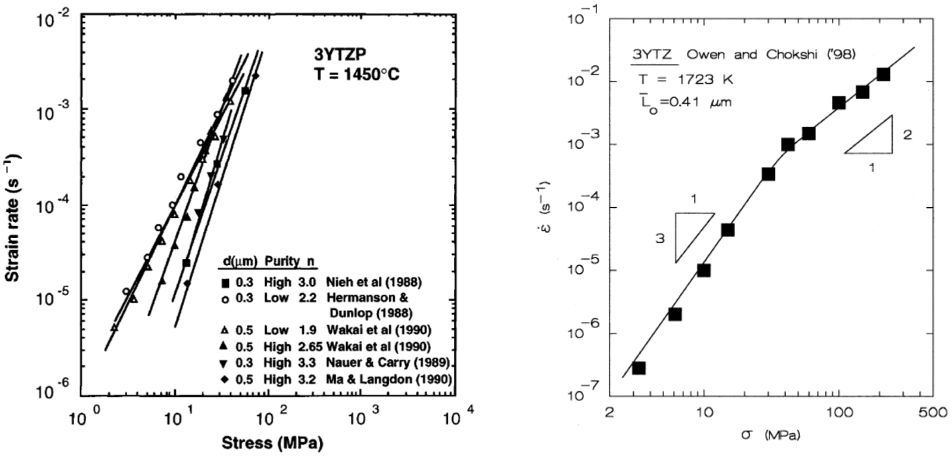

(a) (b)

Figure 1.24 Creep rates of 3YSZ at 1450°C: (a) strain rate vs stress for low- and high-purity 3YSZ tested [149], (b) variation in strain rate with stress [141,142].

Morales-Rodriguez et al. [147] reported the compressive creep properties of Ni-3YSZ in temperatures ranging from 950°C to 1250°C in reduced atmosphere, as shown in Figure 1.25. At 1200 - 1250°C under stresses from 3 to 14 MPa, average values of stress exponent $n = 4.0 \pm 0.4$ and activation energy $Q = 610 \pm 20$ kJ/mol were obtained for the materials with 20% Ni cermet, while average values of $n = 3.9 \pm 0.1$ and $Q = 640 \pm 50$ kJ/mol were obtained for the materials with 40 % Ni. Higher Ni amount resulted in higher creep rates. Both creep parameters decreased with increasing stress and/or temperature, similar as reported for high-purity monolithic YSZ [147].

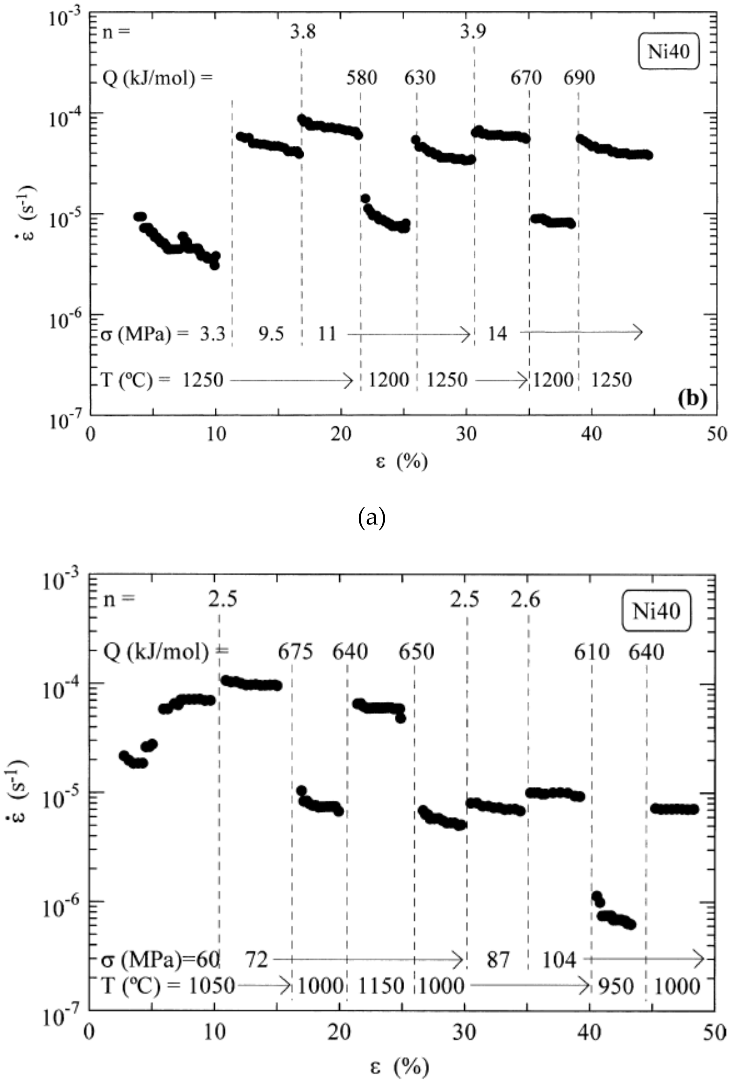

(a)

(b)

Figure 1.25 Strain rate vs strain curve for Ni-3YSZ with 40% Ni: (a) deformed between 1200 and 1250°C under low stresses, (b) deformed between 950 and 1150°C under high stresses. [147].

Based on the fact that the creep behavior of the Ni-YSZ composites is primarily controlled by the ceramic matrix phase [147,148], Kwok et al. [93] applied three-dimensional (3D) microstructural simulation on porous Ni-YSZ materials. 3D image data of the Ni–3YSZ and Ni–8YSZ samples was acquired by FIB serial sectioning, as shown in Figure 1.26. The creep responses by numerical homogenization of Ni and dense and porous YSZ are given in Figure 1.27. It shows that the creep rate of the Ni is about 9 and 7 orders of magnitude faster than that of 3YSZ and 8YSZ, respectively. The creep rates of porous YSZ differ from that of a theoretically dense material, as expected. The similar strain rates of porous Ni-8YSZ and porous 8YSZ indicated that the YSZ phase is essentially carrying most of the applied load.

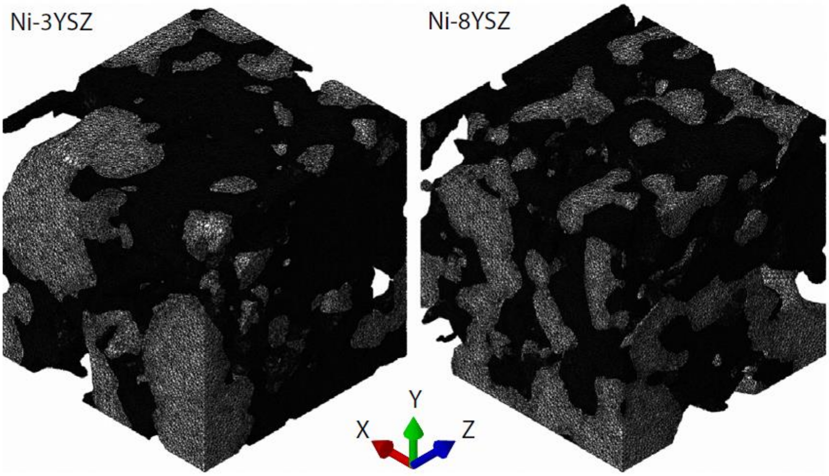

Figure 1.26 Finite element mesh of reconstructed microstructures. The Ni and YSZ phases are colored white and grey respectively [93].

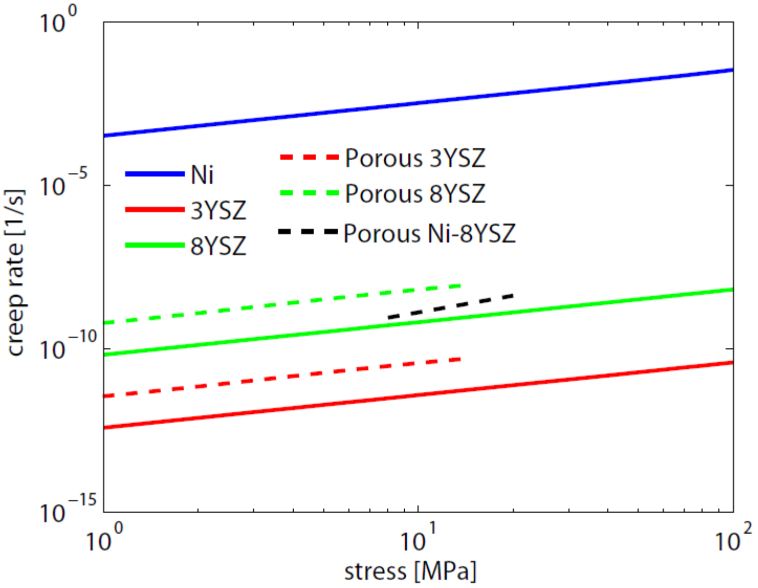

Figure 1.27 Creep rate of Ni, 3YSZ, and 8YSZ at 800°C for the relevant stress range [93,148].

Chapter 2.

Experimental

2.1. Materials production

Within the framework of the present thesis, $La_{0.6}Sr_{0.4}Co_{0.2}Fe_{0.8}O_{3-\delta}$ (LSCF) samples with different porosity and different porous structures, produced at the IEK-1 (Forschungszentrum Jülich) as porous substrate material, were tested with respect to elastic, fracture and creep behavior with bending and compressive tests. Furthermore, 3 mol% Y_2O_3 stabilized ZrO_2 (3YSZ), produced by the Univerity of Valencia, was also tested as porous substrate material with different porosity and different porous structures to reveal the effect of porosity and porous structure on mechanical behavior (elastic modulus and fracture strength from bending test) comparing with the effect on gas permeability behavior. Whereas for LSCF the work mainly concentrated on the effect of the porous structures onto the creep behavior, for 3YSZ the work concentrated mainly on the correlation of mechanical parameters and functionally important gas permeability, hence offering via the combination of both studies a wider view considering a broad range of mechanical properties from room temperature to application relevant temperatures, the relationship to different pore arrangements and the gas permeability which should be optimized to warrant a high permeation of the layered membrane arrangement.

2.1.1. $La_{0.6}Sr_{0.4}Co_{0.2}Fe_{0.8}O_{3-\delta}$ (LSCF)

$La_{0.6}Sr_{0.4}Co_{0.2}Fe_{0.8}O_{3-\delta}$ (LSCF) samples with different microstructures were produced at IEK-1 by different synthesis methods, including dry pressing, tape- and freeze-casting.

2.1.1.1. LSCF-PS (pressed LSCF samples)

To obtain a microstructure with round shaped pores, LSCF was blended with 10 and 30 wt% Spheromers CA15 from (MICROBEADS) with a diameter of 15 µm as pore former. Phase pure LSCF powder delivered by Solvay with an average particle size of 2.5 µm and a specific surface area of 2 m^2 was used. Subsequently the powder was uniaxial dry pressed to bars (4x4x30 mm^3) using a pressure of 50 MPa and sintered at 1250°C for 5 h. Spheromeres leaving ball shaped pores after burn out, providing a closed or open porosity, depending on the ratio of pore former to ceramic powder.

2.1.1.2. LSCF-TCL (tape-cast laminated supports) and -DPD (Sandwich samples)

Supports with membrane were also manufactured by a tape-cast process. Sequential tape-casting was employed to manufacture sheets of asymmetric membranes as described by Schafbauer et al. [150]. For this purpose, two slurries were produced. The slurry for membrane manufacturing contained no pore former, while the slurry for support production contained 30 wt% corn starch in relation to ceramic powder. Supports were cast with a doctor blade gap of 1.9 mm. For all samples, phase pure LSCF powder delivered by Solvay with an average particle size of 2.5 µm and a specific surface area of 2 m^2 was used.

Supported membranes were cast by the two-step sequential tape-cast procedure, casting first the thin membrane layer using slurry without pore former and a doctor blade gap of 1.9 mm. After drying the corn starch containing slurry was cast on top of the membrane foil again using a doctor blade gap of 1.9 mm.

After air drying, support samples and supported membranes were cut from the green tape. To receive a sufficient thickness for the porous material two support foils were laminated together. For manufacturing of the membrane sandwich for creep rupture tests, supported membranes were laminated support to support with the membrane on the outer side. Lamination took place at 80 °C and a pressure of 2000 N/m^2. Sintering of laminated supports and laminated supported membrane sandwiches was performed at 1300°C for 5 h. Burn out of corn starch resulted in a well distributed network of pore channels with varying pore opening diameter after burn out and sintering [33].

Sandwich samples of $Ba_{0.5}Sr_{0.5}Co_{0.8}Fe_{0.2}O_{3-\delta}$ (BSCF) with porous matrix and dense layers on both side for creep rupture testing were also produced by the procedure described above. A detailed description regarding manufacturing of BSCF sandwiches can be found in [151].

2.1.1.3. LSCF-TCR [31]

Porous specimens were prepared by tape-casting using $La_{0.6}Sr_{0.4}Co_{0.2}Fe_{0.8}O_{3-\delta}$ powder (H.C. Starck, Germany). A solvent based slurry with 20 wt% rice starch as pore forming agent in relation to the ceramic powder was used for tape-casting. Casting was performed by a doctor blade procedure with a casting gap of 700 µm. Details of the slurry preparation procedure as well as the ingredients can be found in [11,150]. After drying the flexible tape was cut to stripes and rolled to cylinders. After debindering, the samples were sintered at 1200 °C for 5 h in air resulting in a winding thickness of ~ 120 µm (Figure *2.1*).

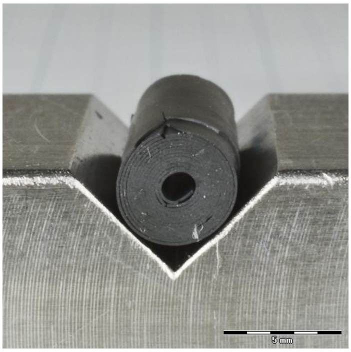

Figure 2.1 Rolled porous LSCF sample [31].

2.1.1.4. LSCF-FC (freeze-cast samples)

Freeze-cast porous LSCF samples were obtained by freezing a ceramic water based slurry in liquid nitrogen. For all samples, phase pure LSCF powder delivered by Solvay with an average particle size of 2.5 µm and a specific surface area of 2 m^2 was used. The slurry contained LSCF ceramic powder, binder (2.5 wt% PEG4000S, Clariant) and dispersant (2 wt%Dolapix C64, Zschimmer & Schwarz GmbH&Co). To vary the porosity the solvent – ceramic ration was varied using 25 and 30 wt% LSCF powder, resulting in a porosity of 43 and 30 % respectively.

An environmentally friendly water suspension containing the LSCF ceramic powder and organic additives as binder (2.5 wt% PEG4000S, Clariant) and dispersant (2 wt% Dolapix C64, Zschimmer & Schwarz GmbH&Co) was prepared and mixed in a planetary mixer. The slurry was poured into a Teflon mold attached to an aluminum base cooled at -50 °C that quickly freezes the solvent, from bottom to top. After complete freezing, the sample was placed in a freeze dryer (Martin Christ Epsilon 2-4) and ice crystals were sublimated at -22 °C (0.1 mbar) within 24 hours. The sample was then pre-sintered at 1200 °C under air during 5 hours, a step used to get a robust porous support for membrane layer deposition. Afterwards, the sample was sintered at 1280 °C, the final manufacturing temperature for dense membranes, however, a dense membrane layer was not applied to the current specimens since it would complicate the mechanical analysis of the substrate material.

2.1.2. 3 mol% Y_2O_3 doped ZrO_2 (3YSZ)

Pressing / sintering and freeze-cast have been utilized at Universidad Politécnica de Valencia, Institute of Chemical Technology (ITQ), Valencia, Spain, as conventional and original ceramic shaping methods, respectively, based on 3 mol% Y_2O_3 doped ZrO_2 (3YSZ) powder. Details on materials preparation and testing are given in the following sections.

Freeze-cast 3YSZ

Freeze-cast samples were fabricated as follows: The 3 mol% Y_2O_3 doped ZrO_2 (3YSZ) powder obtained from Tosoh was ball-milled in acetone during 48 h to ensure homogeneity and a final average particle size of about 2 μm. Porous monoliths were elaborated by ice-templating using the freeze-cast technique according to optimized samples fabricated in previous works [152,153]. Basically, a slurry containing the ceramic powder, water (30-40 wt%) as solvent, a polyacrylate-based dispersing agent (1-4 wt%), polyethylene glycol (1-4 wt%) (Sigma-Aldrich) and zirconium acetate complex (ZRA from Sigma-Aldrich, 24g.L^{-1}) as structuring agent if desired was stirred for 24 h to get a good particle distribution. In order to evaluate the influence of the porosity percentage over the mechanical properties, samples with different initial ceramic powder loading of 57, 60, 63, 66 and 70 wt% have been fabricated. The shaping process was as follows: the slurry was poured into a Teflon mold to get a sample of 1 cm height and cooled using copper rod cooled by liquid nitrogen. After complete freezing, the samples were removed from the mold and ice crystals were sublimated by freeze drying at -53°C and reduced pressure during 24 h using a Scanvac commercial freeze-dryer. The samples were then sintered at 1390°C under air during 6 h. Both heating and decreasing ramps were 2 K/min. To ensure that only the steady-state anisotropic structure was tested, disc-shape samples were cut out from the middle part of the cylinder samples, to exclude the denser top section as well as the isotropic and cellular zones [154,155]. The final diameter of the sample was 10 mm and the final thickness of 1 mm was adjusted by grinding the sample firstly by grinding papers from P#120 to P#1000 and then by a final cloth polishing in 5 μm, 2 μm and 1 μm diamond suspension. Debris was removed by acetone cleaning followed by ultrasonic cleaning and drying at 60°C.

The influence of the presence of a dense top layer over the mechanical properties has also been studied. For this, a slurry made of an 8YSZ powder from Tosoh (previously ball milled during 24 h in acetone) and a binder (6wt% ethylcellulose in terpineol) in a

50:50 weight ratio has been prepared and screen-printed over the porous freeze-cast support. A list of samples and associated features is given in Table 2.1.

Pressing & Sintering

Pressed and subsequently sintered porous 3YSZ samples were fabricated based on the same 3YSZ powder from Tosoh used for the fabrication of freeze-cast samples. A mixture of 3YSZ powder and circular PMMA particles ($Ø_{50}$ = 1.5 µm) pore former agent was ball-milled during 24 h to ensure homogeneity and uniaxally pressed into a 20 mm diameter mold under 150 kN for 3 min. After unmolding, samples were submitted to debinding and sintered in a one-step thermal treatment during 6 h at 1390°C to guarantee good mechanical stability. Both heating and decreasing ramps were 20 h. The final diameter and thickness were of 16 mm and 2 mm, respectively. Details see Table 2.1.

Table 2.1 List of samples and associated features.

Abbr.	Shaping technique	Powder loading [wt%]	Powder loading [vol%]
FC57	Freeze-cast	57	18
FC60		60	20
FC60z		60	20
FC63		63	22
FC66		66	24
FC70		70	28
FC+TL	Freeze-cast + screen-printing	57	18
PS42	Pressing & sintering	42	11

2.2. Mechanical characterization

2.2.1. Ring-on-ring bending tests

Ring-on-ring bending tests were performed on an electromechanical test machine (Instron 1362). The central displacement of the specimens was measured by a sensor in contact with the lower (side in tension load) surface of the sample. The displacement was monitored with a ceramic extension rod attached to a linear variable differential transformer (Sangamo, LVDT, range ± 1 mm with precision ± 1.25 μm). The load was applied with a 1.5 kN load cell (Interface 1210 BLR). A half-sphere was used for the loading set-up in order to assure the alignment and eliminate uncertainties and scattering in obtained results. For the ring-on-ring test, disc specimens were used. Tests were carried out from room temperature up to maximally 1000 °C. The temperature was monitored close to the specimen surface with a type K thermocouple.

The ring-on-ring experimental set-up is illustrated in Figure 2.2. In this test, a disc shape sample is loaded between a loading ring and a support ring. The linear bending theory has been applied for the determination of fracture stress.

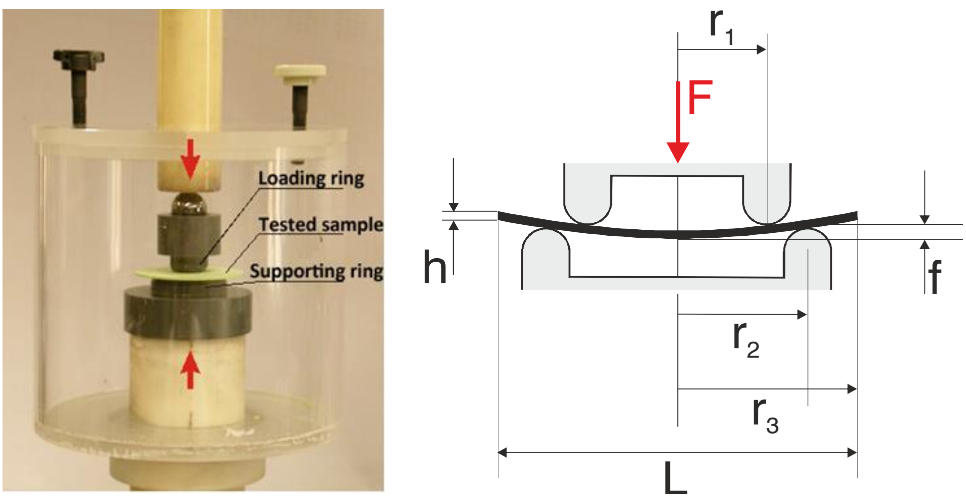

Figure 2.2 Experimental set-up of ring-on-ring bending test.

In general, the elastic modulus is derived from the linear part of the load displacement curve (at low loads a non-linearity in the curve might be observed due to the specimen's unevenness) after ASTM C1499-05 [156].

$$E = \frac{3(1-\nu^2)\cdot r_1^2\cdot \Delta F}{2\pi\cdot \Delta f\cdot h^3} \times \left[\left(\frac{r_2}{r_1}\right)^2 - 1 - ln\left(\frac{r_2}{r_1}\right) + \frac{1}{2}\left(\frac{1-\nu}{1+\nu}\right)\times\left(\frac{r_2^2-r_1^2}{r_3^2}\right)\times\left(\frac{r_2}{r_1}\right)^2\right] \tag{2.1}$$

where ΔF is the force difference and Δf the corresponding displacement change of the linear part of the load-displacement curve used for calculation, h the specimen thickness, r_1, r_2 and r_3 are radius of loading ring, supporting ring and specimen, respectively.

For linear behavior, as it might be expected for brittle fracture, the maximum stress is constant over the tensile loaded surface inscribed by the loading ring:

$$\sigma_f = \frac{3(1+\nu)F_f}{2\pi\cdot h^2}\times\left[ln\left(\frac{r_2}{r_1}\right) + \left(\frac{1-\nu}{1+\nu}\right)\times\frac{r_2^2-r_1^2}{2r_3^2}\right] \tag{2.2}$$

where F_f is the fracture load.

Due to the high dispersion of the mechanical results, statistical assessments were additionally applied using the two-parameter Weibull distributions as described in Section 1.2.3.

Ring-on-ring bending fracture tests were performed for both LSCF and 3YSZ samples. The average dimensions of the samples as well as the tested specimen number of the different tested batches are summarized in the following table. Sample dimension need to meet the requirement according to DIN 51105:2010-08 [157]. Prior to test, samples were grinded and polished in order to achieve flat and parallel surfaces as well as homogeneous thickness along the discs also according to DIN 51105:2010-08 [157].

3YSZ samples produced by freeze-cast and pressing and sintering, as described in Section 2.1.2 were all tested at room temperatures.

Table 2.2 3YSZ samples for ring-on-ring bending test at room temperature.

	Number of valid specimens	**Production method**	**Specimen Diameter [mm]**	**Specimen Thickness [mm]**	**Porosity [%]**
FC57	7	Freeze-cast	15.3 ± 0.1	1.4 ± 0.1	65.1 ± 2.5
FC60	8		15.4 ± 0.1	1.5 ± 0.1	61.8 ± 3.0
FC63	8		15.4 ± 0.2	1.7 ± 0.3	56.9 ± 2.7
FC66	6		15.4 ± 0.1	1.7 ± 0.1	50.2 ± 2.2
FC70	8		15.5 ± 0.1	1.5 ± 0.2	43.5 ± 2.9
FC60a	15		15.1 ± 0.2	1.0 ± 0.1	61.3 ± 2.7
FC60b	13		15.1 ± 0.2	1.1 ± 0.1	61.3 ± 2.7
FC60z	5		16.5 ± 1.2	1.2 ± 0.1	45.7± 3.6
FC+TL	9	Freeze-cast + screen printing	15.2 ± 1.1	1.5 ± 0.1	--

PS42	8	Pressing and sintering	16.1 ± 0.1	2.0 ± 0.1	46.4 ± 2.3

2.2.2. Three-point bending test

In case of bar-shaped specimens, three-point bending test are performed with the Instron 1362 machine. The testing head is changed, while the auxiliary equipment (differential transformer, ceramic extension rod, loading cell, thermocouple) remain the same. The experiments were carried out according to the ASTM C1161 standard [158]. The experimental set-up of three-point bending test is illustrated in Figure 2.3. The corresponding relationships of fracture stress, Young's modulus and fracture strain are listed below.

$$\sigma = \frac{3 \cdot \Delta F \cdot L}{2 \cdot b \cdot h^2} \tag{2.3}$$

$$E = \frac{\Delta F \cdot L^3}{4 \cdot b \cdot h^3 \cdot \Delta f} \tag{2.4}$$

$$\varepsilon = \frac{\sigma}{E} = \frac{6 \cdot h \cdot \Delta f}{L^2} \tag{2.5}$$

Where ΔF is the force in N and Δf is the deflection in mm of the linear region; L, b and h are length, width and height of the tested specimen in mm. The region of maximum stress is located in the middle of the tensile-loaded specimen side (central line of a bar specimen).

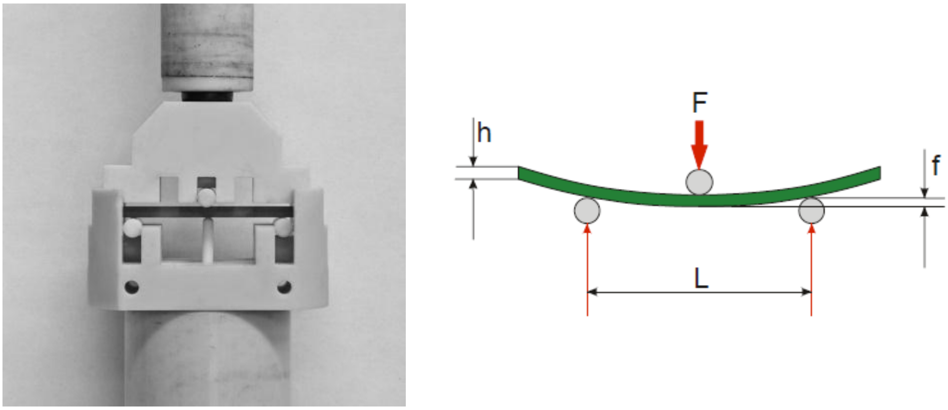

(a) (b)

Figure 2.3 Experimental set-up of three-point bending test.

In order to assess if differences in creep behavior, i.e. the higher creep rates of porous substrate materials, can be critical for the structural stability of the dense layer in an asymmetric membrane, sandwich samples of BSCF and LSCF with porous matrix and dense layers (~20 μm) on both side were tested with three-point bending set-up with respect to the creep rupture behavior of the dense layer. The initial tests concentrated on BSCF, since due to the higher elevated temperature creep rates [115,118] of this material more pronounced effects were expected in shorter experimental times.

Experimental parameters along with the obtained central displacement as a measure of the creep deformation of the entire layered composite are given in Table 2.3. Both samples were tested at application relevant temperatures (> 750°C), and LSCF even at a slightly higher temperature and higher load to enhance creep effects, since in general LSCF possesses lower creep rates than BSCF under identical conditions.

Table 2.3 Experimental parameters of three-point bending creep rupture tests.

Materials	Geometry [mm^3]	Distance between supporting rods [mm]	Temperature [°C]	Time [h]	Load [N]	Note
BSCF	28.3×6.82×1.55	20	875	2	4	Central displacement 78 µm
LSCF-1	~39.8×6.83×1.83		955	-	-	Broken during loading
LSCF-2			955	92	4-8	Central displacement 164 µm
LSCF-3			~950	-	-	Broken during loading
LSCF-4				90	8	Thermal couple not in heating zone
LSCF-5					0	
LSCF-6			-	-	-	As-received

2.2.3. Compressive tests

Uniaxial compression tests were performed to evaluate the elastic behaviour and creep deformation of the LSCF samples with different porosity and porous structures. Before compressive creep testing, the upper and lower ends of the samples were grinded and polished to obtain plane-parallel surfaces.

2.2.3.1. *Elastic properties of freeze-cast LSCF*

In this part of the studies, the elastic behavior of porous freeze-cast LSCF perovskite at room temperature as characterized by a quasi-static hysteresis compression test in order to get insight into the influence of the ferro-elasticity on the apparent elastic parameters of such anisotropic materials. The LSCF powder was provided by Solvay where it was synthesized by solid state reaction. The measured average particle size was ca. 7 μm. Ice-templated porous LSCF supports were prepared using the freeze-cast technique. The sintered porous pellet was cut into one rectangular bar of 5.05×5.05×6.00 mm^3 for mechanical testing.

To evaluate the mechanical behavior, uniaxial compression tests were performed using a universal material testing machine (AGS-X, Shimadzu, Japan) at the Saitama University, Japan, which led to properties more representative of the global behavior than frequently used indentation testing [112,113]. Strain gauges (FLA, Tokyo Sokki, Japan) and a dynamic strain meter (DC-204R, Tokyo Sokki, Japan) were used, in which paired strain gauges were applied for each measurement to eliminate bending strains. One pair of strain gauges was glued along the loading direction to measure the longitudinal strain (ε_l), and a second pair was applied perpendicular to loading direction to assess the transverse strain (ε_t). Compressive stress (σ) was applied to the specimen at room temperature with a loading rate of 1 N/sec (0.039 MPa/s), followed by unloading at the same rate. For this study, a series of quasi-static hysteresis tests were performed. Such a quasi-static hysteresis test consist of several successive compressive tests: the specimen was loaded until a certain stress level is reached, after which the specimen was unloaded. This was repeated several times, while the maximum stress level was increased. The loading-unloading cycle was repeated with progressively increasing maximum stresses until fracture happened. The general idea was that during the loading certain damage processes take place, and it was assumed that during the unloading no extra damage growth occurs. The effects of the damage mechanics were then visualized by unloading the specimen and determining certain parameters, such as Young's modulus, permanent deformation or Poisson's ratio.

Here, the apparent Young's modulus E was calculated as the slope of the longitudinal strain ε_l - stress σ curves:

$$E = \frac{d\sigma}{d\varepsilon_l} \tag{2.6}$$

The apparent Poisson's ratio ν was derived from the differential of the strains in the transverse ε_t and longitudinal directions ε_l under uniaxial stress:

$$\nu = -\frac{d\varepsilon_t}{d\varepsilon_l} \tag{2.7}$$

The apparent shear modulus G and bulk K modulus, which relate to the change in size and shape, respectively, can be expressed in terms of the apparent Young's modulus and apparent Poisson's ratio via:

$$G = \frac{E}{2(1+\nu)} \tag{2.8}$$

$$K = \frac{E}{3(1-2\nu)} \tag{2.9}$$

2.2.3.2. *Compressive creep*

Aiming at a characterization of potential substrate materials, creep behavior of $La_{0.6}Sr_{0.4}Co_{0.2}Fe_{0.8}O_{3-\delta}$ samples with different porosity and different porous structures was investigated with uniaxial compressive set-up. Uniaxial compressive tests were carried out in IEK-2, Forschungszentrum Jülich, using an Instron 1362 electromechanical testing machine, equipped with a high-temperature furnace. Samples were mounted between alumina loading pistons via alumina half-sphere (from top) and plate (from bottom), as shown in Figure 2.4. For displacement measurements, a linear variable differential transformer (Sangamo, LVDT, range ± 1 mm, precision 1.25 µm) with alumina coupling rods was used. The load was determined with a 10 kN load cell (Interface 1210 ACK). The temperature was monitored during the test with a thermocouple located near the sample surface. The LVDT was assembled with the bottom of the half-sphere in the clamping device by an alumina rod so that the position change of the lower traverse relative to the upper specimen fixture was measured yielding information of the sample deformation. An annealing step was applied in beginning of each experiment for several hours in order to obtain thermal equilibrium of materials and to minimize chemical expansion effects as suggested by Rutkowski [159]. All tests were performed in the constant stress mode at constant temperature steps according to the general heating and loading profile illustrated in Figure 2.5. Also before each isothermal step an additional annealing period of 1 h was applied for minimizing thermal expansion effects of the testing machine that might affect the deformation rate. In some cases, cooling steps were also applied for the determination of creep rates. In all cases, each creep measurement was terminated after 24 h of a steady-state deformation or until an integral deformation of 100 μm was reached.

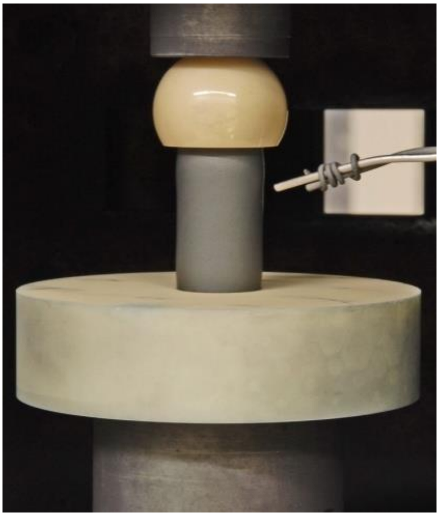

Figure 2.4 Compressive test set-up. The specimen is mounted between Al_2O_3 table and half sphere.

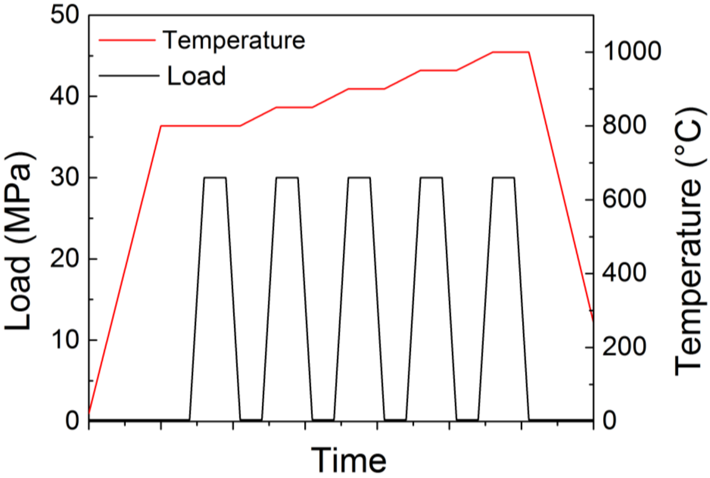

Figure 2.5 Typical heating and loading profile for compressive creep tests in constant load mode.

Creep tests were carried out in air under the application of an axial compressive load in the temperature range 750 to 1000 °C. For elevated temperature tests, a heating rate of 8 K/min was used. A compressive preload of 3 N (corresponding for an area of 20×10^{-6} m^2 to a stress of ~ 0.15 MPa) was applied during heating to keep the specimen fixed. To reach equilibrium condition at the test temperature, a dwell time of 1 h was chosen. Neglecting the area change of the samples by the creep deformation, the initial stress is used for the whole process. Stresses of 15 and 30 MPa were applied to determine the creep rate. Lower stresses did not yield sufficient deformations to determine accurate creep rates, higher stress could not be applied due to the brittleness of the highly porous specimens. Furthermore, this stress values are selected after calculations by Schulz et al. [52], who obtained 30 MPa for the loading state that can appear during membrane operation. Each creep measurement was terminated after 24 h of steady-state deformation or until an integral deformation of 100 μm was reached. For details on the creep testing procedure and instrumentation, see also [115,116].

The initial creep tests were carried out with LSCF-TCR samples, as described in Section 2.1.1. Two samples were tested but at slightly different temperatures. Sample 1 was tested at room temperature (20 °C), 750 °C, 800 °C, 900 °C during heating as well as 800 °C upon cooling; sample 2 was tested at 800 °C, 850 °C and 950 °C only during heating, where the test at 800 °C was carried out to verify the data obtained for the first specimen. Before and after the creep test, cross-sections of single small pieces of the samples were prepared and analyzed by scanning electron microscopy (SEM, Zeiss Supra 50). Porosity and grain size were assessed graphically from micrographs (Software AnalySIS). The average grain sizes were quantified from the SEM images, in terms of the equivalent circular diameter (ECD) values.

Later, aiming at a characterization of potential substrate materials, creep behavior of $La_{0.6}Sr_{0.4}Co_{0.2}Fe_{0.8}O_{3-\delta}$ samples with different porosity and different porous structures was investigated with uniaxial compressive set-up in succession, mainly in the temperature range 800 to 1000°C to avoid the low deformation rate below 800°C.

Detailed production parameters of the tested LSCF samples are given in Table 2.4. Seven batches of LSCF samples were tested, which were produced by different synthesis methods, including pressing and sintering, tape-cast and freeze-cast. Sample production has been introduced in Section 2.1.1. Sample ***PS90*** and ***PS70*** are pressed samples with solid loading of 90% and 70% respectively. ***TCR*** and ***TCL*** are tape-cast samples either rolled into a cylinder or laminated into bars. ***FC30V*** and ***FC25V/P*** are freeze-cast sample with solid loading of 30% and 25% respectively. Since freeze-cast material has anisotropic porous structure, the loading can be either ***V***ertical or ***P***arallel to the freeze direction. Therefore, the letter ***V*** and ***P*** in the sample labels indicate the loading directions. Porosity and grain size was determined by images analysis method based on SEM images.

Table 2.4. Details on the parameters of the tested LSCF samples.

	Dense	**PS90**	**PS70**	**TCR**	**TCL**	**FC30V**	**FC25V/P**
	Pressing and sintering			Tape-cast		Freeze-cast	
Powder	Spray drying			Spray drying	Solid state reaction	Solid state reaction	
Pore former	--	PMMA		Starch		Ice crystals	
Sintering temp./time	1250°C / 5h			1200°C / 5h	1300°C / 5h	1280°C / 5h	
Solid loading [wt%]	--	90	70	20	25	30	25

Porosity P [%]	5.3 ± 0.3	26.3 ± 1.7	62.5 ± 7.0	35.7 ± 1.3	37.0 ± 1.6	30.4 ± 1.4	43.4 ± 3.0
Grain size d [µm]	3.1 ± 0.2	1.8 ± 0.6	1.9 ± 0.1	0.60 ± 0.06	3.3 ± 0.1	3.0 ± 0.2	3.1 ± 0.5

The compressive creep rates were determined from the displacement-time curves recorded at each temperature using a linear fitting routine. The resulting strain rates were mathematically described by a simplified steady-state temperature activated Arrhenius approach [102,115–117,160]:

$$\dot{\varepsilon} = A\sigma^{n} exp\left(-\frac{E_a}{RT}\right) \tag{2.10}$$

where A is a constant, n the stress exponent, E_a the activation energy, and R is the universal gas constant. Applied stress σ and temperature T are the experimental input parameters. A $\ln\dot{\varepsilon} - \ln\sigma$ plot permitted a determination of the n value from the slope of the linear fit of experimental data measured at given temperature. The activation energy E_a was calculated from a semi logarithmic $\ln\dot{\varepsilon} - 1/T$ representation, where the slope yielded E_a/R.

2.3. Pressure drop measurement

Pressure drop measurements were performed at Universidad Politécnica de Valencia, Institute of Chemical Technology (ITQ), Valencia. Basically, in this test the sample is placed in a homemade quartz reactor usually used for the assessment of gas permeation for asymmetric membranes, see details in the supporting information of [161]. Specifically, argon, nitrogen air and oxygen were fed at ambient temperature and the pressure drop ΔP across the membrane was monitored, while the inlet flow rate was varied from 50 mL/min to 400 mL/min. All streams were individually mass flow controlled. Membrane gas leak-free conditions were achieved using elastomeric rings on both sides of the membrane. The permeate was analyzed at steady state by online gas chromatography using a micro-GC Varian CP-4900 equipped with Molsieve5A, Pora-Plot-Q glass capillary, and CP-sil modules. Membrane gas leak-free conditions were ensured by continuously monitoring the nitrogen trace concentration in the permeate gas stream. The data reported here were achieved at steady state after 1 h in the reaction stream. Each GC analysis was repeated three times to minimize the analysis uncertainty. The experimental uncertainty was less than 0.5%.

Pressure drop was assessed for representative samples from all freeze-cast 3YSZ batches from Section 2.1.2 (except for FC+TL) to assess the impact of the hierarchical oriented microstructure on the gas flow resistance and compare it with the behavior of conventional and randomly organized porosity of sample PS42.

2.4. Microstructural characterization

2.4.1. X-Ray diffractometry (XRD)

X-ray diffraction (XRD) is a non-destructive technique used for determining the atomic and molecular structure of a crystal. Samples for XRD are usually in the form of powder but also can be pressed or sintered pellets, and only a few milligrams are needed. The great advantage of the technique is that a vacuum is not required and that the X-rays can travel through a container before and after interacting with the specimen. As the basic principle of XRD, the crystalline atoms cause a beam of incident X-rays to diffract into many specific directions. By measuring the angles and intensities of these diffracted beams, the density of electrons within the crystal can be obtained, from which, some parameters in the crystal can be determined, such as the mean positions of the atoms, their chemical bonds, their disorder, and various other information [54,162].

Bragg invented X-ray crystallography and received Nobel Prize for this specific contribution. The basic principle of XRD is the Bragg's law, as illustrated in Figure 2.6: when a monochromatic X-ray beam with wavelength λ is incident on paralleled lattice planes with spacing d and the incident angle θ, diffraction only happens if the path length difference between X-rays reflected by parallel planes is a multiple of the wavelength, as the following equation [162]:

$$2d\sin\theta = n\lambda \tag{2.11}$$

This expression gives the permitted angles of reflection, θ, in terms of wavelength λ and the spacing of the reflecting planes, d.

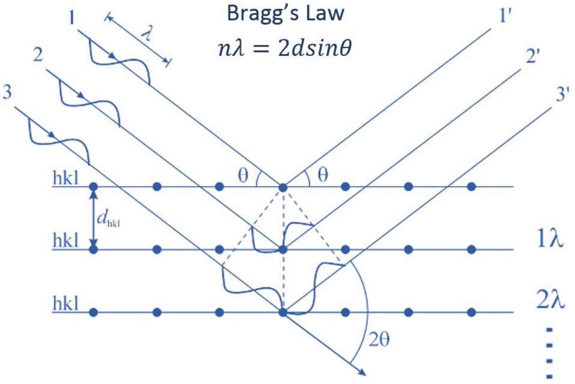

Figure 2.6 Bragg's law [163].

The LSCF ($La_{0.6}Sr_{0.4}Co_{0.2}Fe_{0.8}O_{3-\delta}$) perovskites have a rhombohedral symmetry at low temperature that transforms to a cubic symmetry at higher temperatures, same as reported for LSCF with similar stoichiometry [99,100,105]. Along with this transition the mechanical parameters increase significantly [45,100]. The phase transition of LSCF has attracted much attention but the transition temperature has not been fully specified. In the present work, room temperature (RT) and high temperature (HT) XRD experiments were carried out to establish the transition process in more details.

High-temperature X-ray diffraction (HT-XRD) was used for lattice structure, phase stability and lattice parameters analysis. The diffractometer (D5000, Siemens) was equipped with secondary mono-chromator, a NaI scintillation counter and a Bühler HDK-S1 high temperature chamber utilizing copper anode (λ = 1.5418 Å). Additional XRD investigation at room temperature (RT) of the original small rod bulk specimen and the powder produced from the rod were carried out before HT-XRD experiments with a D4 ENDEAVOUR and a D8 ADVANCE diffractometer, both with a LYNXEYE 1-dimensional detector also utilizing Cu radiation.

Data were collected with steps of 0.02°. The lattice parameters were determined via Rietveld refinement using the software TOPAS (Version 4.2, Bruker AXS GmbH, Karlsruhe Germany). Crystal structures were extracted from the Inorganic Structure Database (ICSD, FIZ Karlsruhe, Germany) [164,165]. The experimental uncertainties for lattice parameters were around ± 0.001 Å.

For X-ray powder diffraction investigation, the specimen was milled in an agate mortar. Tests were carried out in air as the LSCF specimen was sintered in air. The heating of the milled powder was performed firstly on a Pt-Rh heating tape with a lattice parameter of ~3.873 Å and secondly on a *Pt* heating tape with a 5 % higher lattice parameter of with a lattice parameter of ~3.926 Å that permitted a better resolution of the LSCF peaks.

In the initial HT-XRD experiment (VA94B02), the powder specimen was applied on a PtRh heating tape, measured at RT then every 100 K from 100°C to 800°C and back to

100°C, with heating and cooling rate 0.1 K/s. 2θ data were collected with steps of 0.02°, from 20° to 70°. Details are given in Appendices Table A.1.

The second HT-XRD experiment (VA94D02) was planned as shown in Appendices Table A.2. However, the measurement was stopped at the end of the Scan-No. 29 (2θ = ~79°) about the maximum temperature of 1000°C due to a device error, which happened again in the next trial (VA94D04) at about 950°C. Due to the automatic stop of the heating, the sample was subsequently very fast cooled down (thermal shock) to RT. The status of the quenched sample at RT was also measured (VA94D05). Analysis was based on the results of the three tests.

2.4.2. Metallographic preparation

Polished surfaces of specimens were obtained by metallographic preparation for microscopy analysis. They were embedded in epoxy resin (Buehler Epoxy 2000, solidified at room temperature under atmospheric pressure for 48 h), manually grinded with silicon carbide abrasive paper (from P#500 to P#4000) and followed by semiautomatic polishing. The polishing was carried out with a Buehler Minimet 1000, involving cloth polishing in 3 μm and 1 μm diamond suspension and a final step of 0.05 μm alumina suspension, each step for 30 min.

2.4.3. Scanning electron microscope (SEM)

SEM is a type of electron microscope that produces images of a sample by scanning the sample surface with a high-energy beam of electrons in a raster scan pattern. This electron beam generates a number of different types of signals, which are emitted from the area of the specimen where the electron beam is impinging. The induced signals contain information about the sample’s surface topography, composition and other properties such as electrical conductivity. The signals are detected and the intensity of one of the signals is amplified and used as the intensity of a pixel on the image on the computer screen. The electron beam then moves to the next position on the sample and the detected intensity gives the intensity in the second pixel and so on. SEM can achieve resolution about 1 nanometer.

The types of signals generated by the interactions between the electron beam and the specimen include secondary electrons (SE), back-scattered electrons (BSE), characteristic X-rays, Auger electrons, cathodoluminescence, as shown in Figure 2.7(a). Secondary electron detectors are standard equipment in all SEMs, but it is rare that a single machine would have detectors for all possible signals.

The beam electrons interact with the sample distribute over a three-dimensional “interaction volume”, as shown in Figure 2.7(b). The interaction volume is greater than the specimen surface under the beam. Different signals have different maximum escape depths depending on their energy differences. The escape depth of SE is approximately 5-50 nm; while BSE has an escape depth about a hundred times greater, and X-ray even greater. Greater escape depths generally lead to wider lateral dimension from which the signal can generate and thus lower potential resolution. The dimensions and shape of the interaction volume depend on accelerating voltage, atomic number and tilt. The dimensions of the interaction volume will increase with a higher accelerating voltage, and will decrease with higher atomic number elements. When the sample is tilted, the incident beam travels longer distance near the surface. Thus, relatively more SEs are generated within the escape depth than normal.

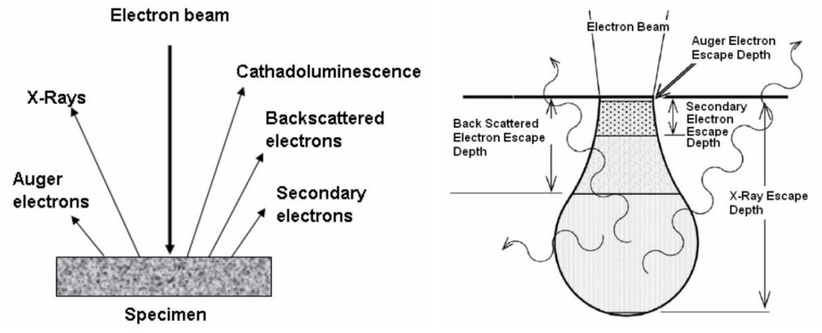

(a)Different signals (b)Interaction volume

Figure 2.7 SEM beam - specimen interactions. [166]

SEM images of polished samples surfaces were used for grain size and porosity evaluation. Grain size were recalculated into the diameter of a circle having an identical area. Hence the measured grain was given as equivalent circular diameter (ECD) in μm. Porosity was measured with image analysis method. SEM images of fractured specimens after mechanical tests were used for fractographic analysis. Fracture origins were identified using a stereoscope (Olympus SZH10) and SEM (Zeiss SUPRA 50VP). SEM was also used for phase analysis. Elemental analysis was carried out by energy-dispersive X-ray spectroscopy (EDS, Inca, Oxford).

2.4.4. Porosity measurement

Porosity measurement was carried out with commercial software AnalySIS pro (version 5.0, Olympus Soft Imaging Solutions GmbH). The wall thickness was measured by image analysis using the “local thickness” plug-in of the Fiji software [167].

The basic of Image Analysis is to set one proper threshold to the target gray-scaled image, see Figure 2.8(a), to extract objects (pores) from their background, see Figure 2.8(b), due to the high degree of contract between the object and the background.

Thresholding creates binary images, see Figure 2.8(c), from gray-scaled ones by turning all pixels below some threshold to zero (the black regions in a binary image) and all pixels above that threshold to one (the white regions). If $g(x, y)$ is a thresholded version of $f(x, y)$ at some global threshold T, it can be defined as [75]:

$$g(x,y) = \begin{cases} 1, & \text{if } f(x,y) \geq T \\ 0, & \text{otherwise} \end{cases} \tag{2.12}$$

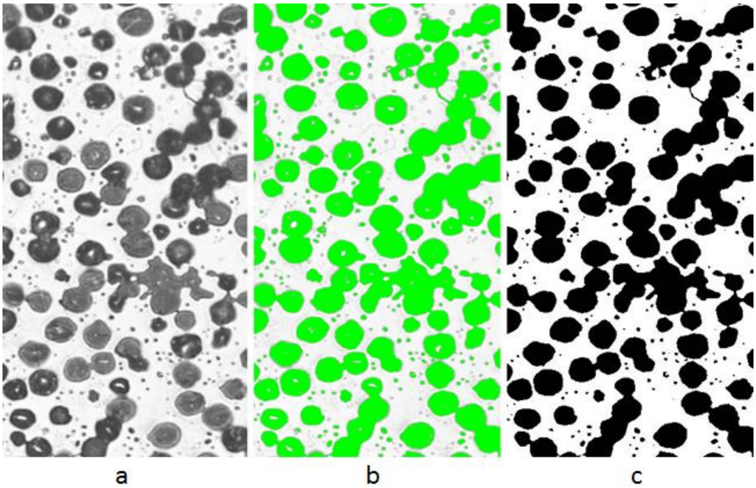

Figure 2.8 General processes of image analysis: a) Cut of original image; b) Setting threshold to select region of interested; c) Filling inner voids in struts and image binarizing.

In our case, the pore area are the black regions and the white regions are the bulk material. Porosity P can be calculated by using the sum of the black pixels divided by the total amount of pixels [75]:

$$P = \frac{A_{black}}{A_{total}} \tag{2.13}$$

Chapter 3.

Results and Discussion

3.1. $La_{0.6}Sr_{0.4}Co_{0.2}Fe_{0.8}O_{3-\delta}$ (LSCF)

3.1.1. XRD

Room temperature (RT) XRD of bulk and powder samples

To investigate the phase stability and homogeneity in bulk and powder material, an as-sintered small rod bulk specimen was investigated via XRD at room temperature, as well as powder grinded from a rod. The spectra of the bulk specimen presented in Figure 3.1(a, b) indicate a single rhombohedral phase, while the powder Figure *3.1*(c, d) showed both rhombohedral and cubic perovskite reflections (~ 60 weight %

rhombohedral and ~ 40 weight % cubic LSCF). Due to the strong overlap of the peak patterns, the dual phases could only be resolved via Rietveld refinement for peaks obtained at higher deflection angles of 135 – 140°, as shown in Figure *3.1*(d).

It appears that the as-sintered rod was only in an equilibrium state near the sample surface, since the RT-stable rhombohedra phase could only be detected with the bulk sample (the experimental acquisition depth of the XRD is less than 10 μm), while both HT-stable and RT-stable phases were discovered with the powder sample.

Interestingly the occurrence of the cubic HT-form at RT appears to be less related to the cooling speed, it rather appears to depend on the specimens' shape and grain size, since one measurement was stopped at 900°C with subsequent fast cooling down (thermal shock) to RT, and the result revealed only rhombohedral phase, see Figure *3.2*(c, d), but before the fast cooling only cubic phase was detected at 900°C Figure *3.2*(a, b).

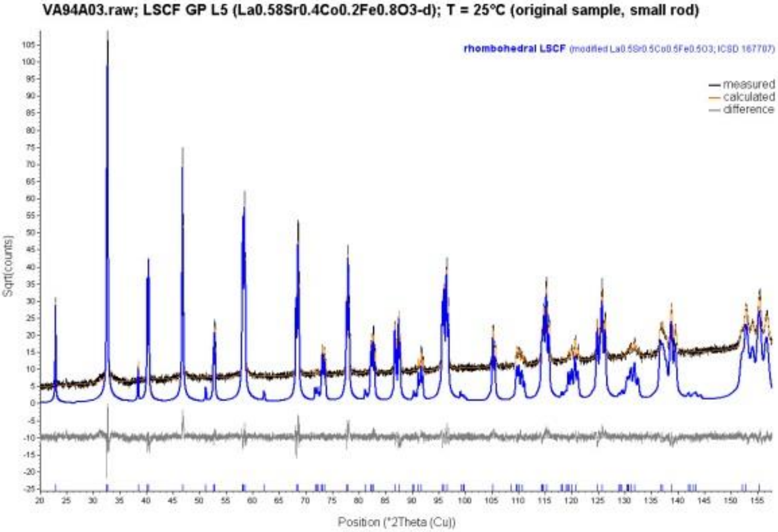

(a)

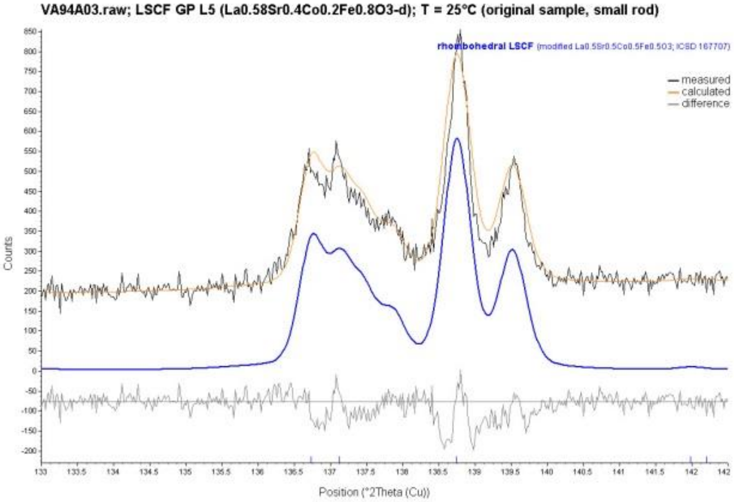
VA94A03.raw; LSCF GP L5 (La0.58Sr0.4Co0.2Fe0.8O3-d); T = 25°C (original sample, small rod)
rhombohedral LSCF (modified La0.5Sr0.5Co0.5Fe0.5O3; ICSD 167707)
measured
calculated
difference
Counts
850
800
750
700
650
600
550
500
450
400
350
300
250
200
150
100
50
0
-50
-100
-150
-200
133
133.5
134
134.5
135
135.5
136
136.5
137
137.5
138
138.5
139
139.5
140
140.5
141
141.5
142
142
Position (°2Theta (Cu))

(b)

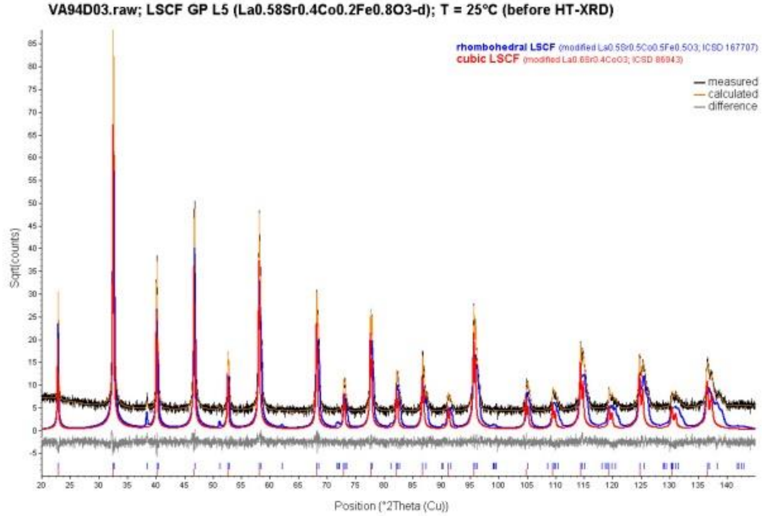
VA94D03.raw; LSCF GP L5 (La0.58Sr0.4Co0.2Fe0.8O3-d); T = 25°C (before HT-XRD)
rhombohedral LSCF (modified La0.5Sr0.5Co0.5Fe0.5O3; ICSD 167707)
cubic LSCF (modified La0.6Sr0.4CoO3; ICSD 86943)
measured
calculated
difference
Sqrt(counts)
85
80
75
70
65
60
55
50
45
40
35
30
25
20
15
10
5
0
-5
20
25
30
35
40
45
50
55
60
65
70
75
80
85
90
95
100
105
110
115
120
125
130
135
140
Position (°2Theta (Cu))

(c)

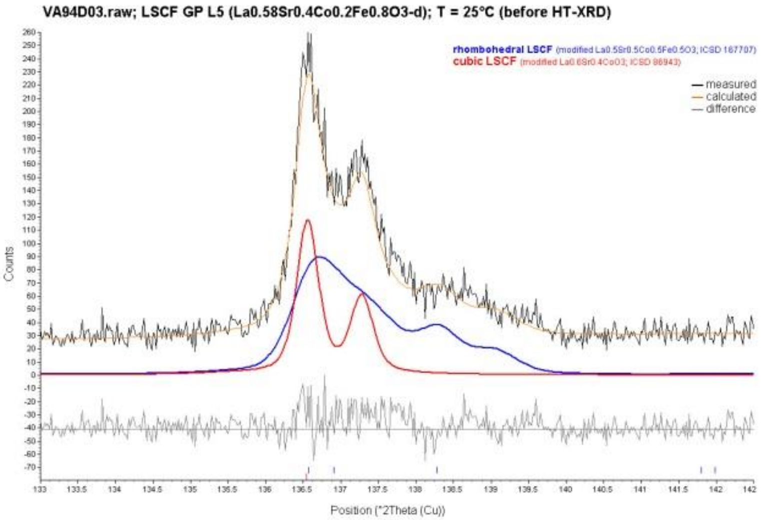

(d)

Figure 3.1 RT- XRD of bulk (a, b) and powder (c, d) LSCF samples.

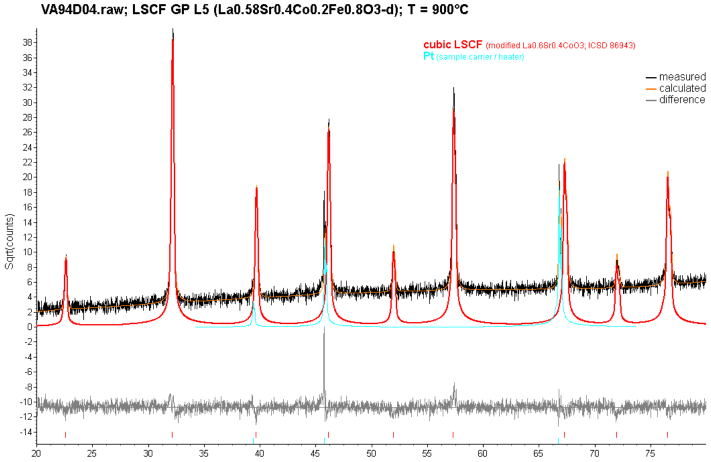

(a)

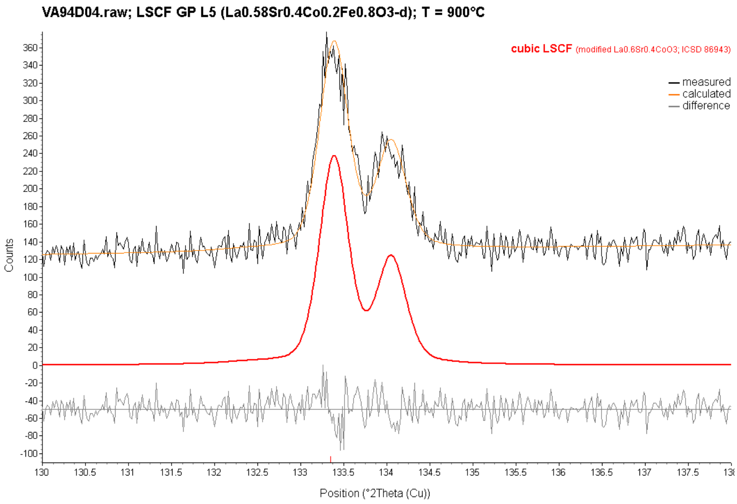
VA94D04.raw; LSCF GP L5 (La0.58Sr0.4Co0.2Fe0.8O3-d); T = 900°C
cubic LSCF (modified La0.6Sr0.4CoO3; ICSD 86943)
measured
calculated
difference
Counts
360
340
320
300
280
260
240
220
200
180
160
140
120
100
80
60
40
20
0
-20
-40
-60
-80
-100
130
130.5
131
131.5
132
132.5
133
133.5
134
134.5
135
135.5
136
136.5
137
137.5
Position (°2Theta (Cu))

(b)

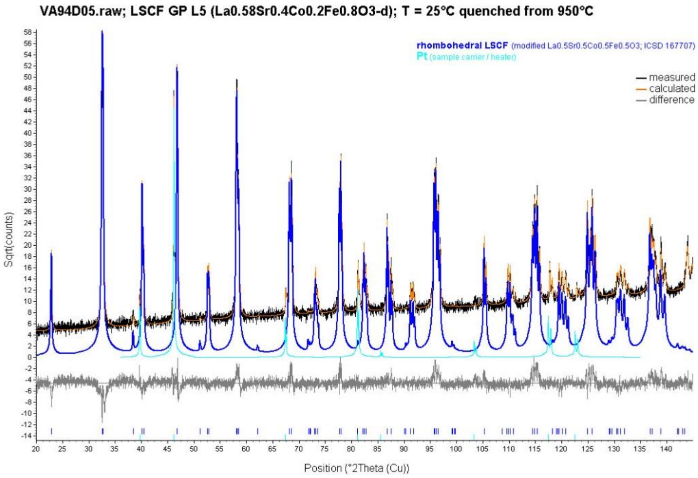
VA94D05.raw; LSCF GP L5 (La0.58Sr0.4Co0.2Fe0.8O3-d); T = 25°C quenched from 950°C
rhombohedral LSCF (modified La0.5Sr0.5Co0.5Fe0.5O3; ICSD 167707)
Pt (sample carrier / heater)
measured
calculated
difference
Sqrt(counts)
58
56
54
52
50
48
46
44
42
40
38
36
34
32
30
28
26
24
22
20
18
16
14
12
10
8
6
4
2
0
-2
-4
-6
-8
-10
-12
-14
20
25
30
35
40
45
50
55
60
65
70
75
80
85
90
95
100
105
110
115
120
125
130
135
140
Position (°2Theta (Cu))

(c)

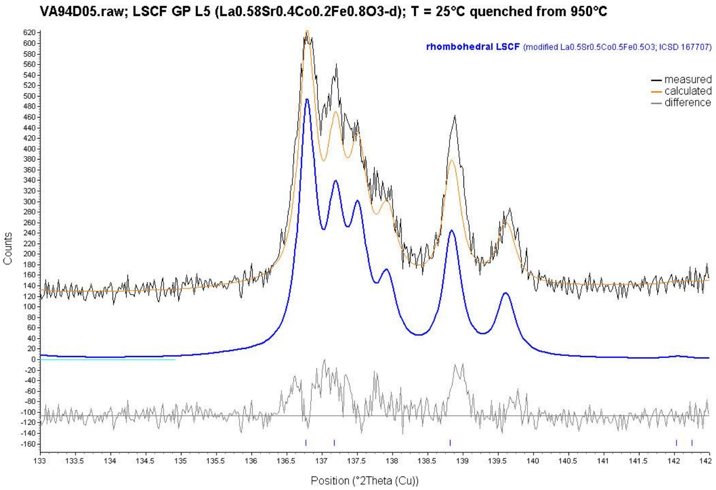

(d)

Figure 3.2 XRD spectra of before (a, b) and after (c, d) quenching.

High temperature powder XRD

In the initial HT-XRD experiment, the powder specimen was applied on a PtRh heating tape, as described in Section 2.4.1. It was detected afterwards that at RT the lattice constant of PtRh (~3.873 Å) and the pseudo-cubic LSCF are very close, hence the peaks were difficult to be resolved. In a second experiment, a Pt heating tape was used, which has a 5 % higher lattice constant (~3.926Å), which avoided the peak interference and permitted an assessment of the rhombohedral – cubic phase change.

The lattice structure used in the analysis was adjusted from $La_{0.5}Sr_{0.5}Co_{0.5}Fe_{0.5}O_3$ (a = 5.4519 Å, c = 13.2963 Å, ICSD collection code 167707 [164,165]) to the present stoichiometry of the rhombohedral structure, which can be imagined as a distorted cubic structure that is compressed or expanded in the direction of the diagonal of the cube. For visualization of the phase change, the lattice parameter of the hexagonal elemental cell was recalculated onto a pseudo-cubic elemental cell, as given below. This recalculation is a correct approximation for small distortions of the cubic lattice. The following parameters need to be defined:

- a_{rh}: a lattice parameter of the hexagonal erected, rhombohedral LSCF phase.
- c_{rh}: c lattice parameter of the hexagonal erected, rhombohedral LSCF phase.
- a_{cub}: a lattice parameter of the cubic LSCF phase. At a temperature of 25°C and 100°C it is the lattice parameter of the second phase.
- $a_{ps.cub}$: recalculated from a_{rh}, pseudo-cubic a lattice parameter $a_{ps.cub} = a_{rh}/\sqrt{2}$.
- $c_{ps.cub}$: recalculated from c_{rh} , pseudo-cubic c lattice parameter $c_{ps.cub} = c_{rh}/(2\times\sqrt{3})$.
- V_{rh}: elemental cell volume of the hexagonal erected, rhombohedra LSCF phase.
- c_{rh}/a_{rh}: axis ratio.

Although different heating tapes were used in the two HT-XRD experiments, the resulting lattice parameters, as shown in Figure 3.3(a), especially in the temperature range of 200 – 600°C, were very close. In the initial test, the peaks were too close to be resolved, which means lack of accuracy. But the second experiment gave similar results, meaning the initial results are still correct. Both HT experiments (VA94B02.raw and VA94D02.raw) indicated that during heating already at 200°C an equilibrium state is reached and only the rhombohedral material exists. Lattice parameters a and c of the rhombohedral phase become equal to the cubic phase lattice parameter between 700 and 800°C. A further possibility for visualization of the phase change is the presentation of the axis ratio c_{rh}/a_{rh}. As the lattice structure changes to cubic, this ratio becomes $\sqrt{6} \approx 2.44950$. As shown in Figure 3.3(b), the ratio reached also $\sqrt{6}$ between 700 and 800°C. Therefore, in the presentation of the lattice parameter as a function of temperature, a phase change from rhombohedral to cubic is indicated at 750°C (with 50 K to 100 K temperature steps).

In the two graphs of Figure *3.3*, a clear discontinuity in the temperature dependence of the lattice parameter can be seen during the heating phase from RT to 200°C. In this range the powder produced from the rod reveals both rhombohedral and cubic LSCF phases. It might be an artificial effect resulting from the Rietfeld analysis due to difficulties to refine both LSCF phases (only rhombohedra phase could be fitted in the case of the VA94B02 date due to the low quality of the data). The discontinuity does not occur in the cooling phase of the first HT-XRD investigation (Figure *3.3*(a) VA94B02.raw, specimen single phase in equilibrium). The single-phase lattice parameters of the initial small rod that was obtained from the XRD surface measurement at RT, could be fitted onto an extrapolation of the HT-XRD data of 200°C to 700°C. In the temperature ranges from 200°C to 650°C for the rhombohedral phase and from 700°C to 1000°C for the cubic phase, the change of the lattice parameter appears to be approximately linear.

The reliability of the temperature measurement was verified based on the phase change of $BaCO_3$ at 811°C, indicating the that temperature difference (uncertainty) was less than ± 20 K near the thermocouple. For all experiments the temperature uncertainty might be attributed to chemical strain effects that add onto the linear thermal expansion. With increasing temperature, the oxygen deficiency increases and hence the elemental cell volume also increases [168].

In the higher angle range 2θ ~ 133 – 141°, the cubic reflection (3 3 2) will split into three rhombohedral reflections, (5 1 4), (5 0 8) and (1 0 16) during phase transition. As shown in Figure 3.4, when the temperature changes from RT to 750°C, the splitting of the (3 3 2) reflection of the cubic phase is still visible up to 650°C, and is not visible anymore above 700°C, which indicates also a phase change between 650°C and 750°C. However, it cannot be ruled out that there is a temperature gradient in the investigated specimen area (± 3 mm along the heating band with respect to the position of the thermocouple).

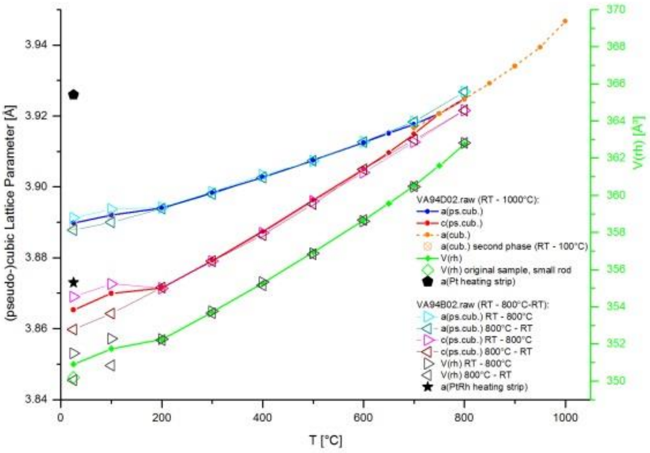

(a)

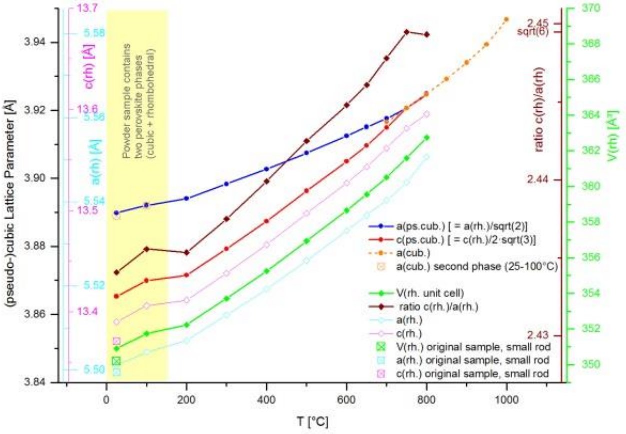

(b)

Figure 3.3 Dependence of lattice parameters on temperature.

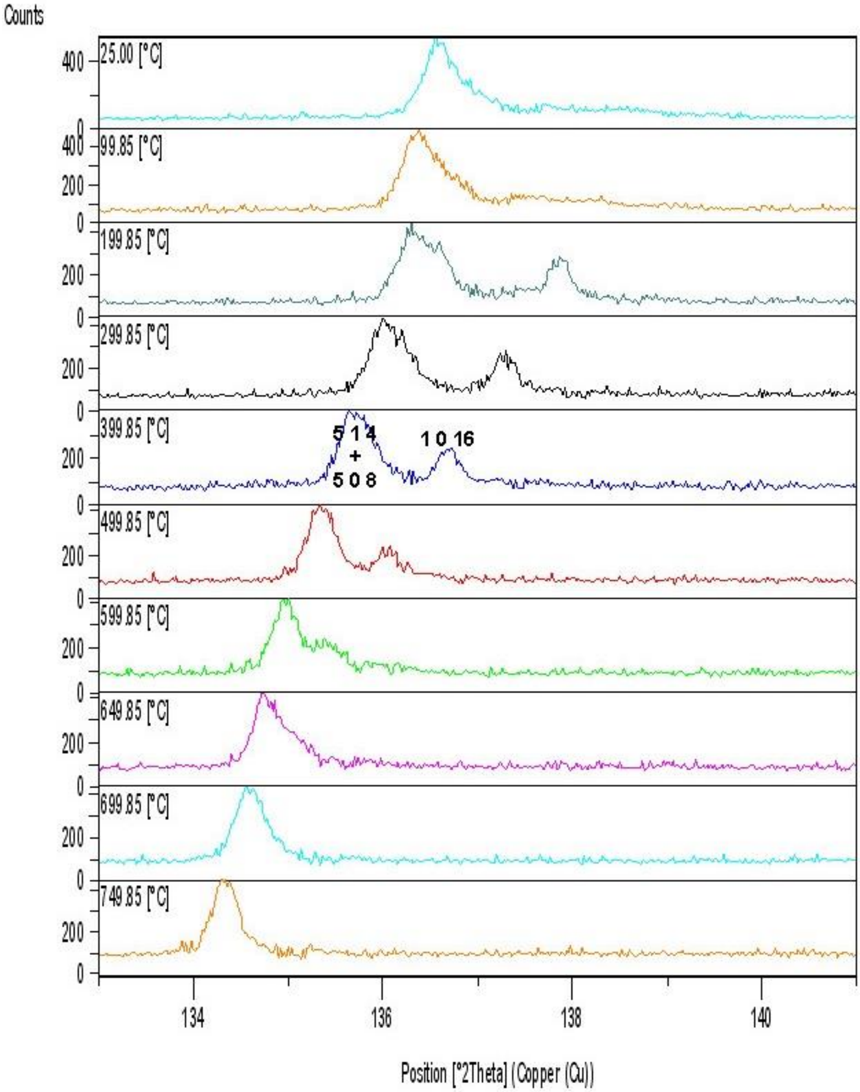

Figure 3.4 Observation of the peak splitting during phase transition in the 2θ range 133 – 141°. The $K_{\alpha 2}$ peaks are moved.

Summarizing the results of this section, high temperature XRD investigations were performed to verify the exact rhombohedral - cubic phase change temperature of LSCF. The results indicated that the phase change completes at 750 °C. Furthermore, at 650°C no reflex splitting of the cubic 3 3 2 – peak can be seen anymore (no image shown), which supports the phase change between 650 °C and 750 °C.

3.1.2. Microstructure

Details on the LSCF samples are given in Table 2.4. The specimens, which had different porosities and pore structures, were investigated via a uniaxial compression test. Porosity was measured by image analysis method based on SEM images, illustrated in Figure 3.5. The different porosities and pore structure of LSCF samples can easily be noticed from the polished microstructures, as shown in Figure 3.5. Figure 3.5(a) is the dense LSCF material from uniaxial pressing. Few pores are observable in the cross-section, corresponding to a porosity of about 5.3%. Figure 3.5 (b) and (c) are the uniaxial pressed samples with PMMA as pore former with typical spherical pores. Figure 3.5 (d) and (e) are tape-cast samples either rolled into a cylinder (TCR) or laminated into bulks (TCL) to obtain testable sample geometries. They both have starch as pore former, which results in a random pore geometry. Figure 3.5 (f), (g) and (h) are freeze-cast sample images vertical (FC30V and FC25V) and parallel (FC25P) to ice crystal growth direction, illustrating the long, aligned pores.

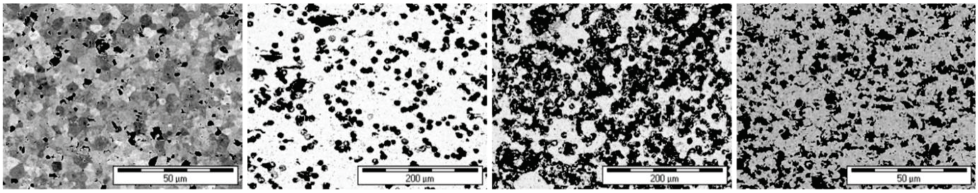

(a) Dense, 5.3% (b) PS90, 26.3% (c) PS70, 62.5% (d) TCR, 35.7%

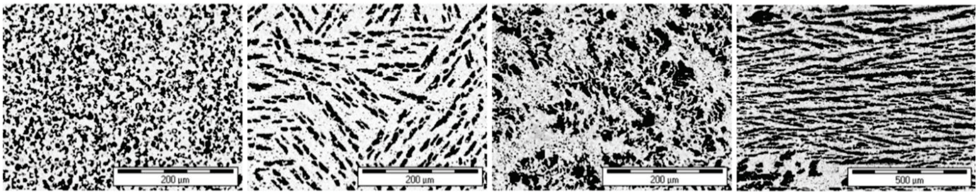

(e) TCL, 37.0% (f) FC30V, 30.4% (g) FC25V, 43.4% (h) FC25P, 43.4%

Figure 3.5 SEM images of polished surfaces of LSCF samples: (a) Dense, (b) PS90, (c) PS70, (d) TCR, (e) TCL, (f) FC30V, (g) FC25V and (h) FC25P.

More details of the freeze-cast LSCF supports are illustrated in Figure 3.6, which exhibit a very high porosity with long aligned pores. Images were taken from cross-sections both parallel (Figure 3.6a) and perpendicular (Figure 3.6b) to the freeze-cast direction. The long, oriented pores are very distinct. Image analysis revealed a rather high porosity of 43.4 % and average grain size of 2.7 μm. Ferro-elastic domains are clearly visible at higher magnification in Figure 3.6c.

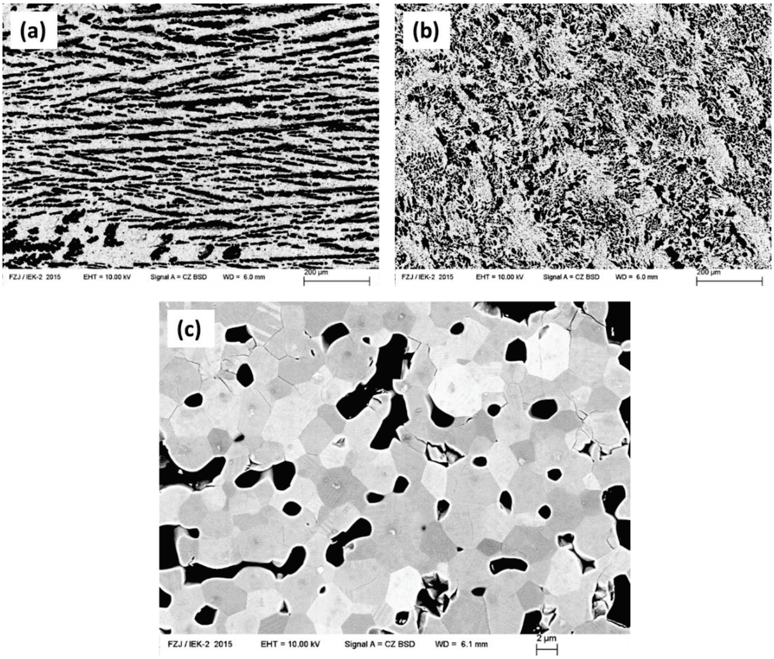

Figure 3.6 Microstructures of freeze-cast LSCF: a) parallel to freezing direction; b) perpendicular to freezing direction; c) grains with ferro-elastic domains.

The microstructural SEM investigations of LSCF-TCR samples before and after creep tests are summarized in Table 3.1. Samples were extracted parallel and perpendicular to the loading direction from the center of the specimens and in addition a load free reference piece from the edge of the rolled specimen.

Porosity of all specimens was comparable, with an average value of 35 %. The aspect ratio of the pores was given as elongation values, which is between 1.2 ~ 1.5. The elongation is a result of the anisotropy due to the orientation of the powder particle caused by the shearing while tape-cast. The measured grain size is ~ 0.6 µm, which is similar as reported for dense LSCF [102].

The specimens did not show any detectable microstructural anisotropy with respect to the loading direction or micro-cracks after creep test. Furthermore, no obvious indication of grain growth or elongation could be found, and the grains remained equiaxed after creep test. Bulk diffusion related creep mechanism could be excluded since no substantial grain deformation was observed on cross-sections. In contrast, a combination of diffusion and dislocation creep is suggested according to the stress exponent. Ferroelastic domains were clearly visible in the SEM images as already shown in Figure 3.7. The visible segregation particles on the surface were investigated with energy dispersive X-ray spectroscopy (EDX) as cobalt-rich phase.

Table 3.1 Microstructures of tape-cast LSCF before and after test.

	A. After loading	B. After loading	C. Without loading
	Cross-section perpendicular to the load axis	Cross-section parallel to the load axis	
SEM Images	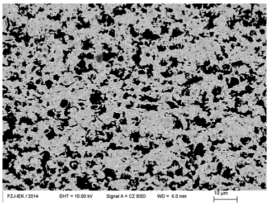	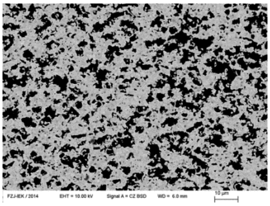	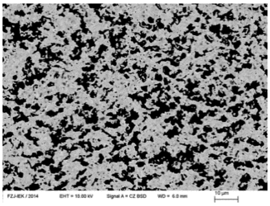
Grain size (µm)	0.60	0.58	0.63
Porosity	34.8 %	35.9 %	36.5 %
Elongation	1.5	1.2	1.5

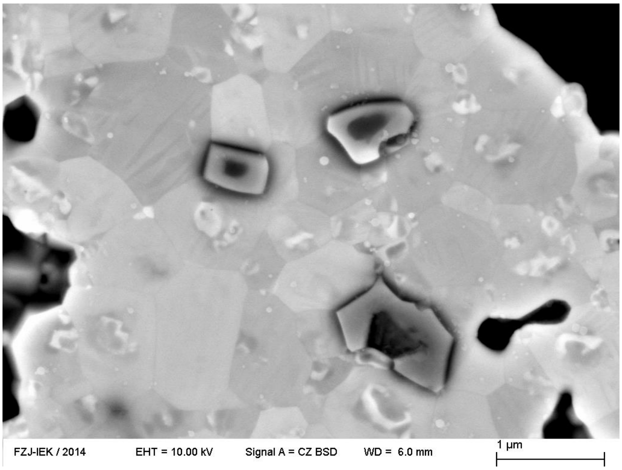

Figure 3.7 SEM image of ferro-elastic domains in LSCF grains.

3.1.3. Elastic properties of freeze-cast LSCF [1]

In this section, the elastic behavior of porous freeze-cast LSCF perovskite at room temperature was characterized by a quasi-static hysteresis compression test in order to get insight into the influence of the ferro-elasticity on the apparent elastic parameters of such anisotropic materials.

The production of the freeze-cast LSCF is given in Section 2.1.1.4. The freeze-cast LSCF supports exhibit a very high porosity with long aligned pores as visualized in Figure 3.6. The measurement procedure is explained in Section 2.2.3.1.

3.1.3.1. *Stress – strain curves*

Similar as in Section 3.1.4 for porous tape-cast LSCF, the ferro-elastic behavior of freeze-cast LSCF was investigated, however, in the current section concentrating on the stress-

---

[1] Section content published. Y. Zou et al. / Journal of the European Ceramic Society 36 (2016) 1651–1657. http://dx.doi.org/10.1016/j.jeurceramsoc.2016.01.034

strain curve. Since the material is highly porous and therefore mechanically relatively weak, a cyclic loading-unloading compression test was performed starting with a maximum load of 100 N (3.9 MPa), followed by a subsequent cycle with a maximum load of 200 N. For the following cycles, the load was increased by 200 N, and after reaching 1000 N, increased by 500 N in each cycle, which was continued until the material failed.

Longitudinal (-), transverse (+) strain and applied stress are shown in Figure 3.8 as a function of time. A crack initiated during the 8th cycle at about 1500 N (60 MPa, longitudinal strain -0.315 %) while loading to 2000 N (78 MPa). However, it was possible to continue the test after this initial crack, which appeared to arrest, since the specimen remained macroscopically intact and no visible damage was observed. In the following 9th cycle, while loading to 2500 N (98.0 MPa), the specimen gradually crushed. Therefore, even though the strain and stress evolve smoothly in Figure 3.8, the processes after the crack initiation are not discussed in the subsequent sections.

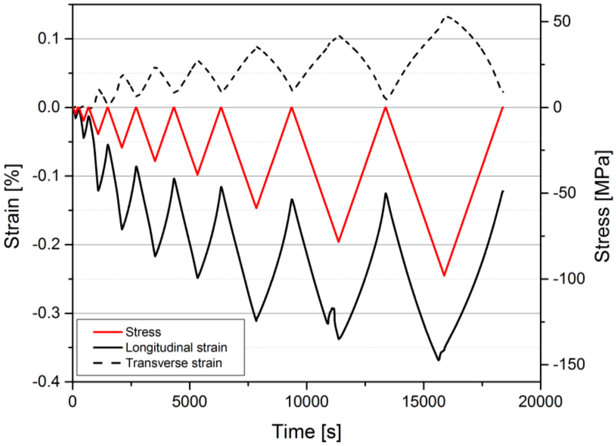

Figure 3.8 Evolution of Stress, longitudinal and transverse strain as a function of time for the load hysteresis test.

The stress-strain curves obtained from the compression test are shown in Figure 3.9 with reversed axes, each cycle termed after its maximum load in N. Compressive stress is considered as negative values, the same for longitudinal strain, while transverse strain is defined as positive. In Figure 3.9a, the stress-strain curve of each single cycle shows a distinctive non-linear behavior. The entire group of curves of all tests exhibits a hysteresis behavior, which is typical for ferro-elastic materials [98]: the stress increases almost linearly with the strain at the beginning of loading, followed by a stress plateau region due to the domain-switching process (known as "critical stress"). The stress increases again after the completion of the domain-switching process. The stress-strain curves during unloading exhibit another nonlinear behavior due to back-switching process, resulting in a hysteresis and remnant strain. The similarity of the behavior of the freeze-cast and dense LSCF with respect to the stress-strain curves and the relationship to ferro-elastic behavior indicates that the experimental results are not affected by crushing effects at lower loads.

Figure 3.9b shows the envelope curve of Figure 3.9a to emphasis the ferro-elastic behavior, and also for the use in further analysis. The stress plateau region, namely the domain-switching region, is within the strain region of -0.05 to -0.15 %, with a maximum critical stress of 22 MPa and a minimum critical stress of 6.3 MPa. The total residual strain after a stress exposure of ~60 MPa is -0.135 %, about 43 % of the maximum strain.

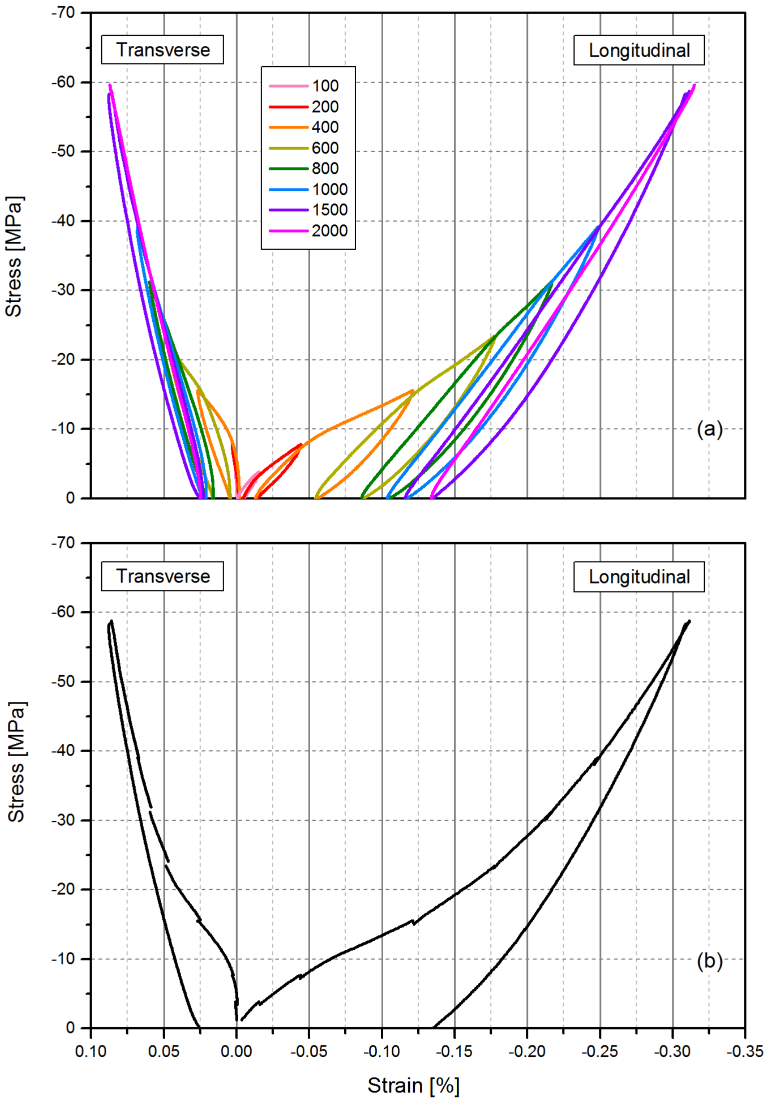

Figure 3.9 Stress - strain curves of circular compressive loading-unloading processes.

3.1.3.2. Elastic parameters

Mechanical parameters, such as Young's modulus and Poisson's ratio cannot be directly evaluated when stress-strain curves are non-linear because of the ferro-elastic domain switching. Hence, the apparent elastic characteristics were evaluated continuously from stress-strain curves with respect to loading and unloading states.

Apparent Young's, shear and bulk moduli are shown in Figure 3.10 as functions of longitudinal strain. Apparent Young's moduli were determined using Equation (2.6) as derivative of the slope of the stress-strain curve of the longitudinal part in Figure 3.9b, and apparent shear moduli were calculated using Equation (2.8) from apparent Young's moduli and apparent Poisson's ratio. Both moduli decrease from the starting of loading, and have minimum values at around -0.08 % longitudinal strain due to the progressively increasing strain related to domain switching, then increase again until the end of loading. At the beginning of unloading, both moduli exhibit even higher values than the end of loading, and continuously decrease until the end of unloading. The apparent Young's modulus has a minimum value of ~11 GPa, close to the 13 GPa given in literatures for tape-cast LSCF material [111] (bending test, porosity 46 %), while apparent shear modulus has a minimum of ~4 GPa.

The apparent bulk modulus has a relatively constant value of ~10 GPa in lower strain range (0 -- 0.10 %), and of ~20 GPa in higher strain range (-0.16 % -- 0.30 %). In the intermediate range (-0.10 % --0.16 %), also the second half of the domain switching region, a high peak is obtained, which can be considered as a transition jump between lower and higher strain range.

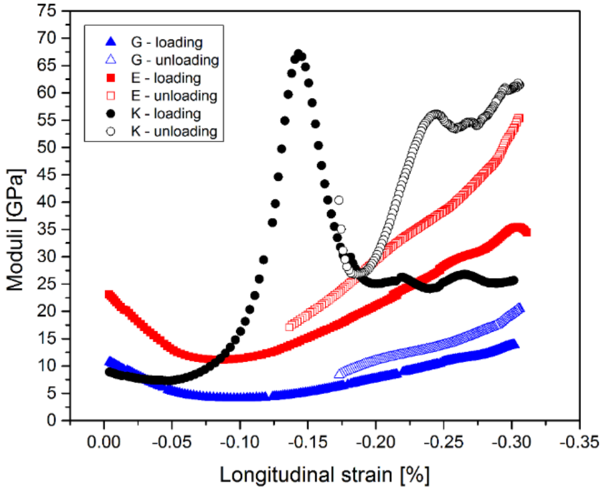

Figure 3.10 The evolution of Young's, shear and bulk modulus as a function of the longitudinal strain.

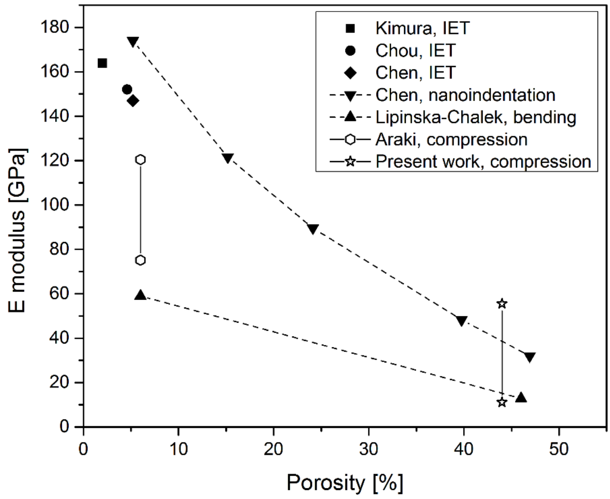

Figure 3.11 Comparison of Young's modulus with literatures.

Seven groups of Young's modulus, all measured at room temperature, are named with respect to the first author, the porosity of the material and experiment methods [98,109–113], including the present work. The seven groups of results cover the porosity range from 2 % to 47 %. Kimura et al. [110], Chou et al. [109] and Chen et al. [112,113] measured the "dense" materials (porosity 2 %, 4.6 % and 5.2 % respectively) using the impulse excitation technique (IET), which is a dynamic and macroscopic method. Chen et al. [113] and Lipinska-Chwalek et al. [111] measured the materials with various porosities using nanoindentation and ring-on-ring bending test set up respectively. These five groups give only a single modulus value. The work of Araki et al. [98] and the present work used the stress-strain curves from compression tests. Therefore, the results of these two groups are shown as a range of Young's modulus values.

It is clear that the Young's modulus decreases with increasing porosity, and the effect is more pronounced for lower porosities. The measured apparent moduli by different measurement techniques differ drastically at low porosity (below 10 %). The difference becomes trivial at higher porosity (above 40 %). For all the measurements with porosity lower than 10 %, nanoindentation method gave the highest modulus than the other methods, which may be due to: (i) the differences in chemical composition between the samples fabricated from different powders and processes; (ii) the localized measurement of indentation method which can give the modulus of the fully dense regions, whereas the other methods all measure the entire specimen volume and are affected by porosity. Three IET measurements from different publications are quite close considering the porosity differences and measurement error and are slightly lower than nanoindentation. Results from bending and compression tests are much smaller than IET and indentation method. We consider this phenomenon as the result of the ferroelastic behavior induced by the loading stresses or effects of the structural defects. The results from bending test are close to the lowest value from compressive test. The same relationship exists in samples with much higher porosity (porosity 44 % with compression and porosity 46 % with bending).

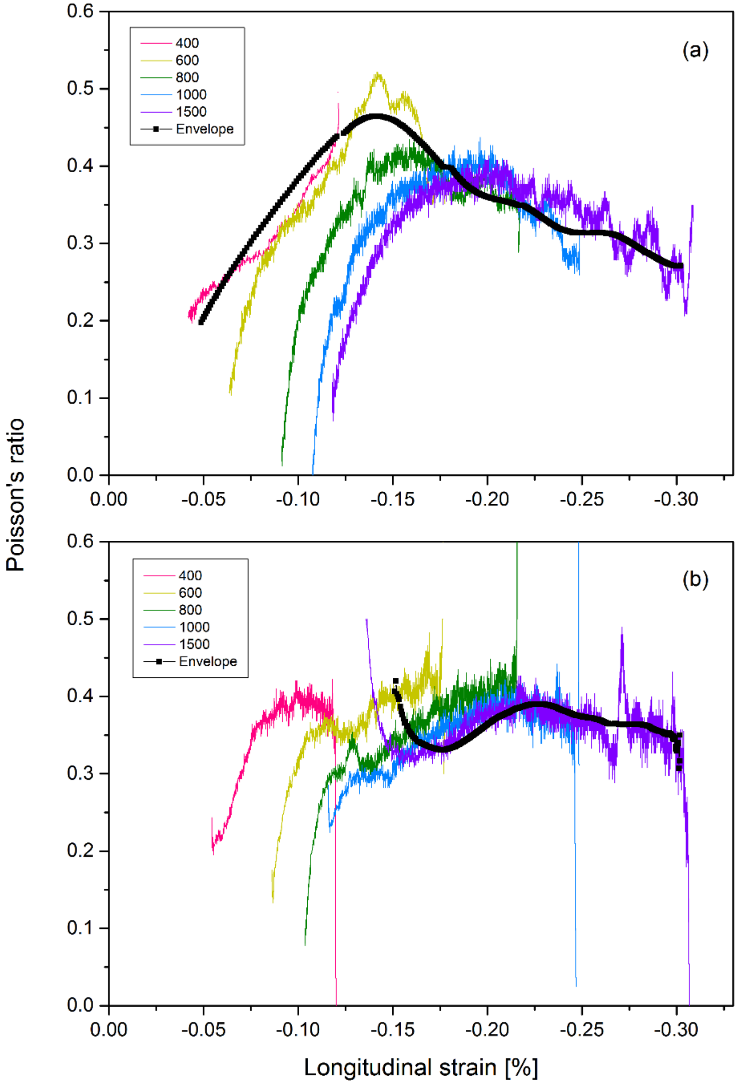

Figure 3.12 The evolution of Poisson's ratio as a function of the longitudinal strain. (a) loading; (b) unloading.

Moreover, in the work of Lipinska-Chwalek et al. and the present work, samples, with similar porosities but different pore arrangements, show similar apparent Young's moduli, which indicates that this parameter is not influenced by pore arrangement. However, the apparent crushing fracture stress (59.6 MPa) of the crack initiation during the 8th cycle is much higher than the average apparent fracture stress of the porous LSCF with isotropic pore structure of Lipinska-Chwalek's (~ 16 MPa obtained in bending test) [111]. This might be associated with benefit from the large, long, oriented pore structure, which not only provides large porosity but also relatively high mechanical stability along the pore direction compared to the homogenously distributed isotropic pore structure, but it has also to be considered that ceramics are typically stronger under compressive than under tensile stresses.

The apparent Poisson's ratios derived using Equation (2.7) from both the original stress-strain curves (Figure 3.9a) and the envelope curve (Figure 3.9b) are shown in Figure 3.12 as a function of longitudinal strain separately for loading (Figure 3.12a) and unloading (Figure 3.12b) processes. Cycles are termed according to their maximum loads in N, and the one derived from envelope curve is named as "Envelope". Since the transverse strains of cycle 1 and 2 are extremely low, even almost invisible in Figure 3.8, the Poisson's ratio was only evaluated from cycle 3 to 8, namely, starting from about -0.05 % longitudinal strain. The Poisson's ratio increases from 0.20 at the beginning of loading and reaches a maximum value of 0.5 at ~-0.14 % longitudinal strain; then decreases to a relative stable value of ~0.3. During unloading, stable values of Poisson's ratio of around 0.35 are observed between -0.20 to -0.30 % longitudinal strain, indicating that the results are not biased by crushing effects at lower loads. The averages of Poisson's ratio are 0.30 and 0.36 for loading and unloading, respectively, close to the value of 0.3 given in literature [110]. The Poisson's ratio has a maximum value since the transverse strain is not only related to a contribution of the lattice distortion but also domain switching.

In this section, elastic parameters, namely Young’s, shear and bulk moduli as well as Poisson’s ratio of freeze-cast LSCF were investigated at room temperature by a quasi-static hysteresis compression test. The evolution of these elastic parameters is studied as a function of the longitudinal strain. The elastic parameters showed extrema related to ferro-elastic domain switching. Young’s and shear moduli revealed minimum values, while bulk modulus and Poisson’s ratio demonstrated maximum values due to the transverse strain contributed by ferro-elastic domain switching.

3.1.4. Ferro-elastic behavior[2]

Porous $La_{0.6}Sr_{0.4}Co_{0.2}Fe_{0.8}O_{3-\delta}$ specimens that were prepared by tape-cast (LSCF-TCR) were tested with uniaxial compression set-up to assess if ferro-elastic creep effects that have been reported for dense material [108] also exist for porous variations. The stress – strain curves obtained at room temperature (20°C) under loads of 15 MPa and 30 MPa are shown in Figure 3.13, where stress and strain were simply calculated using the initial geometry. During loading and unloading, the stress-strain curves were visibly non-linear, which is related to an orientation-switching of ferro-elastic domains under stress [98,101,105]. The deformation behavior under constant load related to ferro-elastic domain switching has been reported for dense LSCF and termed “ferro-elastic creep” [98]. The existence of such twin-like ferro-elastic domains has been verified by SEM studies (Figure 3.7, cobalt-rich phase particles existed before the test).

---

[2] Section content published. Y. Zou et al. / Ceramics International 41 (2015) 4064 – 4069. http://dx.doi.org/10.1016/j.ceramint.2014.11.100

The displacement increases almost linearly with stress at the beginning of the loading as illustrated in Figure 3.13. The strain shows a progressive increase with applied stress above a critical stress σ_c (insert in Figure 3.13(a)), a region in which some ferro-elastic domains are switched by the applied stress. After most possible (or achievable) domains are switched, the displacement increases more linearly with the stress, whilst some remaining domains switch. In the current study, the applied stress was too small to characterize the ferro-elastic response up to saturation. At the beginning of the unloading, the displacement decreases linearly with decreasing stress due to elastic recovery and then non-linearly due to domain back-switching. After unloading, some strain recovery might be expected, however, a non-recoverable remnant strain is still observed.

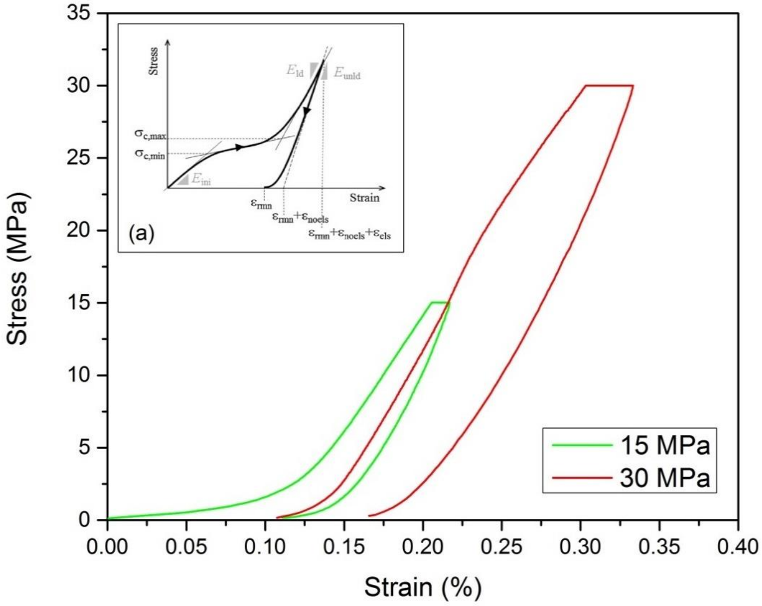

Figure 3.13 Stress–strain curves measured at 20 °C under different loads. Inset(a): typical strain–stress curve of ferroelastic material after [15].

Figure 3.14 shows the deformation as a function of time at 20 °C under constant loads of 15 MPa and 30 MPa, respectively. While keeping the stress level constant, the strain gradually increased, which again similar as reported for dense LSCF [98] an indication of the ferro-elastic creep. The data yielded a stress exponent of 2.5 which is very similar to the value obtained from the elevated temperature creep tests (see following section), although the mechanism responsible for the apparent room temperature creep is related to a different mechanism.

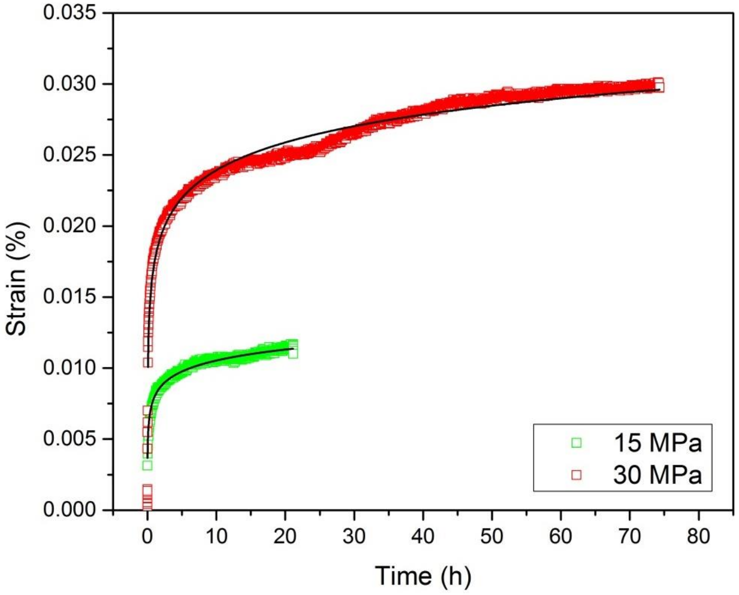

Figure 3.14 Ferro-elastic creep at 20 °C under stress of 15 MPa and 30 MPa.

3.1.5. High temperature creep

3.1.5.1. Tape-cast LSCF (LSCF-TCR) creep behavior[3]

The steady-state creep rates of the tape-cast porous LSCF measured in air in the temperature range 750°C to 950°C are compared in Figure 3.15 to the literature data of dense LSCF58 from Huang [102]. An increase of the creep rates with increasing temperature is expected for a thermally activated process. Similar as reported for dense material [102], indications for a transition to higher creep rates occurred between 750 °C and 800 °C. Note, similar creep rates were also obtained for the variant $La_{0.38}Sr_{0.6}Co_{0.2}Fe_{0.8}O_{3-\delta}$ (LSCF38) from [117] (see Figure 3.15).

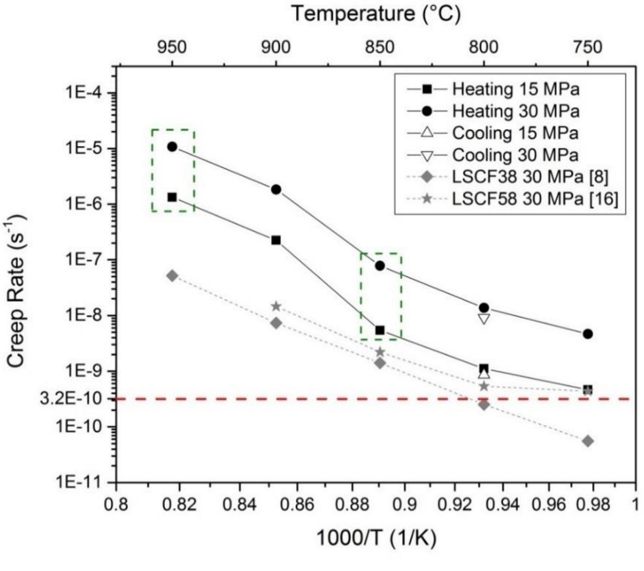

Figure 3.15 Steady-state creep rate o Steady-state creep rate of porous LSCF60 under compressive stress.

---

[3] Section content published. Y. Zou et al. / Ceramics International 41 (2015) 4064 – 4069. http://dx.doi.org/10.1016/j.ceramint.2014.11.100

The activation energy was determined from the slops of the $\ln \dot{\varepsilon} - 1/T$ plots. LSCF58 and LSCF60 exhibit a rhombohedral to cubic phase transition. The transition temperature, and along with this the increase of the Young's modulus by ~ 50 %, depends on the partial pressure of oxygen [45]. The transition temperature in air is identified to be between 700 and 800 °C [99]. Both the structural transition and the increase in Young' modulus might influence the measured creep rate, although from the experimental data an effect of the phase transition from rhombohedral to cubic phase onto the creep behavior could not be verified. Nevertheless, the apparent activation energy in the temperature range 750 to 800 °C in air was not considered. The average apparent activation energy in the temperature range 800 to 950 °C was ~ 530 ± 60 kJ/mol, which is an increase of ~ 10 % compared to dense LSCF58 which led to an average apparent activation energy of 480 kJ/mol [102].

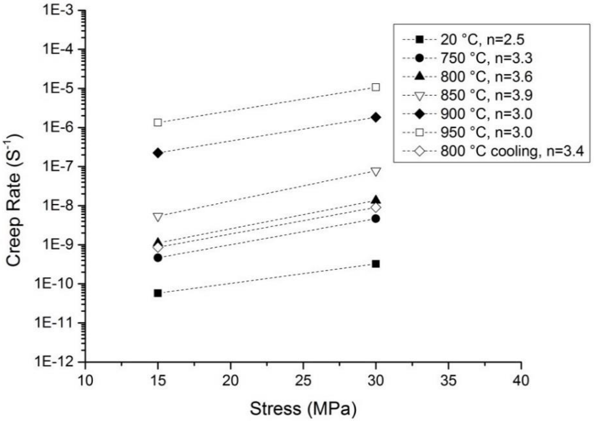

Figure 3.16 Creep rates as functions of the applied stress

The creep rates in air as functions of stress for different temperatures are shown in Figure 3.16. The stress exponent n of porous LSCF was determined from $\ln \dot{\varepsilon} - \ln \sigma$ plots. In the stress range between 15 MPa and 30 MPa the elevated temperature stress exponent *n* is between 3.0 and 3.9, which is higher than for dense LSCF58 with an *n* of 1.9 - 2.5 [102]. The stress exponent values indicate a dislocation creep mechanism at elevated temperatures.

The origin of the difference in activation energy of dense and porous material becomes more apparent when plotting the ratio of the creep rates, i.e. for 30 MPa of porous to that of the dense LSCF material in Figure 3.17. The ratio increases exponentially with increasing temperature, from about 10 to 120. A similar effect has been reported for porous and dense BSCFZ [160] (also shown in Figure 3.17), but the effect is stronger for LSCF, i.e. similar ratios are obtained for 50 K lower temperatures. Similar as suggested for BSCFZ, the observed effect might be a result of creep enhancements by surface diffusional effects.

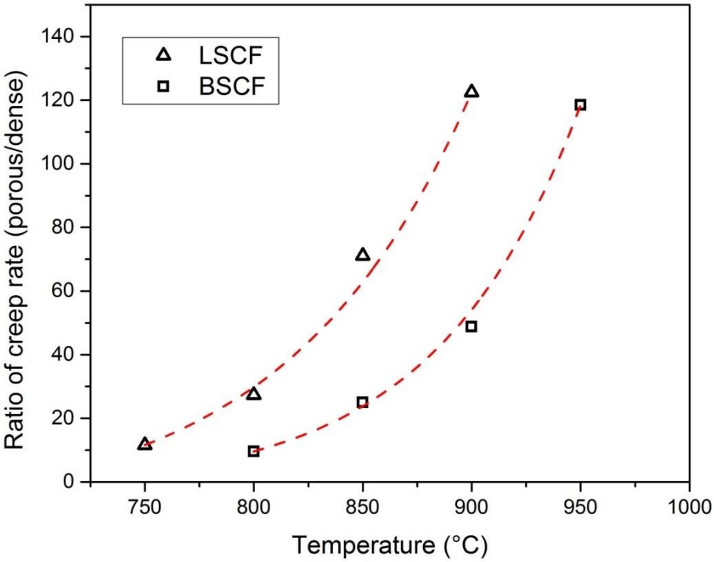

Figure 3.17 Ratio of creep rates of porous to dense material for LSCF and BSCFZ [160] for a stress of 30MPa.

In order to evaluate the long term performance of membrane structure, a maximum tolerable creep deformation of 1 % per year in a compressive mode is suggested to warrant reliable long term operation. Creep rates of porous LSCF60 are higher than those of dense LSCF58 [102] (see Figure 3.15) and all of them are higher than the acceptable rate of 3.2×10^{-10} s^{-1}. Therefore, a reduction of the application stresses or operation temperatures appears to be necessary.

The results of the microstructural SEM investigations are summarized in Table 3.1. Samples were extracted parallel and perpendicular to the loading direction from the center of the specimens and in addition a load free reference piece from the edge of the rolled specimen.

Porosity of all specimens was comparable, with an average value of 35 %. The aspect ratio of the pores was given as elongation values, which is between 1.2 ~ 1.5. The elongation is a result of the anisotropy due to the orientation of the powder particle caused by the shearing while tape-cast. The measured grain size is ~ 0.6 μm, which is similar as reported for dense LSCF [102].

The specimens did not show any detectable microstructural anisotropy with respect to the loading direction or micro-cracks after creep test. Furthermore, no obvious indication of grain growth or elongation could be found, and the grains remained equiaxed after creep test. Bulk diffusion related creep mechanism could be excluded since no substantial grain deformation was observed on cross-sections. In contrast, a combination of diffusion and dislocation creep is suggested according to the stress exponent. Ferro-elastic domains were clearly visible in the SEM images as already shown in Figure 3.7. The visible segregation particles on the surface were investigated with energy dispersive X-ray spectroscopy (EDX) as cobalt-rich phase.

3.1.5.2. *Freeze-cast LSCF creep behavior*

The freeze-cast $La_{0.6}Sr_{0.4}Co_{0.2}Fe_{0.8}O_{3-\delta}$ (LSCF) exhibited a very high porosity with long aligned pores and was designed for the use as porous membrane supports, as shown in Figure 3.6. In fact, a rather high porosity of 44 % was determined by image analysis.

High temperature creep tests were carried out for this material on two directions: 1. Loading direction parallel (P) to freeze direction; 2. Loading direction vertical (V) to freeze direction. Creep rates in the temperature range of 750°C to 1000°C with stress states of 30 MPa are shown in Figure 3.18(a) compared with creep rates of dense LSCF (porosity 3.4%) (Dense – 30 MPa) [102] and the tape-cast LSCF 36% porosity (R – 30 MPa) (Section 3.1.5.1) [31] from literature. The creep rates at 750 °C are at the limit of experimental resolution; therefore, the data do not permit a detailed interpretation. The tests along the freeze direction (P) reveal a lower creep rate than in the other direction, which can be related to the pore orientation, specifically, along the freeze direction more support walls are available to bear the load. From Figure 3.18 (a) it can be seen that the creep rates of freeze-cast LSCF in both directions are higher than the values obtained for the respective dense material, but lower than the tape-cast LSCF, which has in fact a lower porosity. Therefore, the freeze-cast LSCF appears to be more promising than the tape-cast material.

The activation energies for the temperature range 850 – 1000°C for both directions are 412 ± 40 kJ/mol (V) and 372 ± 77 kJ/mol (P), respectively. Both are lower than the data for dense LSCF (474 ± 24 kJ/mol for 850 – 950 °C) [102] and tape-cast LSCF (580 ± 60 kJ/mol, 800 – 950°C) [31]. The stress exponents at 900 - 1000°C have average values of 2.0 (V) and 1.8 (P), which indicates that the creep is dominated by a diffusional mechanism, and are similar as the stress exponent for dense LSCF reported in literature (1.9 - 2.5 in temperature range 750 - 950°C) [102].

A linear fitting was performed for the creep rates from 800 to 1000°C. Then the data determined from these mathematical descriptions were used to calculate the creep rate ratio of the porous LSCF to dense LSCF, as shown in Figure 3.18 (b). The creep rates of porous materials increased more or less progressively with increasing temperature. The creep rates ratio between freeze-cast LSCF parallel to pore direction and the dense material almost remains constant along the temperature range, while the ratio between tape-cast and dense material increased most strongly and the ratio between the freeze-cast vertical to pore direction and dense material indicates intermediate behavior. Therefore, the pore arrangement appears to have a significant influence on creep rates.

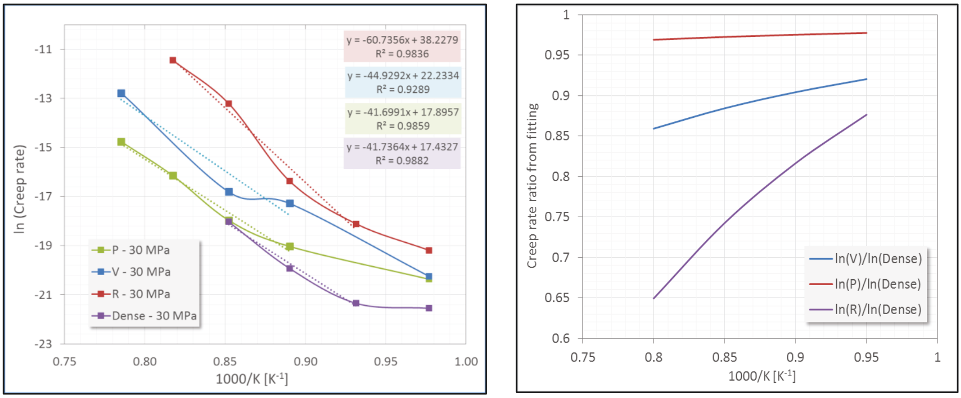

(a) (b)

Figure 3.18 (a) Creep rates of freeze-cast LSCF along two directions in comparison of creep rates of dense LSCF and tape-cast LSCF from literature; (b) Ratio of creep rates in natural logarithm.

Further elevated temperature creep tests were performed in vacuum with this material for both directions in the temperature range of 800°C to 950°C with stress states of 8, 15, and 30 MPa. Creep rates are shown in Figure 3.19. The tests along the freeze direction (P) reveals lower creep rates. Furthermore, the creep rates in vacuum are always higher than in air, as can be seen in Figure 3.20. The activation energies for the temperature range 800 – 950 °C for both directions are 440 ± 20 kJ/mol (V) and 331 ± 32 (P) kJ/mol, respectively, both being very similar as the ones for freeze-cast LSCF in air 412 ± 40 kJ/mol (V) and 372 ± 77 kJ/mol (P). The stress exponents for the temperature range 800 - 950 °C have average values of 2.0 (V) and 1.6 (P), respectively, which indicates that the creep is dominated by a diffusional mechanism. Values are similar as the stress exponent for freeze-cast LSCF measured in air (2.0 (V) and 1.8 (P) in temperature range 900 - 1000°C).

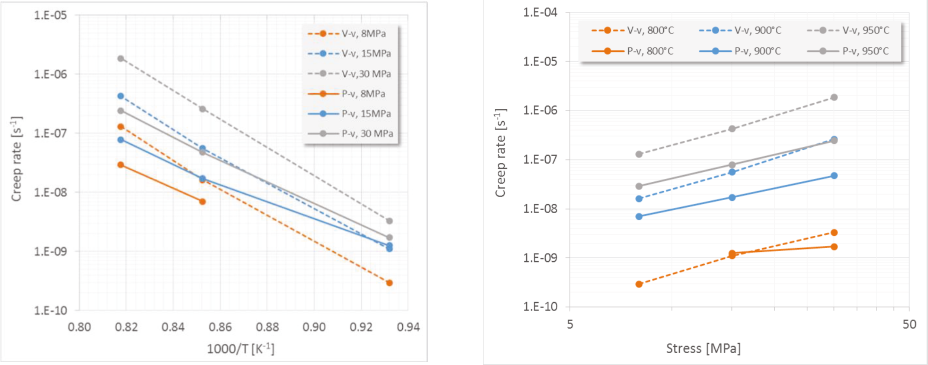

(a) (b)

Figure 3.19 Creep rates in vacuum of freeze-cast LSCF along two directions.

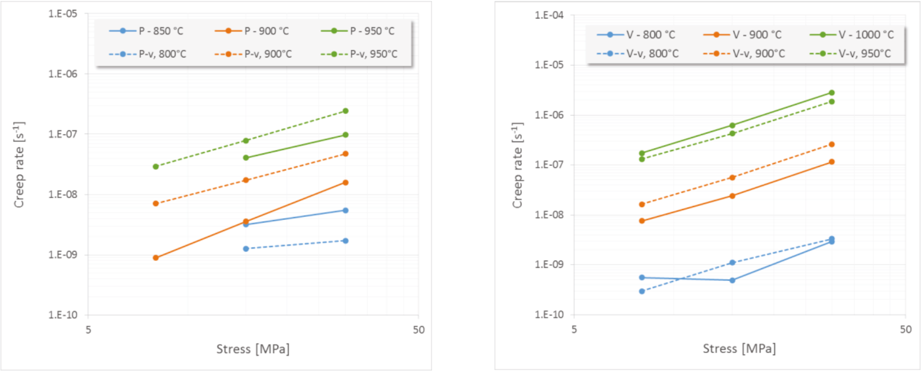

(a) (b)

Figure 3.20 Creep rates in vacuum of freeze-cast LSCF along two directions in comparison with creep rates in air.

3.1.5.3. Comparison of creep behavior of LSCF with different porosity

In Section 3.1.5.1 and 3.1.5.2, the creep behavior of porous tape-cast and freeze-cast LSCF materials was studied in detail. The influence of porosity on creep rate is remarkable and it seems that not only the overall fractional porosity but the different porous structures also affect creep rate, as illustrated in Figure 3.18. To investigate the effect of different porosity and porous structures on creep rate and how the creep rate varies from that of the dense LSCF, more porous samples by tape-casting, freeze-casting and uniaxial pressing, and a dense LSCF reference specimen obtained by uniaxial pressing, were tested and analysed in the following subsection. Details on the LSCF samples production are described in Section 2.1.1; tested samples details are given in Table 2.4 and relevant text; microstructures are illustrated in Figure 3.5. The specimens, which had different porosities and pore structures, were investigated via a uniaxial compression test as introduced in Section 2.2.3.2.

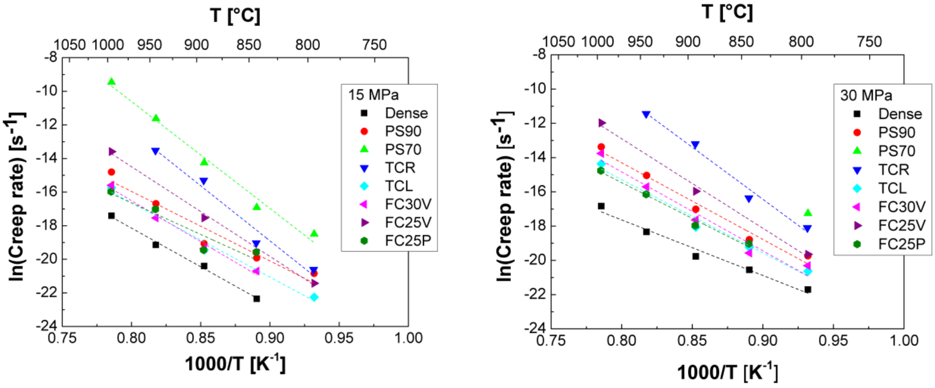

(a)

(b)

Figure 3.21 Temperature dependency of creep rates of different LSCF samples.

Elevated temperature creep tests were carried out for these materials for applied stress of 15 MPa and 30 MPa in the temperature range of 800°C to 1000°C. Creep rates in terms of their natural logarithm as a function of 1000/*T* (*T* in K) are shown in Figure 3.21.

The freeze-cast sample FC25 were tested in the loading direction both vertical (FC25V) and parallel (FC25P) to the freeze direction. All porous samples have higher creep rates than the respective dense material of similar grain size, as might be expected, and almost all the creep rates exceed the 1% creep strain per year criteria (3.2×10^{-10} s^{-1}, $\ln(3.2\times10^{-10}) \approx -21.9$), which is suggested to be critical for application. [114]

Comparing the "Dense" samples results to literature data by Huang et al. [102], under 30 MPa and 900°C, the shown creep rate (1.38×10^{-9} s^{-1}) in Figure 3.21 is about one order of magnitude lower than the data reported by Huang (1.5×10^{-8} s^{-1}) as quoted in Table 1.3. The main reason for this distinct difference could be the grain size difference between current dense material (3.1 ± 0.2 μm) and the one of Huang (0.6 ± 0.2 μm). Assuming that the creep rate difference is only induced by the grain size, with the data under 30 MPa and 900°C, the grain size exponent m can be roughly estimated with Equation (1.14) to be 1.7, same as reported for BSCF in literature [115].

Overall, LSCF samples show a clear increase in creep rates with increasing porosity. Regarding different synthesis methods, it seems that the tape-cast laminated material possesses the lowest creep rate compared to the others with similar porosity, while the specimen from uniaxial pressing leads to the highest creep rates. Reason for the difference between the different methods should be the focus of future studies. Samples with smaller grain size have higher creep rates, as expected from Equation (1.14).

According to Equation (2.10), the activation energy E_a can be calculated from the slope of *ln(*creep rates*)* - 1000/*T* (*T* in K) plots, as in Figure 3.21, and the stress exponent *n* from the plots of *ln*(creep data) – *ln*(stress) (plots given in Appendices A.2). Both parameters are summarized in Table 3.2. The stress exponent *n* ranges from 1.4 to 3.4 and the activation energy from 297 to 530 kJ/mol, similar as reported by Huang et al. (the stress exponent in the range 1.9 to 2.5 for all temperatures, activation energy ~ 250 kJ/mol in the temperature range 700 to 800 °C) [102]. The samples with smaller grain size tend to have a higher n and E_a values. The TCR sample has the highest n and E_a values, which might be an artefact related to the rolled cylinder geometry.

Table 3.2 Creep exponents and activation energies.

	Dense	**PS90**	**PS70**	**TCR**	**TCL**	**FC30V**	**FC25V**	**FC25P**
Porosity *P* [%]	5.3 ± 0.3	26.3 ± 1.7	62.5 ± 7.0	35.7 ± 1.3	37.0 ± 1.6	30.4 ± 1.4	43.4 ± 3.0	
Grain size *d* [μm]	3.1 ± 0.2	1.8 ± 0.6	1.9 ± 0.1	0.6 ± 0.06	3.3 ± 0.1	3.0 ± 0.2	3.1 ± 0.5	
n	1.4	2.1	1.8	3.4	1.8	2.4	2.1	1.5
E_a [kJ/mol]	321	358	479	530	346	433	356	297

In general, the creep rate is determined by the species of the lowest diffusivity and in LSCF, it has been reported to be related to the diffusion of A-site cations [102]. Besides, different publications studying the porosity effect on steady-state creep have concluded that the stress exponent of the porous body should be identical to that of the dense materials [92,93]. Therefore, it appears to be reasonable to assume that for LSCF samples with the same lattice structure should have the identical stress exponent (identical creep mechanism) and identical creep activation energy (identical diffusion species and diffusion paths).

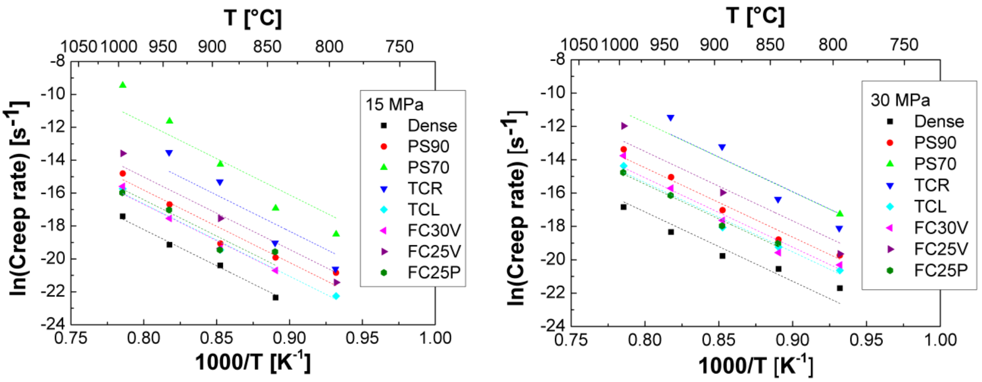

(a) (b)

Figure 3.22 Single slope fitting of the creep rate data under 15 and 30 MPa for activation energy calculation.

Considering the reasonable assumptions outlined above, then all the creep results in Figure 3.21 should have the same slope (same activation energy). Considering the large uncertainty of creep results due to the small deformation measurements, the slopes of the fitting lines in Figure 3.21 are possible to be the deviations from one single value. Therefore, a single slope fitting was applied separately to the creep data under 15 and 30 MPa, as shown in Figure 3.22. The resulting best fitting slope and corresponding activation energy values are given in Figure 3.23**Fehler! Ungültiger Eigenverweis auf Textmarke.**. Activation energy values for 15 and 30 MPa agree very well to each other, as expected. A similar single slope fit was also applied to the plots of *ln*(creep data) – *ln*(stress) for stress exponent calculation, to obtain a best fitting stress exponent value of 1.7, as illustrated in Figure 3.23.

Table 3.3 Best fitting slope values for single slope fitting and corresponding activation energy.

	$E_a/1000R$	E_a
	[K]	[kJ/mol]
15 MPa	44.022	365.9
30 MPa	41.628	346.1

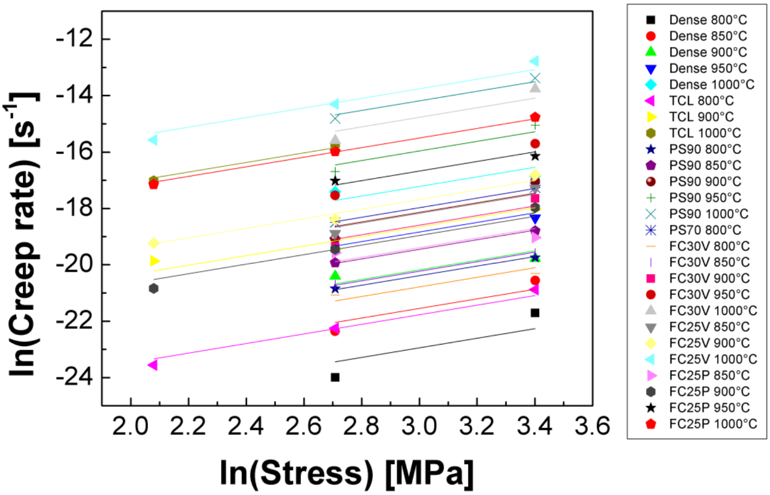

Figure 3.23 Single slope fitting of the creep rate data for stress exponent calculation.

With the activation energy in Table 3.3 and the stress exponent n = 1.7 (best fitting value from Figure 3.23), the values of $\ln A$ term were then calculated for each single fitting lines. In Figure 3.24, the $\ln A$ values are plotted as a function of porosity. The dashed lines are linear fitting of $\ln A$ values from the group of samples produced by the same production method and the dense LSCF is considered as the base point of all sample groups.

$$\ln \dot{\varepsilon} = n \ln \sigma - \frac{E_a}{RT} + \ln A \tag{3.1}$$

$$\dot{\varepsilon} = A' \sigma^n exp\left(-\frac{E_a}{RT} + bP\right) \tag{3.2}$$

Considering the linearity of the $\ln A$ on porosity to be proven by the results, then Equation (2.10) can be transformed into Equation (3.2), with an extra e^{bP} term related to porosity P. The parameter b is corresponding to the different porous structure.

In fact, the exponential term e^{bP} has been discussed intensively by R.W. Rice based on the **Minimum Solid Area** (MSA) concept [78,79]. As shown in Figure 1.13, based on different literature models, for low porosities, the minimum solid area (and hence the property value of interest) approximately linear decreases on a semi-log plot versus P. Beyond a critical porosity P_c, the property of interest starts decreasing more rapidly, then nearly precipitously, going to zero. The creep rate, on the contrary, increases with increasing porosity. But the exponential term e^{bP} seems to be still useful with a positive b value, while in work of Rice, b is negative for elastic modulus and fracture strength.

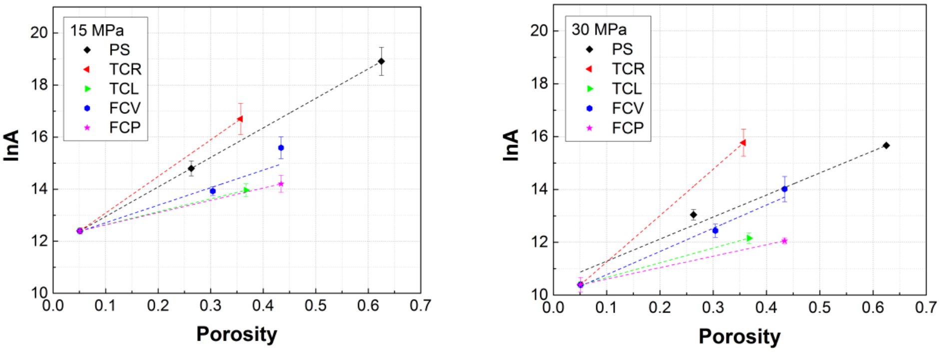

(a) (b)

Figure 3.24 Evolution of calculated $\ln A$ values over porosity.

As for a diffusion creep mechanism, the creep rate also depends on grain size, as described in Equation (1.14). In Figure 3.25, the $\ln A$ values were calculated with creep rates normalized to a grain size of 1 µm. An inverse grain size exponent $m = 1.7$ was used in the calculations, which was calculated above using the "Dense" sample and results of Huang et al. [102]. Compared to Figure 3.24, the normalized values in Figure 3.25 vary much less for the different porous structures. It also proofs that under the tested conditions, the creep behavior of the material is pre-dominantly determined by diffusion. A similar phenomenon has been reported for BSCF and BSCFZ in literature [118].

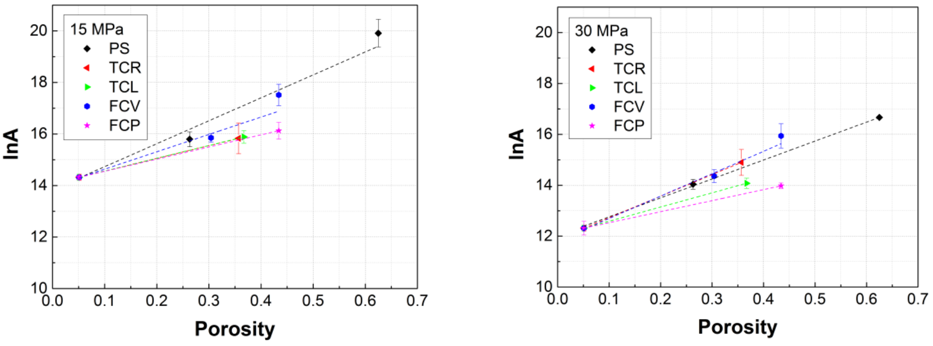

(a) (b)

Figure 3.25 Evolution of calculated ln *A* values over porosity with normalization to grain size *d* = 1 µm.

In this section, creep behavior of LSCF specimens prepared with uniaxial pressing, tape-cast, and freeze-cast were investigated via uniaxial compression testing with respect to high temperature creep behaviour. All porous samples have higher creep rates than the dense material, as might be expected, and all of the creep rates exceed the 1 % creep strain per year criteria (3.2×10^{-10} s^{-1}), which is considered to be critical for application. Overall, LSCF samples show a clear increase in creep rates with increasing porosity, but different porous structures seem to result in different creep rates. Furthermore, samples with smaller grain size have higher creep rates. After normalization to grain size 1 µm, the difference in creep rate become smaller, which indicates that also the grain size has a more pronounced influence on creep rates.

3.1.6. Creep rupture

Sandwich samples of BSCF and LSCF with porous matrix and dense layers on both side (as illustrated in Figure 3.27a) were tested with three-point bending set-up with respect to the creep rupture behavior of the dense layer.

In fact, after testing, micro-cracks along the grain boundaries were observed on the tensile side surface of BSCF dense layer after creep test at 875 °C for two hours that can be associated with creep rupture of the dense layer, as shown in Figure 3.26. Similar creep damage features have been reported for dense BSCF bulk materials in literature [169]. But no obvious cracks could be found on the tensile side of the LSCF sample, even though the sample had a much larger apparent deformation than the BSCF sample (see central displacement in Table 2.3).

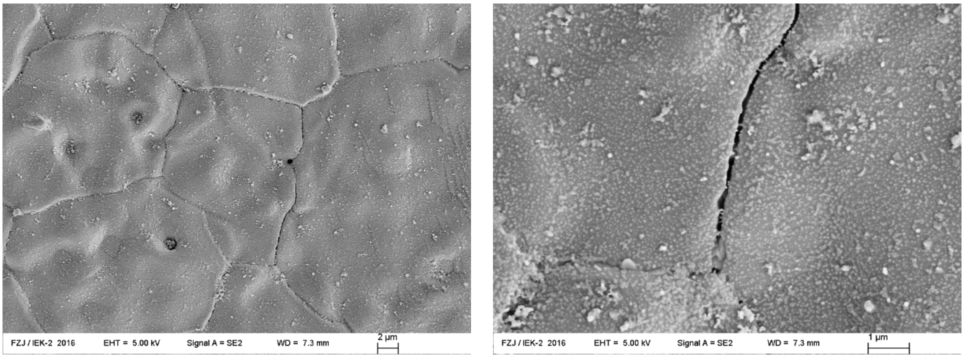

(a) (b)

Figure 3.26 Intergranular crack on the tensile side of BSCF dense layer after a creep test at 875 °C for two hours.

But interestingly, a remarkable surface difference was observed for LSCF samples between as-received and tested samples, and between the tensile side and the compressive side of the tested sample. Figure 3.27(b) presents the dense layer surface of as-received sample. The material is quite dense but pores / pin holes are observable. Figure 3.27(c) is the dense layer surface of tensile side after creep test at 955 °C for about one hour. Secondary phases were observed on the sample surface, large amount of small crystals inside of grain boundaries and also large crystals grown out of grain boundary. There are two kinds of secondary phases from the EDX results: the darkest phase is $CoFeCrO_x$ and the less dark phase is $SrCrO_x$. And these two kinds of crystallites exist almost always as couple. Besides, the matrix grain surface become much rougher than in case of the as-received samples due to an apparent thermal etching effect, and no pores / pin holes observable anymore. Figure 3.27(d) corresponds to the dense layer surface of compressive side after creep test. Only a few secondary phase crystallites exist on the surface and only $SrCrO_x$ phases could be detected. Pores / pin holes were still observable and matrix grain surface roughness is similar as that of the as-received sample. Besides, Cr was only detected on the secondary phase particles but neither in the matrix LSCF nor the as-received materials. It proved that the Cr was not in the original material but coming from the test environment.

It can be speculated that during the bending test at high temperatures, reacting with Cr impurities (may be induced from tooling processes or the testing environment), LSCF degraded into $SrCrO_x$ and $CoFeCrO_x$ phases.

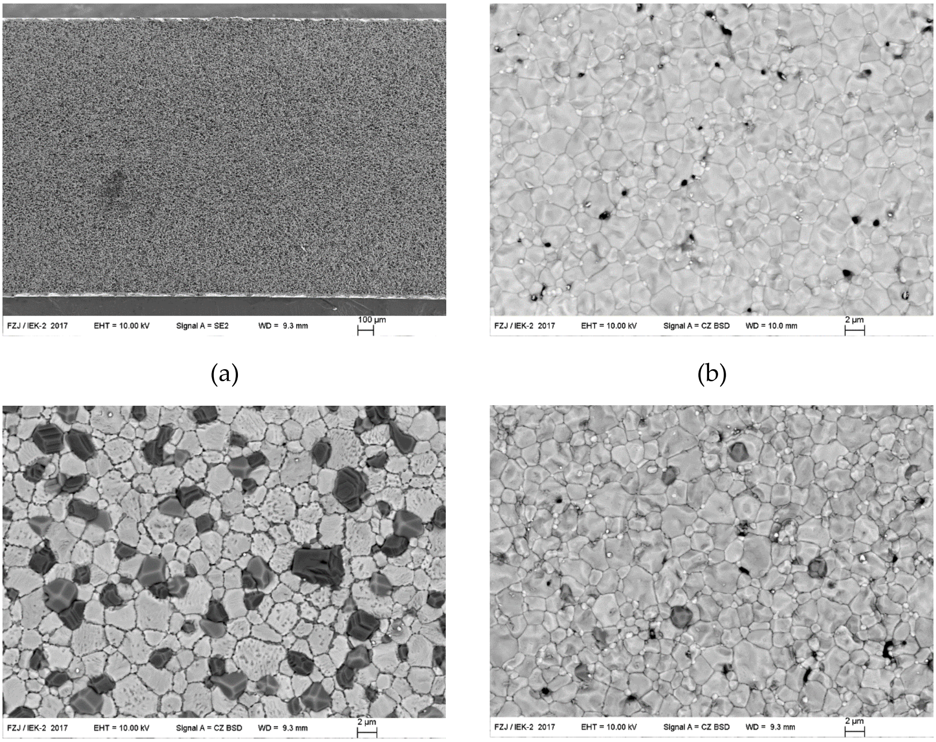

(a) (b)

(c) (d)

Figure 3.27 SEM images of LSCF sandwich sample: (a) cross-section with all three layers; (b) dense layer surface of as-received sample; (c) dense layer surface of tensile side after creep test at 955 °C with $CoFeCrO_x$ (darkest) and $SrCrO_x$ (less dark) particles; (d) dense layer surface of compressive side after creep test with a few $SrCrO_x$ particles.

Sr surface segregation and Cr deposition and poisoning of LSCF have been the focus of a large number of studies regarding SOFC application. Jiang and Chen presented a detailed review on the studies of Cr deposition and poisoning of SOFC cathodes [170]. A lot of studies suggested that SrO species are originally enriched or segregated at the surface of LSCF, which can be the result of decreased stability at the surface and structural distortion due to the abrupt termination of the lattice structure [171]. Majkic et al. outlined on the basis of experiments using creep quenched samples that Sr segregation in La–Sr–Fe–Cr–O is a stress induced phenomenon [172]. Araki et al. studied the Sr segregation for annealed LSCF with and without compression and concluded that compressive stress resulted in larger but fewer segregation particles [99], however, no Cr in the segregated particles was reported suggesting that the used experimental set-up did not contain Cr-containing metals, contrary to the set-up used in the current work.

The reaction of gaseous Cr species and surface segregated SrO would lead to the formation of Sr-Cr-O nuclei on the surface of LSCF and subsequent crystallization and grain growth of SrCrO4 and /or Cr_2O_3 solid phases [170]. Recent study of the surface segregation and Cr deposition on dense LSCF bar samples showed that both cobalt and strontium are segregated out of the LSCF lattice, forming individual SrO and CoOx particles [170]. But no Cr detected on the segregated CoOx. The authors suggested that the Cr deposition on LSCF preferentially takes place on segregated SrO rather than on Co_3O_4 [170].

However, in the present study, both $SrCrO_x$ and $CoFeCrO_x$ particles were detected on the tensile side of the bending samples but only $SrCrO_x$ particles on the compressive side where in general much less secondary phase particles were observed. Therefore, in agreement with literature [170], Cr deposition on LSCF preferentially takes place on segregated SrO rather than on CoO_x. But when the condition is more befitting for Cr deposition, i.e. under tensile stress in this case, both processes can be observed.

To verify the origin source of the Cr element and the influence of the stress status on the surface degradation of LSCF, further two tests were performed without the thermal couple in the heating zone with different loads (see Table 2.3 sample LSCF-4 and LSCF-5). Both tests were performed with three-point bending set-up at 950 °C for 90 hours.

LSCF-4 sample was loaded at 8 N, while in the case of LSCF-5, no load was applied. After the tests, SEM investigations were carried out to characterize creep rupture and surface degradation effects.

No crack/delamination was observed for both samples. But secondary phases were found for both samples on both dense and porous layers. EDX results showed that the secondary phase was FeCoOx. There was no trace of Cr in the samples with all EDX results. Compared to the previous test, the thermal couple was removed from the heating zone, which was speculated to be the Cr source. Therefore, these results proofed that the Cr observed in the initial test that was reported previously came from the testing environment, namely, the thermal couple in the furnace; it was not in the original as-received sample.

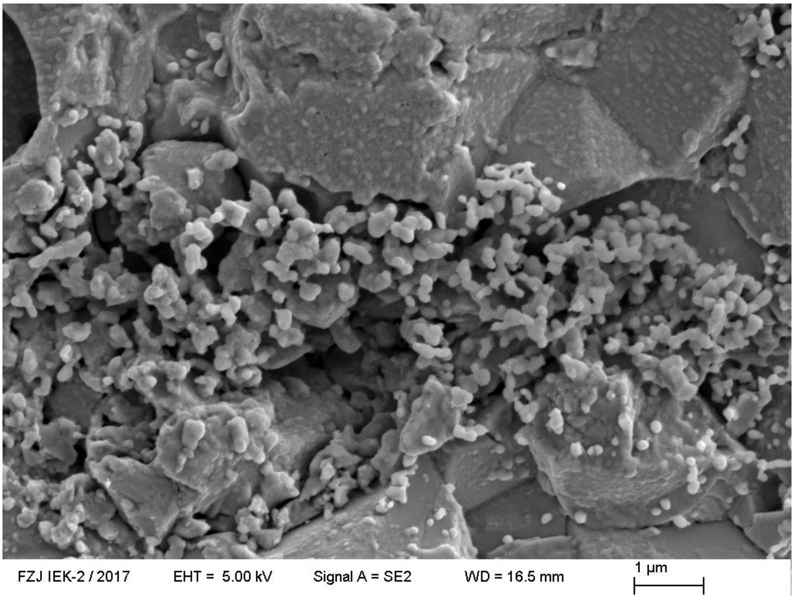

(a) LSCF-4 secondary phase on porous layer grains

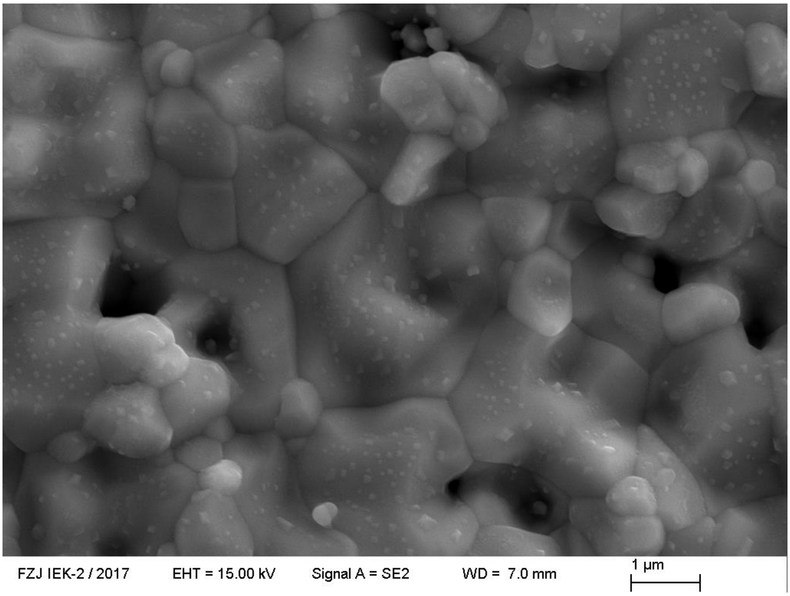

(b) LSCF-4 tensile side: very small secondary phase particles on grain surfaces

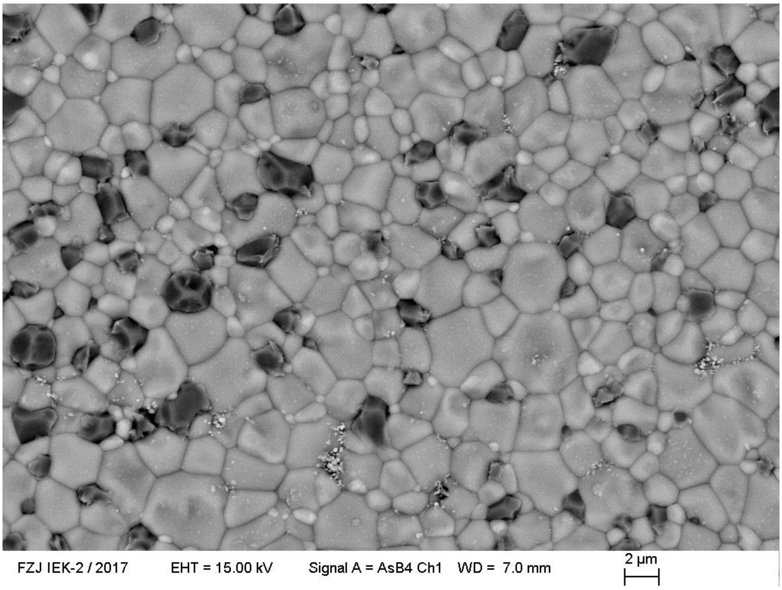

(c) LSCF-4 compressive side: large secondary phase particles, $FeCoO_x$.

Figure 3.28 SEM images of LSCF-4 samples after three-point-bending test.

Figure 3.28 presents a SEM images of the sample LSCF-4 after the three-point-bending test at 950°C for 90 hours. Secondary phases, FeCoOx, were found on both dense and porous layers. In Figure 3.28a, the secondary phase particles have already segregated as clusters on the grain surface. On the tensile side (Figure 3.28b), only very small secondary phase particles were found on grain surfaces. On the compressive side (Figure 3.28c), large secondary phase particles were observed.

Figure 3.29 shows the SEM images of LSCF-5 sample after annealing at 950°C for 90 hours. Secondary phases, FeCoOx, were found on both dense and porous layers. On the upper side (compressive side in the three-point-bending setup, Figure 3.29a), secondary phase particles were found. On the bottom side (tensile side in the three-point-bending setup, Figure 3.29b), almost no secondary phase particles were observed, while pin holes can be seen on the sample surface.

SEM investigations were also performed for an as-received sample and results are shown in Figure 3.30. Secondary phases, $FeCoO_x$, were found on one side (Figure 3.30b), similar as in Figure 3.29a. On the other side (Figure 3.30a), no phase particles were observed, while pin holes can be seen on the sample surface, similar as in Figure 3.29b.

No surface crack and no lay delamination were found for all sandwich samples. Therefore, creep rupture seems not to be a problem to LSCF at the considered temperature, although some relaxation effects due to the remnant porosity of the membrane layer cannot be ruled out. Secondary phase particles, FeCoOx, existed already on one side of as-received samples that were maybe generated during the sintering process when the respective surface was in contact with the sintering plates. Cr species observed in the initial test were introduced from the thermal couple in the furnace. When thermal couple was removed in the subsequent tests from the heating zone, no Cr observed on the samples anymore.

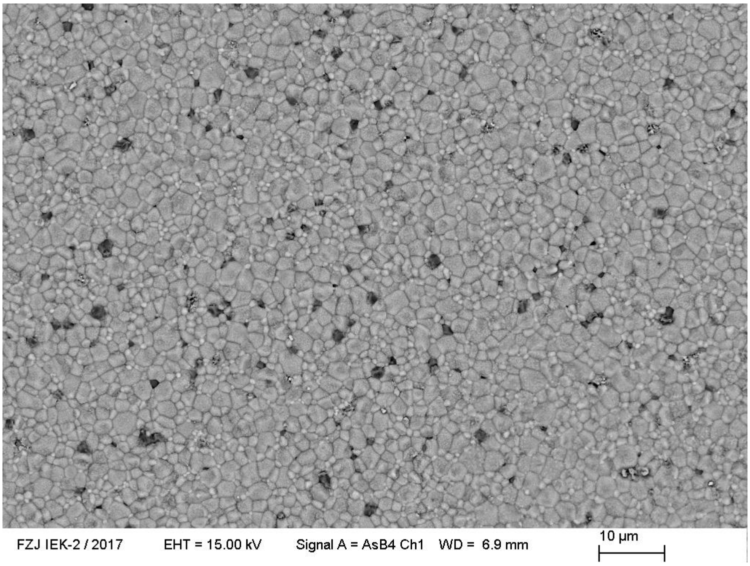

(a) LSCF-5, upper side: secondary phase particles, $FeCoO_x$.

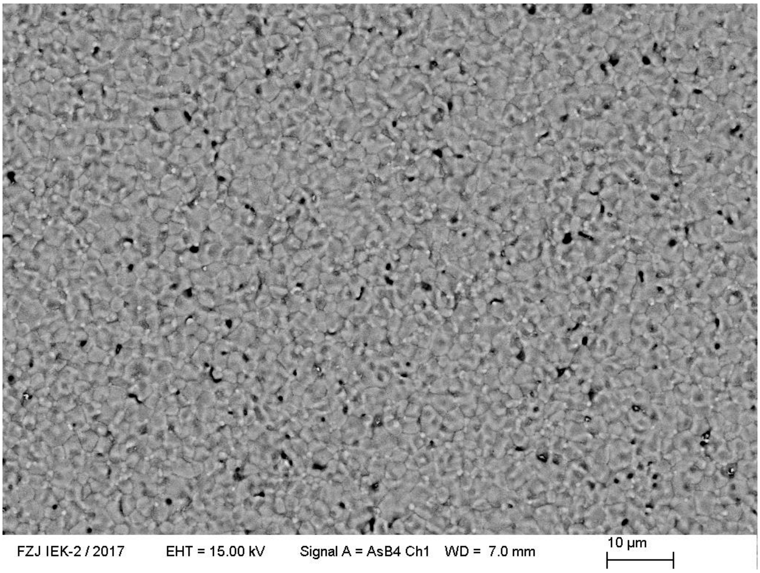

(b) LSCF-5, bottom side: no secondary phase particle.

Figure 3.29 SEM images of LSCF-5 samples after three-point-bending test.

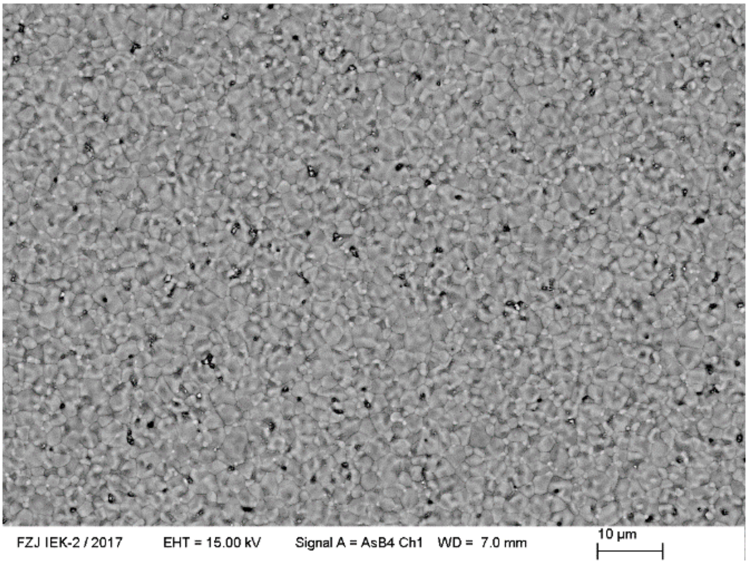

(a) LSCF-6, side 1

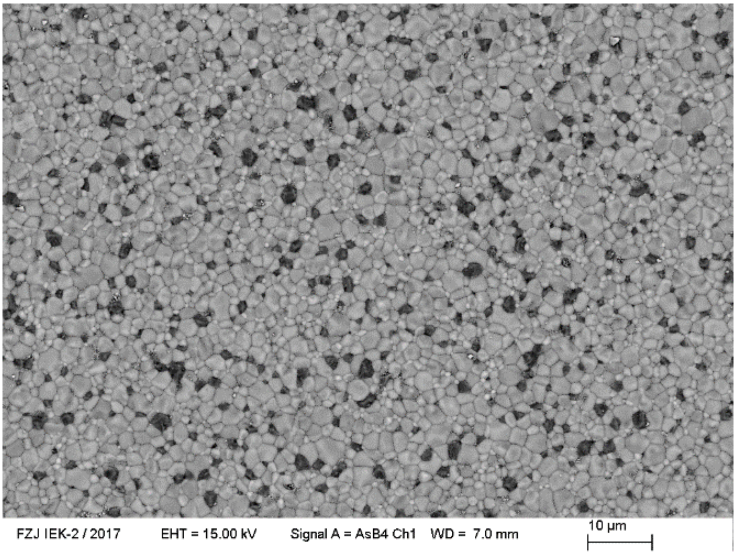

(b) LSCF-6, side 2: secondary phase particles, $FeCoO_x$

Figure 3.30 SEM images of as-received LSCF sample.

In this section, to assess the creep behavior of asymmetric membrane, sandwich samples of BSCF and LSCF were tested with three-point bending set-up with respect to the creep rupture behavior of the dense layer. Due to the large morphological changes, it is not possible to conclude if creep rupture can be critical for LSCF, however, the creep rupture features observed for the dense BSCF layer on porous substrate verifies that creep aspects are of concern for asymmetric membranes operated at elevated temperatures, especially when the substrate material possess higher deformation rates than the dense layer under the respective conditions. For the dense BSCF layer a creep rupture strain of 0.1 % was estimated based on creep rates and deformation using formulas given in literature [173], a value that is similar to creep rupture strains published for dense BSCF bulk material [115].

3.2. Freeze-cast 3 mol% Y_2O_3 doped ZrO_2 (3YSZ)[4]

3.2.1. Microstructure

Figure 3.31 illustrates the polished surface perpendicular (a-e) and parallel (f) of the freezing direction of freeze-cast specimens. Porosity of specimen FC57, FC60, FC63, FC66 and FC70 was evaluated from Figure 3.31(a-e) by image analysis, yielding the data in Table 3.4. Due to the high anisotropy of the pores, the morphological properties were characterized by measuring length and width in areas of 1 mm^2 using the micrographs presented in Figure 3.31(a-e). The measured values and the length/width ratio as function of the powder loading are given in Figure 3.32 as obtained from the images of polished cross-sections, Figure 3.31(a-e).

---

[4] Section content published. Y. Zou et al. / Journal of the European Ceramic Society 37 (2017) 3167–3176. http://dx.doi.org/10.1016/j.jeurceramsoc.2017.03.056

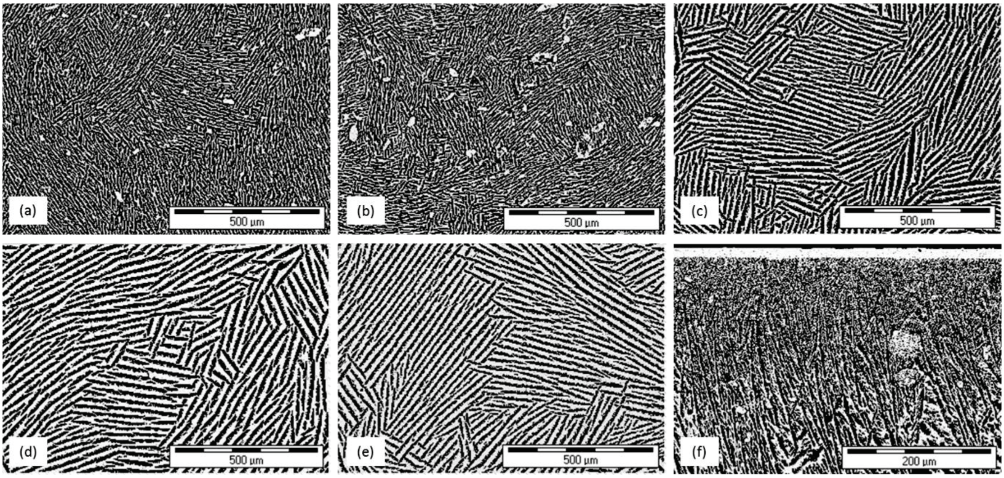

Figure 3.31 Top view (a-e) and cross-section (f) SEM micrographs of polished freeze-cast specimens: (a) FC57, (b) FC60, (c) FC63, (d) FC66, (e) FC70 and (f) FC+TL after sintering 6 h at 1390°C.

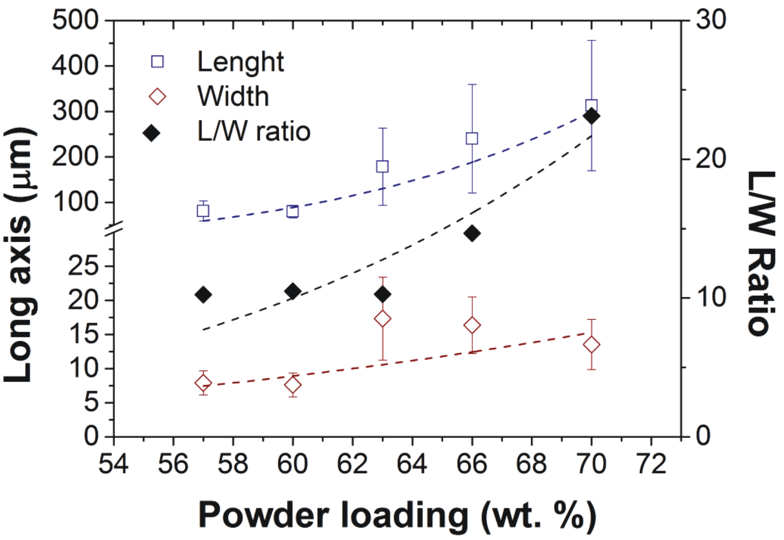

Figure 3.32 Pore size parameters as a function of solid loading and length/width pore ratio.

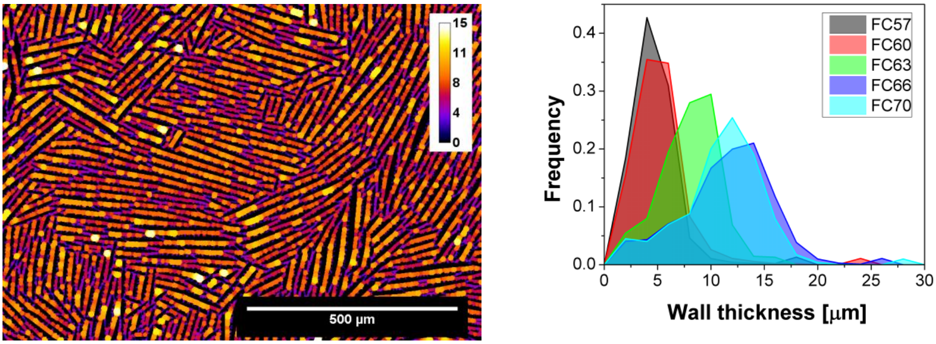

(a) (b)

Figure 3.33 Wall thickness measured by image analysis: (a) wall thickness of FC63, used the same image as Figure 3.31c; (b) wall thickness distribution of all freeze-cast samples.

As can be seen in the Figure 3.32, the pore dimensions of samples FC57 and FC60 are similar both in terms of length and width, but from sample FC63, the increment of the powder loading of the slurries causes an increment in pore length and a slight decrease in width. Considering the length/width ratio of the pore morphology of each sample, it can be appreciated how this value remains practically constant for samples FC57, F60 and FC63 and increases significantly for samples FC66 and FC70.

Regarding the freeze-cast samples without structuring agent (a-e), it can be observed that the final microstructure is directly influenced by the initial powder loading since its increase induces (i) a decrease of the overall porosity, (ii) an increase of the pore length (perpendicular to freeze direction), (iii) an increase of the interlamellar spacing and wall thickness and (iv) appearance of surface roughness between the ceramic walls. The wall thickness distributions are given in Figure 3.33, furthermore, the calculated mean wall thicknesses are also given in Table 3.4. With the powder loading, from 57% to 70%, the overall porosity decreases from 65% to 43% and the wall thickness increases from ~4 to ~10 µm. With the increase of powder loading, the size of these asperities increases up to bridging with the laminar wall facing it, thus changing the pore morphology. This observation has already been reported in literature [174] for highly concentrated solutions and might be explained by the engulfment of particle agglomerates created by particles repelled from the ice-water interface and subsequent tip healing. Figure 3.31f shows the cross-section of the sample with 8YSZ top layer (FC+TL). The porosity was not calculated since it varies through the thickness, which is a natural appearance of freeze-cast sample. A fully densified 8YSZ top layer can be seen.

Figure 3.34 shows typical microstructures for freeze-cast porous samples without structuring agent FC60 (Figure 3.34a) and with structuring agent FC60z (Figure 3.34b). The clear effect of the ZRA structuring agent onto the microstructure with the formation of a honeycomb-like structure (Figure 3.34b) very different from the similar sample produced without ZRA can be observed (Figure 3.34a). This structuring effect has been reported and detailed in [175], where the main explanation for such microstructure is the slower incorporation of water molecules onto the crystal surface resulting in a smooth internal and faceted growth. Details inside the lamellar structure walls were obtained using SEM of polished surfaces of FC60 (Figure 3.34c) and FC60z (Figure 3.34d). FC60 (Figure 3.34c) reveals a high density inside the lamellar walls with porosity about 1%. Other freeze-cast samples without ZRA structuring agent showed similar structure and porosity values (images not shown). FC60z with structuring agent showed a high porosity inside the honeycomb-like structure walls (Figure 3.34d) of about ~ 28%.

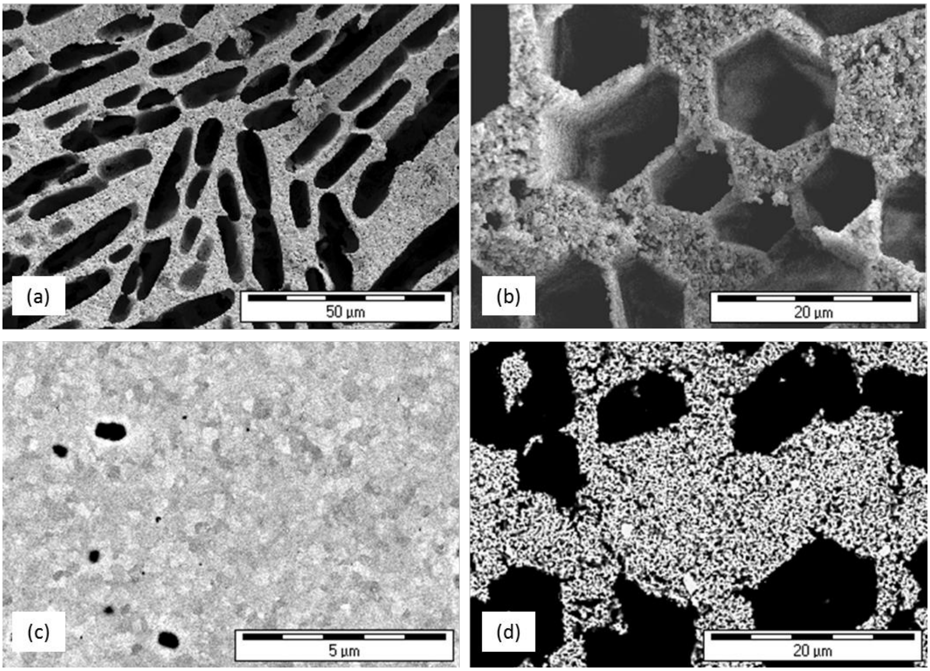

Figure 3.34 Top view FESEM micrographs of (a) FC60 and (b) FC60z. SEM micrographs of polished surfaces of (c) FC60 and (d) FC60z.

To assess the suitability of the freeze-cast material for the application in asymmetric material systems, mechanical tests have also been performed for the 3YSZ freeze-cast support (FC57) coated with an 8YSZ dense top layer. This assembly can be defined as a prototypical asymmetric membrane for oxygen separation from air. Indeed, the 8YSZ material has been chosen due to its high ionic conductivity in comparison with 3YSZ [176–178] and also for its chemical and thermal compatibilities which makes the manufacturing of membranes easier.

Figure 3.31f shows the polished cross-section of the FC+TL sample and Figure 3.35 illustrates details of the FC+TL sample in FESEM micrographs. It can be observed that the 8YSZ top layer is fully densified and homogeneous across its thickness, which is of about 15 µm (Figure 3.35a). Figure 3.35b and c present the surface of the top layer where a full grain consolidation can be observed, hence confirming the previous observation. Circular pinholes of approximately a few nanometers diameter are observable in a larger scale view, but should not be a problem for the application since they do not reach through the layer thickness.

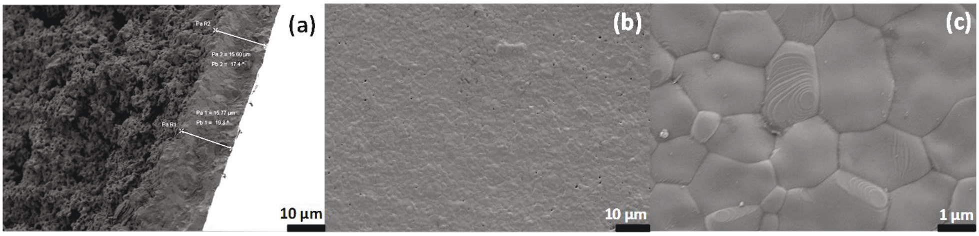

Figure 3.35 FESEM micrographs of FC+TL sample after sintering 6 h at 1390ºC: Cross-section of the 8YSZ dense top layer (TL) supported by a 3YSZ freeze-cast porous support (a), top views of the dense top layer (b and c).

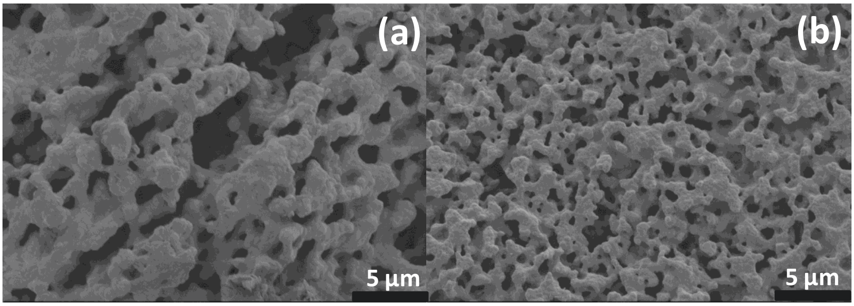

Figure 3.36 FESEM micrographs of cross-section (a) and surface (b) of the pressed / sintered 3YSZ with PMMA as pore former agent sample after sintering 6 h at 1390°C.

Figure 3.36 shows the microstructure of the PS42 sample elaborated by pressing and sintering a mixture of 3YSZ powder and PMMA pore former agent and after sintering 6 h at 1390°C. As expected, the sample has a randomly organized porosity all over its volume. The pores are small in the micron range (about 1-2 μm) in agreement with the initial PMMA polymeric powder and its average size of 1.5 μm.

3.2.2. Mechanical properties

The uncoated and coated 3YSZ substrates were tested with ring-on-ring bending tests (ROR). In addition, one complementary FC60 batch was tested via a proof-test procedure (labelled as FC60a and FC60b). Elastic moduli and fracture stresses were determined using linear bending theory. A detailed summary of tested specimens and results is shown in Table 3.4.

Mean fracture stress and mean elastic moduli are plotted as a function of porosity in Figure 3.37. These two properties show the same tendency with respect to porosity. PS42 (data in dashed frame) with isotropic pore structure has, as might be expected, a higher mean elastic modulus (16.5 ± 3.1 GPa) and mean fracture stress (56.0 ± 8.7 MPa). Batches FC57, FC60, FC63, FC66 and FC70 have similar mean elastic moduli (3.0 ~ 5.7 GPa) and mean fracture stress (16.1 ~ 19.8 MPa). In fact, mechanical properties did not change much within the considered porosity range (40 % ~ 65 %). FC60z, which has a hexagonal structure, has a lower mean fracture stress than FC60, which might be expected, since a) all the sharp angles in the hexagon shapes are stress concentrate point, which can then lead to fracture at a lower overall stress state; b) the high porosity inside the honeycomb-like structure walls (Figure 3.34d) leads to a further reduction of the mechanical strength. The large uncertainty associated with the presented elastic moduli and mean fracture stresses reflects also the limited number of available specimens.

Table 3.4 Details of tested specimens and results.

	Number of valid specimens	**Specimen Diameter [mm]**	**Specimen Thickness [mm]**	**Porosity [%]**	**Mean wall thickness [μm]**	**Mean elastic modulus *E* [GPa]**	**Mean fracture stress σ_f [MPa]**	**Inverse relative uncertainty of mean fracture stress η**
FC57	7	15.3 ± 0.1	1.4 ± 0.1	65.1 ± 2.5	4.1 ± 2.3	3.0 ± 0.9	16.2 ± 3.7	4.4
FC60	8	15.4 ± 0.1	1.5 ± 0.1	61.8 ± 3.0	4.6 ± 2.8	3.7 ± 0.4	19.0 ± 1.6	11.9
FC63	8	15.4 ± 0.2	1.7 ± 0.3	56.9 ± 2.7	7.3 ± 2.6	3.3 ± 3.1	16.1 ± 12.2	1.3
FC66	6	15.4 ± 0.1	1.7 ± 0.1	50.2 ± 2.2	10.6 ± 4.1	4.6 ± 2.0	19.8 ± 6.7	3.0
FC70	8	15.5 ± 0.1	1.5 ± 0.2	43.5 ± 2.9	10.2 ± 3.9	5.7 ± 4.1	17.7 ± 5.5	3.2
FC60a	15	15.1 ± 0.2	1.0 ± 0.1	61.3 ± 2.7	--	2.6 ± 0.8	12.5 ± 3.1	4.0
FC60b	13	15.1 ± 0.2	1.1 ± 0.1	61.3 ± 2.7	--	2.9 ± 1.2	12.6 ± 3.3	3.8
FC60z	5	16.5 ± 1.2	1.2 ± 0.1	45.7± 3.6	--	1.3 ± 0.5	5.2 ± 1.1	4.7
FC+TL	9	15.2 ± 1.1	1.5 ± 0.1	--	--	6.4 ± 1.5	23.7 ± 3.2	7.4
PS42	8	16.1 ± 0.1	2.0 ± 0.1	46.4 ± 2.3	--	16.5 ± 3.1	56.0 ± 8.7	6.4

For the application, it will be an advantage if weak specimens can be removed from the production via a pre-test, a mechanical proof test. In such a proof test a discrete stress is applied that is sufficient to remove for example all specimens with a failure probability of 1 %. However, the proof testing might induce additional defects or cause the growth of already existing defects via subcritical crack growth, hence, in the current study it was assessed if the proof testing affects the material or if it is a means to increase the reliability. Hence, a proof testing was additionally performed for batch FC60b to assess if proof testing affects the fracture stress and the proof test results were compared with group FC60a, which was tested with the normal ROR testing procedure.

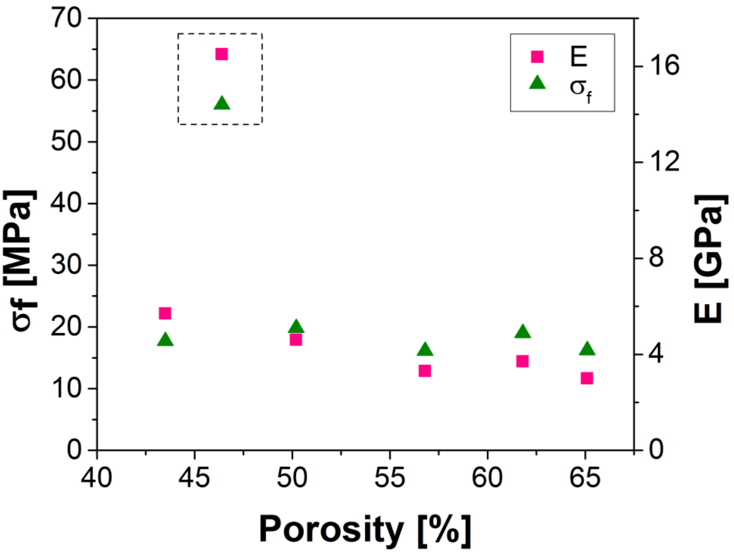

Figure 3.37 Mean fracture stresses (σ_f) and elastic moduli (E) versus porosity. Framed data points correspond to pressed sample PS42 and others freeze-cast samples.

In the proof test, specimens were first loaded (100 N/min) to 20 N (~12 MPa, failure probability ~50%), and then unloaded. If the specimens survive the pro-load, then the specimens were loaded again until fracture. The specimens that did not survive the pre-load were taken out and defined due to their limited quality as unsuitable specimens. Weibull plots of FC60a and FC60b with and without proof test are compared in Figure 3.38. Data labelled FC60a are the results for the normal test procedure, FC60b for all specimens from proof test no matter if the specimens fracture or not during the first loading, FC60ab combines the results from the former two groups and finally FC60b-Proof presents the results only those specimens that survived the first loading. The characteristic strength and Weibull modulus of FC60a are 13.7 MPa and 4.6, of FC60b are 13.9 MPa and 4.3, of FC60ab are 13.8 MPa and 4.6.

FC60b-Proof results in larger characteristic strength (15.3 MPa) and Weibull modulus (6.6). However, if the unsuitable data are added to the data set, the entire combined group of all samples (FC60ab) reveals good agreement with the initial test sets (FC60a and FC60b) that did not consider a proof test, hence confirming that the pre-load in proof testing did not influence in the specimens via subcritical crack growth. Therefore, the test procedure and results are reliable, verifying that proof testing is able to remove samples with lower fracture properties, hence, can be used in application to improve the in-service reliability.

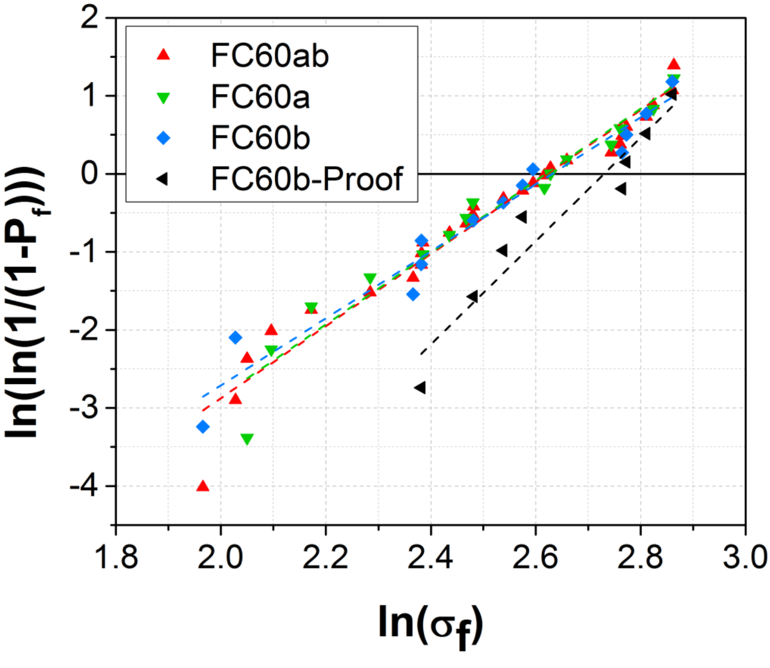

Figure 3.38 Weibull plots of proof-testing verification procedure results.

3.2.3. Pressure drop measurement

For the application as support of asymmetric gas-separation membranes, fast gas diffusion through the pore system in required, i.e. high gas permeance or low flow resistance. In general, it can be expected that, contrary to mean fracture stress and elastic modulus, the flow resistance decreases with increasing porosity. In the current work the flow resistance was assessed in terms of the pressure drop and permeation flux of the substrate materials.

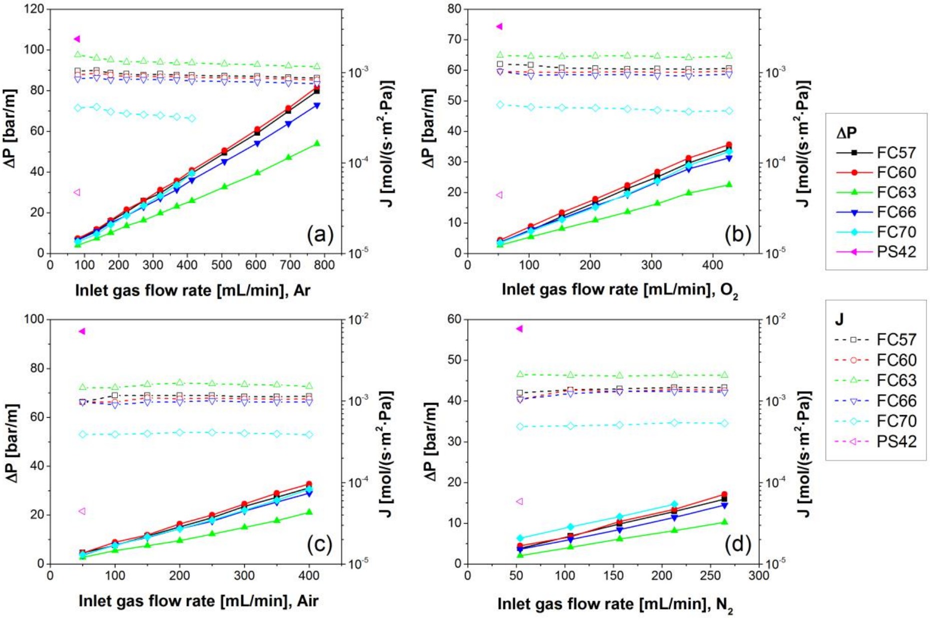

Figure 3.39 Pressure drop measurement and gas permeation flux results with inlet gas (a) Ar, (b) O2, (c) air and (d) N2. All samples have a thickness of 1 mm.

Figure 3.39 presents the pressure drop results in argon (a), oxygen (b), air (c) and nitrogen (d) and the derived gas permeation flux. For all samples, the pressure drop increases with the total inlet gas flow rate and with the ionic radius of gas molecules, as might be expected. In comparison with the specimens produced via pressing and sintering, the freeze-cast materials lead to significantly lower pressure drops. As an example, a pressure drop of more than 95 mbar/mm for the PS42 sample is observed when using 50mL/min of air as inlet flow in comparison with the 4 mbar/mm obtained under the same conditions for all freeze-cast samples. The maximum pressure drop obtained under air for freeze-cast supports is about 32 mbar/min corresponding to an inlet flow of 400 mL/min, still far of the 95 mbar/min previously detailed. These observations confirm the advantages of a freeze-cast hierarchical porous structure, where pressure loss can be strongly minimized and gas transport boosted. In terms of application, it means that higher operating flow rates can be obtained for the asymmetric membrane and thus a higher efficiency.

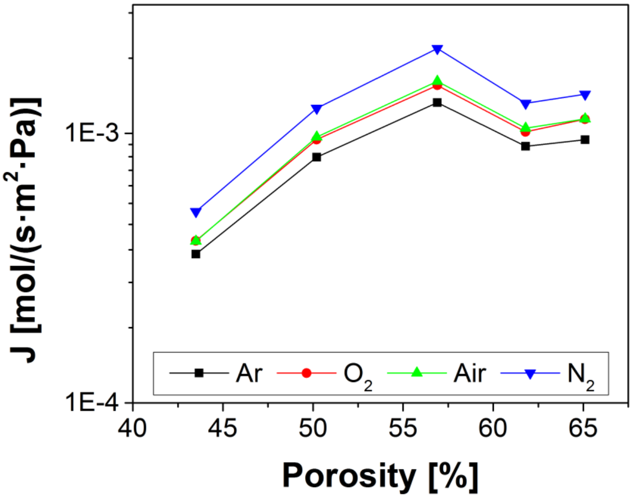

(a)

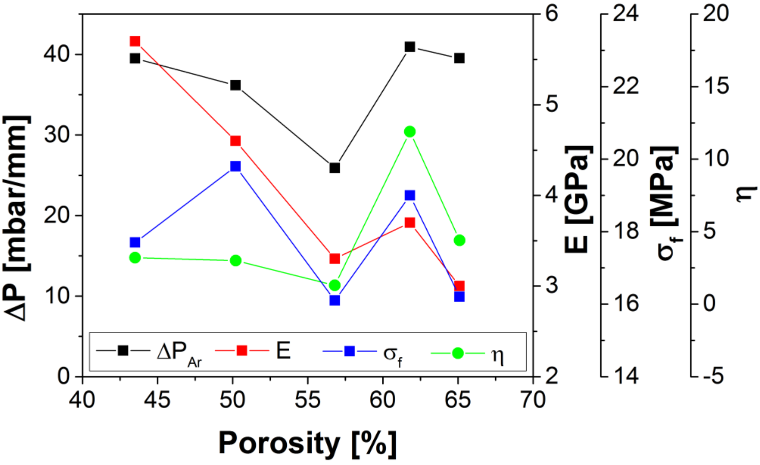

(b)

Figure 3.40 Plots of (a) gas permeation flux in different atmospheres; (b) Porosity dependence of pressure drop in Ar along with elastic modulus E, mean fracture stress σf, inverse relative uncertainty of mean fracture stress η.

Figure 3.40a presents the gas permeation flux of freeze-cast samples in different atmospheres as a function of porosity. Below 57% porosity, gas permeation flux increases with increasing porosity. A decrease in permeation was observed when the porosity increases beyond 57%, which can be explained by the change of morphology at this point (see Figure 3.31a-e). Samples with porosity higher than 57% (FC60, FC57) have smaller wall thickness and smaller interlamellar spacing compared to the other samples, which leads to a higher tortuosity of the microporous structure, and further leads to a decrease in permeability.

Figure 3.40b gives the porosity dependence of pressure drop in Ar along with mean elastic modulus *E*, mean fracture stress σ_f and the inverse relative uncertainty of mean fracture stress η. The inverse relative uncertainty of the average fracture stress is shown as a measure of the dispersion of the fracture stress data. A non-monotonous decrease of the all these properties was observed with increasing porosity, as might be expected. An increase occurs with respect to all properties beyond porosity 57%, where the morphology changes.

It is certain that besides the overall porosity, there are other pore structure parameters that play an important role on the strength of macroporous materials, which may refer to pore geometry, pore orientation and wall thickness. In the work of Seuba et al. [138], they suggested that wall thickness is the key morphological parameter on mechanical reliability and strength of macroporous materials. Both Weibull modulus and strength tend to increase with smaller wall thickness and this can be attributed to the reduced probability of finding a catastrophic defect in thinner walls. Similar effects are observed in the present work, see Figure 3.40b, elastic modulus, mean fracture strength and inverse relative uncertainty of mean fracture stress (For large number of tested specimens the inverse relative uncertainty of the average fracture stress basically becomes very similar to the Weibull modulus of a fracture stress distribution [179].) all increase after the morphology change point beyond 57% porosity.

Seuba et al. [138] also suggested that strength is mainly determined by the total porosity and the effect of morphological parameters like wall thickness is relatively weak. In the present work, the influence of the morphological parameters seems to be rather strong. Figure 3.40b suggests that fracture stress may decrease with porosity, but the huge variation may also indicate that there is no fracture stress change with respect to porosity in the range 43% to 65%. This behavior suggests that the effect of morphological parameters on fracture stress almost overwhelm the contribution of total porosity. This phenomenon may be explained by the ring-on-ring test obtained fracture stress characterized in the present work instead of compression strength reported in literature. When the samples are loaded along freezing direction in a bending test, with long pores, namely, long walls, tend to have a leverage effect, will break with lower loads. Therefore, in a bending test, the pore geometry, besides wall thickness and total porosity, is also an important morphological parameter on mechanical properties.

Strong increases in all parameters are observed when changing the porosity from 43 to 57%. The smallest increase is in fact observed for the elastic modulus which in terms of mechanical properties is an integral property that depends on all pores and defects in the volume, where a recent work [180] reports that larger pores have a stronger effect than small pores. Stronger effects are observed for the strength which is via the weakest link related to the largest defects in the material and the Weibull modulus, which indicates the reliability being related to the distribution of defects, i.e. a higher value indicates a more homogeneous distribution of defects. Looking at the failure strain it in fact increases rather continuously with values of 0.31, 043, 0.49, 0.51 and 0.54% for the considered porosities, indicating increasing strain tolerance, however also proving that the effect causing the discontinuous behavior in the other parameters is not reflected in the failure strain. Overall the observed increase in mechanical parameters indicates that increasing the porosity to 57% leads to a more homogeneous pore distribution (Weibull modulus) with average smaller pores (elastic modulus) and reduced maximum defect size, i.e. less large pores (strength), this smaller pores then also lead to an increase in flow resistance.

In this section, mechanical properties and pressure drop effect of freeze-cast porous 3YSZ material were studied and discussed in terms of the influence of overall porosity and pore structure. Comparing with porous 3YSZ material from conventional pressing and sintering production process, freeze-cast material appears to have inferior mechanical properties, i.e. elastic modulus and fracture strength, but as an advantage of lower pressure drop effect. Hence, as expected, minimizing the pressure loss goes along with a reduction of the mechanical stability. An optimized balance between the two aspects is needed to be achieved which should be the aim of future developments.

However, although all properties reveal a similar tendency, there is no monotonous decrease with increasing porosity, as might be expected. It appears that there is not only an influence of the overall porosity, the pore structure seems also to play an important role, which may refer to pore size, pore orientation and wall thickness.

3.3. Comparison of LSCF and 3YSZ porous substrates

In the current thesis, porous LSCF and 3YSZ samples with different porosity and different porous structures were both produced as porous substrates material for OTM components. Whereas for LSCF the work mainly concentrated on the effect of the porous structures on creep behavior, for 3YSZ the studies focused on the correlation of mechanical parameters and functional gas permeability. As a substrate material selection criteria, the compatibility with the dense functional layer is of great importance. But in this section, these two porous substrate materials are compared with each other only according to their mechanical behavior despite of the dense functional layer. For a dense LCSF membrane layer, a porous LSCF layer has obvious advantages with respect to thermal expansion and processing (i.e. sintering, bonding), whereas for the application of other layers, i.e. $Ce_{0.9}Gd_{0.1}O_{1.95-\delta}$, a careful consideration of advantages and disadvantages of different potential substrate materials, also with respect to the apparent mechanical behavior, is necessary

At room temperature, the dense LSCF has elastic moduli between 60 – 180 GPa depending on the used measurement techniques (IET), see Figure 3.11, while dense 3YSZ yields an value of around 220 GPa by IET [136]. Porous LSCF from tape-casting and freeze-casting with porosity about 45% have elastic moduli of about 12 GPa (see Figure 3.11), while freeze-cast 3YSZ with porosity 43% has an elastic modulus of around 6 GPa and uniaxial pressed 3YSZ with porosity 46% possesses an elastic modulus of approximately 16 GPa, see Figure 3.37. Hence, in a dense state 3YSZ yields higher values, whereas in a porous state LCSF indicates a higher elastic modulus, however, note, as recently verified by Zhang et al. [180] such elastic moduli – porosity dependencies depend strongly on the actual pores size.

In a ring-on-ring bending test, dense LSCF showed a bending fracture strength of approximately 70 MPa, while the tape-cast 46% porous LSCF revealed a strength of about 20 MPa [32]. In the cyclic compressive loading test illustrated in Figure 3.8, freeze-cast LSCF with porosity about 44% showed an initial crack under a loading of ~ 60 MPa for a longitudinal strain of -0.315 % and until a loading to about 98.0 MPa, the specimen was gradually crushed. Dense 3YSZ revealed a very high strength of about 700 MPa with biaxial flexure test [135]. For freeze-cast 45% porosity 3YSZ under a compressive load, the crashing strength is between 50 – 300 MPa regarding to different porous structures, see Figure 1.23 [137]. In a ring-on-ring bending test, the freeze-cast 3YSZ samples with porosity 43 – 65% had a fracture strength about 20 MPa, while the uniaxial pressed sample with 46% porosity had a much higher strength about 55 MPa, see Figure 3.37.

Even though dense 3YSZ has much higher elastic modulus and fracture strengths than dense LSCF, considering porous material, the porous 3YSZ shows no apparent advantages over LSCF. When only considering the freeze-cast material, 3YSZ show an even smaller elastic modulus than LSCF. With respect to fracture strength, porous 3YSZ shows similar values as porous LSCF. It indicates that for high porosities (> 40%), the material with the higher bulk properties loses its mechanical advantages and the differences in mechanical behavior diminishes compared to that of dense materials. For porous materials, the overall fractional porosity and the porous structure are the most important parameters influencing the elastic modulus and fracture strength. Besides, smaller elastic modulus means smaller strain tolerance for similar fracture strengths, i.e.

smaller elastic modulus means larger fracture strain. When the material is under a strain controlled loading status, the freeze-cast 3YSZ might be survivor, however, design of membrane units also requires consideration of Weibull moduli and failure probabilities for room and application relevant temperatures, hence, requiring test series of larger number of specimens of the actual batches produced for the particular purpose since processing is known to be a factor that affects strongly these parameters.

Comparing the creep rates of LSCF (Figure 3.21) and 3YSZ (Figure 1.27 [93]), LSCF yields much higher values than 3YSZ, i.e. about 2 to 3 orders of magnitude higher. Under application relevant temperatures, the creep deformation can release the stresses induced to the multi-layer component like an OTM and SOFC module. But on the other hand, for long-term operation, the creep deformation will change the geometry of the component and further can result in creep rupture and the component might lose its geometry integrity and cannot keep its functionality. Therefore, the 3YSZ material with relative low creep rates and known as super-plastic ceramic under high temperatures can be advantageous as a substrate material keeping its geometry integrity under long-term operation conditions.

Overall, only considering the mechanical properties like elastic modulus, fracture strength and creep responses, the porous freeze-cast 3YSZ, with larger fracture strain, lower creep rates and possible larger creep rupture strain, might be the better candidate as porous substrate material in OTM application.

Chapter 4.

Conclusions

In this thesis the mechanical behaviors of selected membrane and substrate materials have been compiled and documented.

- High temperature XRD of LSCF

The aim was to verify the exact rhombohedral - cubic phase change temperature of LSCF. The phase change completes at 750°C (50 K to 100 K temperature steps). Furthermore, at 650°C no reflex splitting of the cubic 3 3 2 – peak can be seen anymore (no image shown), which again indicates a phase change between 650 °C and 750 °C.

- Elastic and fracture properties of freeze-cast LSCF

Elastic parameters, namely Young's, shear and bulk moduli as well as Poisson's ratio of freeze-cast LSCF were investigated at room temperature by a quasi-static hysteresis compression test. The evolution of these elastic parameters is studied as a function of the longitudinal strain. The elastic parameters showed extrema related to ferroelastic domain switching. Young's and shear moduli revealed minimum values, while bulk modulus and Poisson's ratio demonstrated maximum values due to the transverse strain contributed by ferroelastic domain switching.

- Ferroelastic behavior of porous LSCF

Compression stress-strain curves at room temperature revealed a non-linear behaviour similar as reported for dense LSCF58. Such a phenomenon can be explained by the ferroelasticity of the perovskite material in its low temperature stable rhombohedral phase, which was also reflected in a distinctive ferroelastic creep.

- Creep properties of tape-cast, freeze-cast, and pressing LSCF

LSCF specimens prepared with uniaxial pressing, tape-cast, and freeze-cast at IEK-1, Forschungszentrum Jülich GmbH, which had different porosities and pore structures, were investigated via an uniaxial compression test for high temperature creep behaviour. All porous samples have higher creep rates than the dense material, as might be expected, and all of the creep rates exceed the 1 % creep strain per year criteria (3.2×10-10 s^{-1}), which is expected to be critical for application. Regarding different synthesis methods, it seems that the tape-cast material has the lowest creep rate compared to the other two methods with similar porosities, while the specimen from uniaxial pressing leads to the highest creep rates. Reason for the difference between the different methods is not yet clarified and should be the aim of future studies.

Since the creep deformation appears to exceed an acceptable level, a strategy for reduction of the creep deformation should be a decrease of the operation temperature and/or operational loads by a respective design of the membrane module. However, lower flux in case of lower temperature has to be considered. In order to compensate the material creep, a smart design of the support microstructure might be an option as reported for a new generation of supports with straight pore channels perpendicular to the load direction, manufactured by freeze drying.

- Creep rupture of LSCF

To assess the creep behavior of asymmetric membrane, sandwich samples of BSCF and LSCF were tested with three-point bending set-up with respect to the creep rupture behavior of the dense layer. Due to the large morphological changes, it is not possible to conclude if creep rupture can be critical for LSCF, however, the creep rupture features observed for the dense BSCF layer on porous substrate verifies that creep aspects are of concern for asymmetric membranes operated at elevated temperatures, especially when the substrate material possess higher deformation rates than the dense layer under the respective conditions.

- Elastic and fracture properties of freeze-cast 3YSZ

Mechanical properties and pressure drop effect of freeze-cast porous 3YSZ material were studied and discussed in terms of the influence of overall porosity and pore structure. Comparing with porous 3YSZ material from conventional pressing and sintering production process, freeze-cast material appears to have inferior mechanical properties, i.e. elastic modulus and fracture strength, but as an advantage of lower pressure drop effect. Note, although the low strength indicates inferior performance under external mechanical loads as might be induced by pressure differences or handling, it can be easily derived that the freeze-cast material has a rather high critical strain compared to tape-cast material, indicating that under the action of thermally induced strains (differences in thermal expansion), the material can be even superior. Hence, as expected, minimizing the pressure loss goes along with a reduction of the mechanical stability. An optimized balance between the two aspects is needed to be achieved which should be the aim of future developments. However, although all properties reveal a similar tendency, there is no monotonous decrease with increasing porosity, as might be expected. It appears that there is not only an influence of the overall porosity, the pore structure seems also to play an important role, which may refer to pore size, pore orientation and wall thickness.

Appendices

A.1 XRD measurement details.

Table A.1 Initial measurement from RT to 800°C, sample on PtRh heating tape.

Scan-No.	T	Heating rate	$2\theta_{Start}$	$2\theta_{end}$	$\Delta 2\theta$	t/step	Holding time	Measure time
	°C	K/s	°	°	s	s	s	s
1	25		20	70	0.02	3	0	7500
2	100	0.1	20	70	0.02	3	600	7500
3	200	0.1	20	70	0.02	3	600	7500
4	300	0.1	20	70	0.02	3	600	7500
5	400	0.1	20	70	0.02	3	600	7500
6	500	0.1	20	70	0.02	3	600	7500
7	600	0.1	20	70	0.02	3	600	7500
8	700	0.1	20	70	0.02	3	600	7500
9	800	0.1	20	70	0.02	3	600	7500
10	700	0.1	20	70	0.02	3	600	7500
11	600	0.1	20	70	0.02	3	600	7500
12	500	0.1	20	70	0.02	3	600	7500
13	400	0.1	20	70	0.02	3	600	7500
14	300	0.1	20	70	0.02	3	600	7500
15	200	0.1	20	70	0.02	3	600	7500
16	100	0.1	20	70	0.02	3	600	7500
17	25	20	70	0.02	3	600	7500	

Total time: 42:10:50 h

Table A.2 Second measurement from RT to 1000°C, sample on Pt heating tape.

Scan-No.	T	Heating rate	$2\theta_{\mathrm{Start}}$	$2\theta_{\mathrm{end}}$	$\Delta 2\theta$	t/step	Holding time	Measure time
	°C	K/s	°	°	s	s	s	s
1	25	20	80	0.02	5	0	15000	
2	25	133	141	0.02	10	0	4000	
3	100	0.1	20	80	0.02	5	600	15000
4	100	0.1	133	141	0.02	10	0	4000
5	200	0.1	20	80	0.02	5	600	15000
6	200	0.1	133	141	0.02	10	0	4000
7	300	0.1	20	80	0.02	5	600	15000
8	300	0.1	133	141	0.02	10	0	4000
9	400	0.1	20	80	0.02	5	600	15000
10	400	0.1	133	141	0.02	10	0	4000
11	500	0.1	20	80	0.02	5	600	15000
12	500	0.1	133	141	0.02	10	0	4000
13	600	0.1	20	80	0.02	5	600	15000
14	600	0.1	133	141	0.02	10	0	4000
15	650	0.1	20	80	0.02	5	600	15000
16	650	0.1	133	141	0.02	10	0	4000
17	700	0.1	20	80	0.02	5	600	15000
18	700	0.1	133	141	0.02	10	0	4000
19	750	0.1	20	80	0.02	5	600	15000
20	750	0.1	133	141	0.02	10	0	4000
21	800	0.1	20	80	0.02	5	600	15000
22	800	0.1	133	141	0.02	10	0	4000
23	850	0.1	20	80	0.02	5	600	15000
24	850	0.1	133	141	0.02	10	0	4000
25	900	0.1	20	80	0.02	5	600	15000
26	900	0.1	133	141	0.02	10	0	4000
27	950	0.1	20	80	0.02	5	600	15000
28	950	0.1	133	141	0.02	10	0	4000
29	1000	0.1	20	80	0.02	5	600	15000
30	1000	0.1	133	141	0.02	10	0	4000
31	900	0.1	20	80	0.02	5	600	15000
32	900	0.1	133	141	0.02	10	0	4000
33	800	0.1	20	80	0.02	5	600	15000
34	800	0.1	133	141	0.02	10	0	4000
35	700	0.1	20	80	0.02	5	600	15000
36	700	0.1	133	141	0.02	10	0	4000
37	600	0.1	20	80	0.02	5	600	15000
38	600	0.1	133	141	0.02	10	0	4000

39	500	0.1	20	80	0.02	5	600	15000
40	500	0.1	133	141	0.02	10	0	4000
41	400	0.1	20	80	0.02	5	600	15000
42	400	0.1	133	141	0.02	10	0	4000
43	300	0.1	20	80	0.02	5	600	15000
44	300	0.1	133	141	0.02	10	0	4000
45	200	0.1	20	80	0.02	5	600	15000
46	200	0.1	133	141	0.02	10	0	4000
47	100	0.1	20	80	0.02	5	600	15000
48	100	0.1	133	141	0.02	10	0	4000
49	25	20	145	0.02	10	600	62500	

Total time: 153:14:10 h

A.2 Stress exponent calculations for LSCF creep

Table A.3 Summary of LSCF high temperature creep stress exponents.

	Temperature [°C]	Average stress exponent *n*
Dense	850-1000	1.37
TCL	800-1000	1.82
WP90	800-1000	2.12
WP70	800	1.79
FC30V	850-1000	2.35
FC25V	850-1000	2.07
FC25P	850-1000	1.52

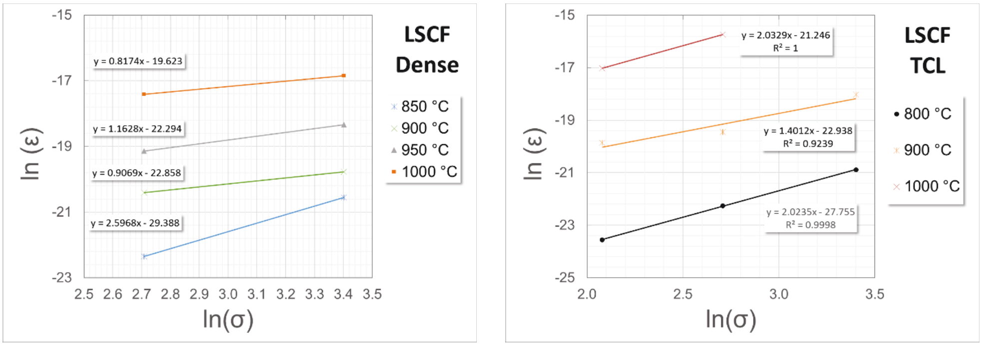

(a) (b)

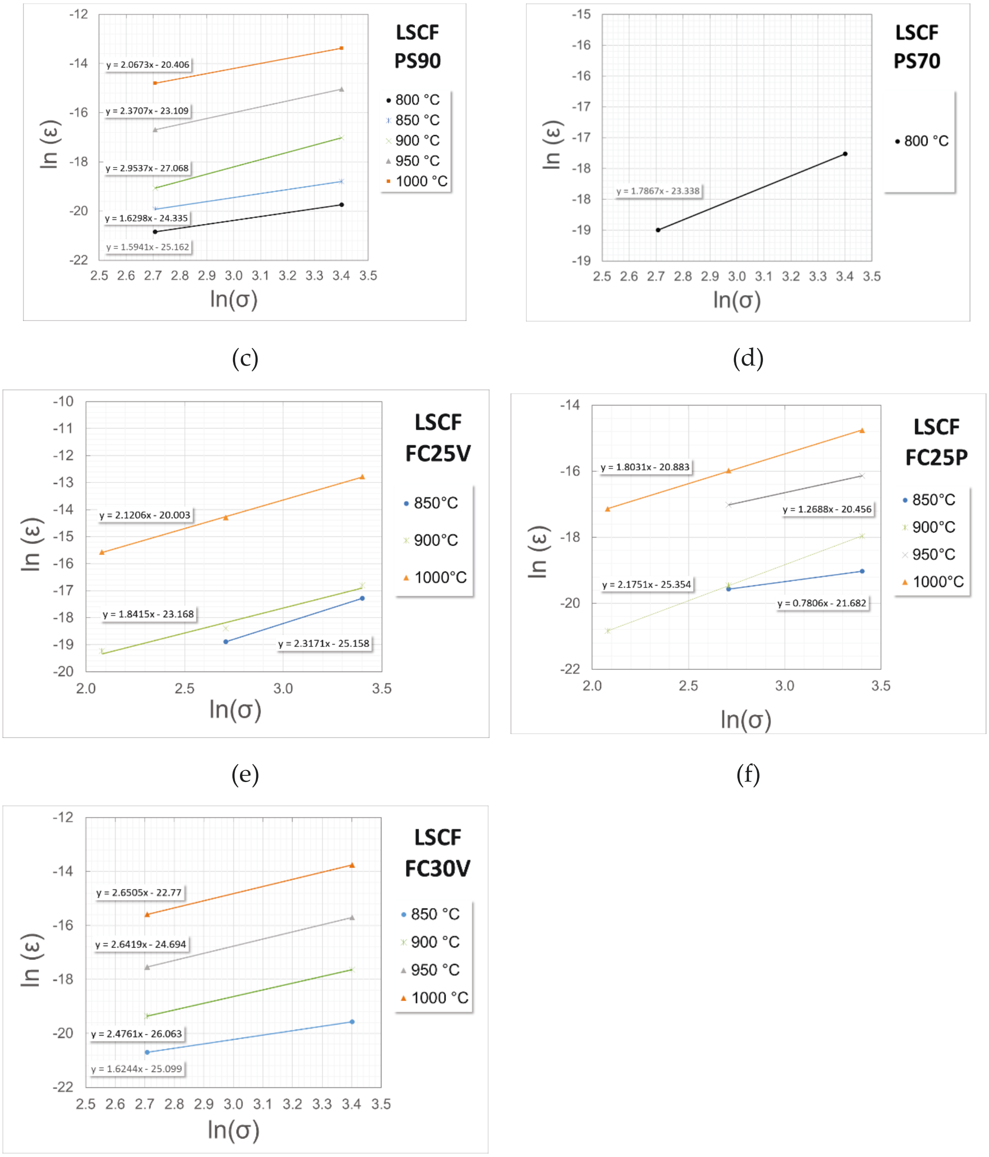

(c)

(d)

(e)

(f)

(g)

Figure A.1 Natural exponential plots of creep rate on stress for stress exponent calculation.

Bibliography

[1] C. Hodrien, Squaring the Circle on Coal - Carbon Capture and Storage, in: Clavert. Energy Gr. Conf., Bath, 2008. http://www.claverton-energy.com/wordpress/wp-content/files/ccs-squaring-the-circle-on-carbon-capture-and-storage-c-hodrien-claverton-energy-group-bath-october-2008.pdf.

[2] T.F.. et al. Stocker, The Physical Science Basis - Summary for Policymakers, Observed Changes in the Climate System, in: IPCC, Clim. Chang. 2013, Cambridge University Press, 2013: p. 15.

[3] M. Hartmann, D. L.; Klein Tank, A. M. G.; Rusticucci, 2: Observations: Atmosphere and Surface, in: IPCC WGI AR5, 2013: p. 198.

[4] R. Lal, Forest soils and carbon sequestration, For. Ecol. Manage. 220 (2005) 242–258. doi:10.1016/j.foreco.2005.08.015.

[5] T.E. Graedel, The Pieces of the Periodic Table Nature's Building Blocks: An A-Z Guide to the Elements, by John Emsley World of the Elements, Elements of the World, by Hans-Jurgen Quadbeck-Seeger, J. Ind. Ecol. 13 (2009) 154–155. doi:10.1111/j.1530-9290.2008.00080_3.x.

[6] A.C. Bose, G.J. Stiegel, P.A. Armstrong, B.J. Halper, E.P. (Ted) Foster, Progress in Ion Transport Membranes for Gas Separation Applications, in: A.C. Bose (Ed.), Inorg. Membr. Energy Environ. Appl., Springer New York, New York, NY, 2009: pp. 3–25. doi:10.1007/978-0-387-34526-0_1.

[7] Y. He, X. Zhu, Q. Li, W. Yang, Perovskite oxide absorbents for oxygen separation, AIChE J. 55 (2009) 3125–3133. doi:10.1002/aic.11931.

[8] H.J.M. Bouwmeester, Chapter 10 Dense ceramic membranes for oxygen separation, Membr. Sci. Technol. 4 (1996) 435–528. doi:10.1016/S0927-5193(96)80013-1.

[9] S.P.S. Badwal, F.T. Ciacchi, Ceramic Membrane Technologies for Oxygen Separation, Adv. Mater. 13 (2001) 993–996. doi:10.1002/1521-4095(200107)13:12/13<993::AID-ADMA993>3.0.CO;2-#.

[10] M. Lipinska-Chwalek, J. Malzbender, A. Chanda, S. Baumann, R.W. Steinbrech, Mechanical characterization of porous Ba0.5Sr0.5Co0.8Fe0.2O3−d, J. Eur. Ceram. Soc. 31 (2011) 2997–3002. doi:10.1016/j.jeurceramsoc.2011.07.002.

[11] F. Schulze-Küppers, S. Baumann, W.A. Meulenberg, D. Stöver, H.P. Buchkremer, Manufacturing and performance of advanced supported Ba0.5Sr0.5Co0.8Fe0.2O3-?? (BSCF) oxygen transport membranes, J. Memb. Sci. 433 (2013) 121–125. doi:10.1016/j.memsci.2013.01.028.

[12] S. Baumann, J.M. Serra, M.P. Lobera, S. Escolástico, F. Schulze-Küppers, W.A. Meulenberg, Ultrahigh oxygen permeation flux through supported Ba0.5Sr0.5Co0.8Fe0.2O3−δ membranes, J. Memb. Sci. 377 (2011) 198–205. doi:10.1016/j.memsci.2011.04.050.

[13] X. CHANG, C. ZHANG, Y. HE, X. DONG, W. JIN, N. XU, A Comparative Study of the Performance of Symmetric and Asymmetric Mixed-conducting Membranes, Chinese J. Chem. Eng. 17 (2009) 562–570. doi:10.1016/S1004-9541(08)60245-1.

[14] J. Gurauskis, Ø.F. Lohne, H.L. Lein, K. Wiik, Processing of thin film ceramic membranes for oxygen separation, J. Eur. Ceram. Soc. 32 (2012) 649–655. doi:10.1016/j.jeurceramsoc.2011.10.009.

[15] J.M. Serra, J. Garcia-Fayos, S. Baumann, F. Schulze-Küppers, W.A. Meulenberg, Oxygen permeation through tape-cast asymmetric all-La0.6Sr0.4Co0.2Fe0.8O3−δ membranes, J. Memb. Sci. 447 (2013) 297–305. doi:10.1016/j.memsci.2013.07.030.

[16] S.M. Hashim, A.R. Mohamed, S. Bhatia, Current status of ceramic-based membranes for oxygen separation from air, Adv. Colloid Interface Sci. 160 (2010) 88–100. doi:10.1016/j.cis.2010.07.007.

[17] Y.-S. Lin, W. Wang, J. Han, Oxygen permeation through thin mixed-conducting solid oxide membranes, AIChE J. 40 (1994) 786–798. doi:10.1002/aic.690400506.

[18] G.Z. Cao, Electrical conductivity and oxygen semipermeability of terbia and yttria stabilized zirconia, J. Appl. Electrochem. 24 (1994) 1222–1227. doi:10.1007/BF00249885.

[19] J. Sunarso, S. Baumann, J.M. Serra, W.A. Meulenberg, S. Liu, Y.S. Lin, J.C. Diniz da Costa, Mixed ionic-electronic conducting (MIEC) ceramic-based membranes for oxygen separation, J. Memb. Sci. 320 (2008) 13–41. doi:10.1016/j.memsci.2008.03.074.

[20] J.W. Stevenson, T.R. Armstrong, R.D. Carneim, L.R. Pederson, W.J. Weber, Electrochemical Properties of Mixed Conducting Perovskites La1 − x M x Co1 − y Fe y O 3 − δ (M = Sr, Ba, Ca), J. Electrochem. Soc. 143 (1996) 2722–2729. doi:10.1149/1.1837098.

[21] M. Ikeguchi, Y. Yoshino, K. Kanie, M. Nomura, E. Kikuchi, M. Matsukata, Effects of preparation method on oxygen permeation properties of SrFeCo0.5Ox membrane, Sep. Purif. Technol. 32 (2003) 313–318. doi:10.1016/S1383-5866(03)00048-0.

[22] P. Zeng, R. Ran, Z. Chen, H. Gu, Z. Shao, J.C.D. da Costa, S. Liu, Significant effects of sintering temperature on the performance of La0.6Sr0.4Co0.2Fe0.8O3-d oxygen selective membranes, J. Memb. Sci. 302 (2007) 171–179.

[23] S. Baumann, F. Schulze-Küppers, S. Roitsch, M. Betz, M. Zwick, E.M. Pfaff, W.A.

Meulenberg, J. Mayer, D. Stöver, Influence of sintering conditions on microstructure and oxygen permeation of Ba0.5Sr0.5Co0.8Fe0.2O3-?? (BSCF) oxygen transport membranes, J. Memb. Sci. 359 (2010) 102–109. doi:10.1016/j.memsci.2010.02.002.

[24] M. Schulz, U. Pippardt, L. Kiesel, K. Ritter, R. Kriegel, Oxygen permeation of various archetypes of oxygen membranes based on BSCF, AIChE J. 58 (2012) 3195–3202. doi:10.1002/aic.13843.

[25] C. Wagner, {Ü}ber den Mechanismus der elektrischen Stromleitung im Nernststift, Naturwissenschaften. 31 (1943) 265–268. doi:10.1007/BF01475685.

[26] H. Kusaba, Y. Shibata, K. Sasaki, Y. Teraoka, Surface effect on oxygen permeation through dense membrane of mixed-conductive LSCF perovskite-type oxide, Solid State Ionics. 177 (2006) 2249–2253. doi:10.1016/j.ssi.2006.05.038.

[27] P. Haworth, S. Smart, J. Glasscock, J.C. Diniz da Costa, High performance yttrium-doped BSCF hollow fibre membranes, Sep. Purif. Technol. 94 (2012) 16–22. doi:10.1016/j.seppur.2012.04.005.

[28] T. Schiestel, M. Kilgus, S. Peter, K.J. Caspary, H. Wang, J. Caro, Hollow fibre perovskite membranes for oxygen separation, 2005. doi:10.1016/j.memsci.2005.03.035.

[29] H. Wang, C. Tablet, J. Caro, Oxygen production at low temperature using dense perovskite hollow fiber membranes, J. Memb. Sci. 322 (2008) 214–217. doi:10.1016/j.memsci.2008.05.038.

[30] W.K. Hong, G.M. Choi, Oxygen permeation of BSCF membrane with varying thickness and surface coating, J. Memb. Sci. 346 (2010) 353–360. doi:10.1016/j.memsci.2009.09.056.

[31] Y. Zou, F. Schulze-Küppers, J. Malzbender, Creep behavior of porous La0.6Sr0.4Co0.2Fe0.8O3-?? oxygen transport membrane supports, Ceram. Int. 41 (2015) 4064–4069. doi:10.1016/j.ceramint.2014.11.100.

[32] G. Pećanac, S. Foghmoes, M. Lipińska-Chwałek, S. Baumann, T. Beck, J. Malzbender, Strength degradation and failure limits of dense and porous ceramic membrane materials, J. Eur. Ceram. Soc. 33 (2013) 2689–2698. doi:10.1016/j.jeurceramsoc.2013.04.018.

[33] P. Niehoff, S. Baumann, F. Schulze-Kuppers, R.S. Bradley, I. Shapiro, W.A. Meulenberg, P.J. Withers, R. Vassen, Oxygen transport through supported Ba0.5Sr0.5Co0.8Fe0.2O3-delta membranes, Sep. Purif. Technol. 121 (2014) 60–67. doi:10.1016/j.seppur.2013.07.002.

[34] M. Lipińska-Chwałek, G. Pećanac, J. Malzbender, Creep behaviour of membrane and substrate materials for oxygen separation units, J. Eur. Ceram. Soc. 33 (2013) 1841–1848. doi:10.1016/j.jeurceramsoc.2013.02.007.

[35] V. Stournari, W. Deibert, M.E. Ivanova, C. Krautgasser, R. Bermejo, J. Malzbender, Mechanical properties of tape casted Lanthanum Tungstate for membrane substrate

application, Ceram. Int. 42 (2016) 15177–15182. doi:http://dx.doi.org/10.1016/j.ceramint.2016.06.109.

[36] Y. Zou, W. Araki, M. Balaguer, J. Malzbender, Elastic properties of freeze-cast La0.6Sr0.4Co0.2Fe0.8O3-??, J. Eur. Ceram. Soc. 36 (2016) 1651–1657. doi:10.1016/j.jeurceramsoc.2016.01.034.

[37] B.C. Bonekamp, Chapter 6: Preparation of asymmetric ceramic membrane supports by dip-coating, in: A.J. Burggraaf, L. Cot (Eds.), Fundam. Inorg. Membr. Sci. Technol., Elsevier, 1996: p. 141.

[38] C. Gaudillere, J.M. Serra, Freeze-casting: Fabrication of highlyporous and hierarchical ceramic supports for energy applications, Bol. La Soc. Esp. Ceram. Y Vidr. 55 (2016) 45–54. doi:10.1016/j.bsecv.2016.02.002.

[39] B.C. Steele, Ceramic ion conducting membranes, Curr. Opin. Solid State Mater. Sci. 1 (1996) 684–691. doi:10.1016/S1359-0286(96)80052-0.

[40] S.S. Lion, W.L. Worrell, Electrical properties of novel mixed-conducting oxides, Appl. Phys. A Solids Surfaces. 49 (1989) 25–31. doi:10.1007/BF00615461.

[41] B. Calés, J. Baumard, Mixed Conduction and Defect Structure of ZrO -CeO -Y203 Solid Solutions, J. Electrochem. Soc. 45 (1984) 2407–2413. doi:10.1149/1.2115267.

[42] W.D. KINGERY, J. PAPPIS, M.E. DOTY, D.C. HILL, Oxygen Ion Mobility in Cubic Zr0.85Ca0.15O1.85, J. Am. Ceram. Soc. 42 (1959) 393–398. doi:10.1111/j.1151-2916.1959.tb13599.x.

[43] K. Ono, T. Oishi, J. Moriyama, Measurements on galvanic cells involving solid-sulphide electrolytes, Solid State Ionics. 3–4 (1981) 555–558. doi:10.1016/0167-2738(81)90150-8.

[44] W. Araki, Y. Arai, J. Malzbender, Transitions of Ba0.5Sr0.5Co0.8Fe0.2O3-δ and La0.58Sr0.4Co0.2Fe0.8O3-δ, Mater. Lett. 132 (2014) 295–297. doi:10.1016/j.matlet.2014.06.093.

[45] B. Huang, J. Malzbender, R.W. Steinbrech, Elastic anomaly and internal friction of Ba0.5Sr0.5Co0.8Fe0.2O3-δ and La0.58Sr0.4Co0.2Fe0.8O3-δ, J. Mater. Res. 26 (2011) 1388–1391. doi:10.1557/jmr.2011.164.

[46] A.S. Bhalla, R. Guo, R. Roy, The perovskite structure -- a review of its role in ceramic science and technology, Mater. Res. Innov. 4 (2000) 3–26. doi:10.1007/s100190000062.

[47] J.E. Miltat, M.J. Donahue, Handbook of Magnetism and Advanced Magnetic Materials, 2007. doi:10.1002/9780470022184.

[48] C. Li, K.C.K. Soh, P. Wu, Formability of ABO3 perovskites, J. Alloys Compd. 372 (2004) 40–48. doi:10.1016/j.jallcom.2003.10.017.

[49] H. Hayashi, H. Inaba, M. Matsuyama, N.G. Lan, M. Dokiya, H. Tagawa, Structural consideration on the ionic conductivity of perovskite-type oxides, Solid State Ionics. 122 (1999) 1–15. doi:10.1016/S0167-2738(99)00066-1.

[50] Wikipedia - Fluorit, (n.d.). https://de.wikipedia.org/wiki/Fluorit.

[51] N.F. Atta, A. Galal, E.H. El-Ads, Perovskite Nanomaterials – Synthesis, Characterization, and Applications, in: L. Pan, G. Zhu (Eds.), Perovskite Mater. - Synth. Characterisation, Prop. Appl., InTech, Rijeka, 2016. doi:10.5772/61280.

[52] M. Schulz, R. Kriegel, W. Burckhardt, Modeling of oxygen flux and stress distribution for Ba0.5Sr0.5Co0.8Fe0.2 O3 membranes at application conditions, in: 10. Intern. Conf. Inorg. Membr., Tokyo, Japan, 2008.

[53] M.W. Barsoum, Fundamentals Of Ceramics, 2003. doi:10.1017/CBO9781107415324.004.

[54] C.B. Carter, M.G. Norton, Ceramic materials : science and engineering, 2nd ed., Springer, New York, 2007. doi:10.1007/978-1-4614-3523-5.

[55] J.D. Lord, R. Morrell, Elastic modulus measurement, Meas. Good Pract. Guid. No. 98, Febr. 2007. (2007). http://www.npl.co.uk/publications/elastic-modulus-measurement.

[56] R. Morrell, Biaxial flexural strength testing of ceramic materials., Meas. Good Pract. Guid. No. 12, December 2007. (2007).

[57] H. Kuhn, D. Medlin, ASM Handbook. Volume 8: Mechanical Testing and Evaluation, 2000. http://www.asminternational.org/web/tss/technical-resources/-/journal_content/56/10192/06772G/PUBLICATION.

[58] G. Roebben, B. Bollen, A. Brebels, J. Van Humbeeck, O. Van der Biest, Impulse excitation apparatus to measure resonant frequencies, elastic moduli, and internal friction at room and high temperature, Rev. Sci. Instrum. 68 (1997) 4511–4515. doi:10.1063/1.1148422.

[59] A.A. Griffith, The Phenomena of Rupture and Flow in Solids, Philos. Trans. R. Soc. A Math. Phys. Eng. Sci. 221 (1921) 163–198. doi:10.1098/rsta.1921.0006.

[60] W. Weibull, A statistical distribution function of wide applicability, J. Appl. Mech. 18 (1951) 293–297. doi:citeulike-article-id:8491543.

[61] D.J. Green, An Introduction to the Mechanical Properties of Ceramics:, Cambridge University Press, Cambridge, 1998. doi:10.1017/CBO9780511623103.

[62] ASTM International, ASTM C1239 - 13, Standard Practice for Reporting Uniaxial Strength Data and Estimating Weibull Distribution Parameters for Advanced Ceramics, ASTM Stand. (2013). doi:10.1520/C1239.

[63] G.G. Chell, R.C. McClung, C.J. Kuhlman, D.A. Russell, K. Garr, B. Donnelly, Guidelines for Proof Test Analysis, (1999). http://ntrs.nasa.gov/search.jsp?R=19990064431 (accessed

October 7, 2016).

[64] T. Okada, I. Kimoto, Improvement of suspension insulator reliability by porcelain proof testing, 1968 8th Electr. Insul. Conf. (1968) 173–176. doi:10.1109/EIC.1968.7456137.

[65] Y. Miyajima, Studies on high-tensile proof tests of optical fibers, J. Light. Technol. 1 (1983) 340–346. doi:10.1109/JLT.1983.1072128.

[66] D.G. Harlow, The effect of proof-testing on the Weibull distribution, J. Mater. Sci. 24 (1989) 1467–1473. doi:10.1007/BF02397087.

[67] J.E. Ritter, P.B. Oates, E.R. Fuller, S.M. Wiederhorn, Proof testing of ceramics, J. Mater. Sci. 15 (1980) 2275–2281. doi:10.1007/BF00552317.

[68] A.G. Evans, E.R. Fuller, Proof testing — the effects of slow crack growth, Mater. Sci. Eng. 19 (1975) 69–77. doi:10.1016/0025-5416(75)90009-9.

[69] J.X. Yi, H.L. Lein, T. Grande, S. Yakovlev, H.J.M. Bouwmeester, High-temperature compressive creep behaviour of the perovskite-type oxide Ba0.5Sr0.5Co0.8Fe0.2O3 - ??, Solid State Ionics. 180 (2009) 1564–1568. doi:10.1016/j.ssi.2009.09.014.

[70] F.R.N. Nabarro, Report on a Conference on Strength of Solids, London, 1948.

[71] C. Herring, Diffusional viscosity of a polycrystalline solid, J. Appl. Phys. 21 (1950) 437–445. doi:10.1063/1.1699681.

[72] P. Colombo, In Praise of Pores, October. 322 (2008) 381–383. doi:10.1126/science.1162962.

[73] K. Meyer, P. Lorenz, B. Bohlkuhn, P. Klobes, Porous Solids and Their Characterization - Methods of Investigation and Application, Cryst. Res. Technol. 29 (1994) 903–930. doi:10.1002/crat.2170290702.

[74] J. Rouquerol, D. Avnir, C.W. Fairbridge, D.H. Everett, J.H. Haynes, N. Pernicone, J.D.F. Ramsay, K.S.W. Sing, K.K. Unger, Recommendations for the characterization of porous solids, Pure Appl. Chem. 66 (1994) 1739–1758. doi:10.1351/pac199466081739.

[75] Y. Zou, J. Malzbender, Development and optimization of porosity measurement techniques, Ceram. Int. 42 (2016) 2861–2870. doi:10.1016/j.ceramint.2015.11.015.

[76] L.J. Gibson, M.F. Ashby, Cellular solids structure and properties, 2nd ed, Cambridge Cambridge University Press, 1997. http://openlibrary.org/books/OL993071M.

[77] M.F. Ashby, R.F.M. Medalist, The mechanical properties of cellular solids, Metall. Trans. A. 14 (1983) 1755–1769. doi:10.1007/BF02645546.

[78] R.W. Rice, Porosity of Ceramics, in: Mater. Eng., 1998: p. Chapter 2.

[79] R.W. Rice, Evaluation and extension of physical property-porosity models based on

minimum solid area, J. Mater. Sci. 31 (1996) 102–118. doi:10.1007/BF00355133.

[80] M. Scheffler, P. Colombo, Cellular Ceramics: Structure, Manufacturing, Properties and Applications, 2006. doi:10.1002/3527606696.

[81] E. RYSHKEWITCH, Compression Strength of Porous Sintered Alumina and Zirconia, J. Am. Ceram. Soc. 36 (1953) 65–68. doi:10.1111/j.1151-2916.1953.tb12837.x.

[82] F.P. KNUDSEN, Dependence of Mechanical Strength of Brittle Polycrystalline Specimens on Porosity and Grain Size, J. Am. Ceram. Soc. 42 (1959) 376–387. doi:10.1111/j.1151-2916.1959.tb13596.x.

[83] R.M. SPRIGGS, Expression for Effect of Porosity on Elastic Modulus of Polycrystalline Refractory Materials, Particularly Aluminum Oxide, J. Am. Ceram. Soc. 44 (1961) 628–629. doi:10.1111/j.1151-2916.1961.tb11671.x.

[84] R.W. RICE, Extension of the Exponential Porosity Dependence of Strength and Elastic Moduli, J. Am. Ceram. Soc. 59 (1976) 536–537. doi:10.1111/j.1151-2916.1976.tb09434.x.

[85] J.C. Wang, Young's modulus of porous materials, J. Mater. Sci. 19 (1984) 801–808. doi:10.1007/BF00540451.

[86] M.F. Ashby, The properties of foams and lattices., Philos. Trans. A. Math. Phys. Eng. Sci. 364 (2006) 15–30. doi:10.1098/rsta.2005.1678.

[87] L.J. Gibson, Modelling the mechanical behavior of cellular materials, Mater. Sci. Eng. A. 110 (1989) 1–36. doi:10.1016/0921-5093(89)90154-8.

[88] L.J. Gibson, M.F. Ashby, G.S. Schajer, C.I. Robertson, The Mechanics of Two-Dimensional Cellular Materials, Proc. R. Soc. A Math. Phys. Eng. Sci. 382 (1982) 25–42. doi:10.1098/rspa.1982.0087.

[89] L.J. Gibson, M.. Ashby, Cellular Solids: structure and properties, 2nd ed., Cambridge University Press, 1997. doi:https://doi.org/10.1017/CBO9781139878326.

[90] A.M. Hodge, D.C. Dunand, Measurement and modeling of creep in open-cell NiAl foams, Metall. Mater. Trans. A. 34 (2003) 2353–2363. doi:10.1007/s11661-003-0298-3.

[91] P.P. Castañeda, The effective mechanical properties of nonlinear isotropic composites, J. Mech. Phys. Solids. 39 (1991) 45–71. doi:10.1016/0022-5096(91)90030-R.

[92] K. Kwok, D. Boccaccini, Å.H. Persson, H.L. Frandsen, Homogenization of steady-state creep of porous metals using three-dimensional microstructural reconstructions, Int. J. Solids Struct. 78–79 (2016) 38–46. doi:10.1016/j.ijsolstr.2015.09.020.

[93] K. Kwok, P.S. Jørgensen, H.L. Frandsen, Computation of Effective Steady-State Creep of Porous Ni-YSZ Composites with Reconstructed Microstructures, J. Am. Ceram. Soc. 98 (2015) 2873–2880. doi:10.1111/jace.13712.

[94] L.W. Tai, M.M. Nasrallah, H.U. Anderson, D.M. Sparlin, S.R. Sehlin, Structure and electrical properties of La1-xSrxCo1-yFeyO3. Part 1. The system La0.8Sr0.2Co1-yFeyO3, Solid State Ionics. 76 (1995) 259–271. doi:10.1016/0167-2738(94)00244-M.

[95] A. Mineshige, J. Izutsu, M. Nakamura, K. Nigaki, J. Abe, M. Kobune, S. Fujii, T. Yazawa, Introduction of A-site deficiency into La0.6Sr 0.4Co0.2Fe0.8O3-δ and its effect on structure and conductivity, Solid State Ionics. 176 (2005) 1145–1149. doi:10.1016/j.ssi.2004.11.021.

[96] S. Wang, High temperature properties of La0.6Sr0.4Co0.8Fe0.2O3−δ phase structure and electrical conductivity, Solid State Ionics. 159 (2003) 71–78. doi:10.1016/S0167-2738(03)00027-4.

[97] J. MIZUSAKI, T. SASAMOTO, W.R. CANNON, H.K. BOWEN, Electronic Conductivity, Seebeck Coefficient, and Defect Structure of La1???xSrxFeO3 (x=0.l, 0.25), J. Am. Ceram. Soc. 66 (1983) 247–252. doi:10.1111/j.1151-2916.1983.tb15707.x.

[98] W. Araki, J. Malzbender, Ferroelastic deformation of La0.58Sr0.4Co0.2Fe0.8O3-?? under uniaxial compressive loading, J. Eur. Ceram. Soc. 33 (2013) 805–812. doi:10.1016/j.jeurceramsoc.2012.10.035.

[99] W. Araki, T. Yamaguchi, Y. Arai, J. Malzbender, Strontium surface segregation in La0.58Sr0.4Co0.2Fe0.8O3 -δ annealed under compression., Solid State Ionics. 268 (2014) 1–6. doi:10.1016/j.ssi.2014.09.019.

[100] B.X. Huang, J. Malzbender, R.W. Steinbrech, L. Singheiser, Mechanical properties of La0.58Sr0.4Co0.2Fe0.8O3 -δ membranes, Solid State Ionics. 180 (2009) 241–245. doi:10.1016/j.ssi.2008.11.005.

[101] B.X. Huang, R.W. Steinbrech, J. Malzbender, Direct observation of ferroelastic domain effects in LSCF perovskites, Solid State Ionics. 228 (2012) 32–36. doi:10.1016/j.ssi.2012.08.025.

[102] B.X. Huang, R.W. Steinbrech, S. Baumann, J. Malzbender, Creep behavior and its correlation with defect chemistry of La0.58Sr0.4Co0.2Fe0.8O3−δ, Acta Mater. 60 (2012) 2479–2484. doi:10.1016/j.actamat.2011.12.025.

[103] a Fossdal, M. Menon, I. Waernhus, K. Wiik, M. a Einarsrud, T. Grande, Crystal structure and thermal expansion of La1-xSrxFeO3-delta, J. Am. Ceram. Soc. 87 (2004) 1952–1958. doi:10.1134/S0036023613100148.

[104] J.C. Grenier, N. Ea, M. Pouchard, P. Hagenmuller, Structural transitions at high temperature in Sr2Fe2O5, J. Solid State Chem. 58 (1985) 243–252. doi:10.1016/0022-4596(85)90241-5.

[105] B.X. Huang, J. Malzbender, R.W. Steinbrech, E. Wessel, H.J. Penkalla, L. Singheiser, Mechanical aspects of ferro-elastic behavior and phase composition of

La0.58Sr0.4Co0.2Fe0.8O3-??, J. Memb. Sci. 349 (2010) 183–188. doi:10.1016/j.memsci.2009.11.047.

[106] P. Müllner, W.M. Kriven, On the role of deformation twinning in domain reorganization and grain reorientation in ferroelastic crystals, J. Mater. Res. 12 (1997) 1771–1776. doi:10.1557/JMR.1997.0244.

[107] K. Kleveland, N. Orlovskaya, T. Grande, A.M.M. Moe, M. Einarsrud, K. Breder, G. Gogotsi, Ferroelastic Behavior of LaCoO3-Based Ceramics, J. Am. Ceram. Soc. 84 (2004) 2029–2033. doi:10.1111/j.1151-2916.2001.tb00953.x.

[108] W. Araki, J. Malzbender, Ferroelastic deformation of La0.58Sr0.4Co0.2Fe0.8O3-delta under uniaxial compressive loading, J. Eur. Ceram. Soc. 33 (2013) 805–812. doi:10.1016/j.jeurceramsoc.2012.10.035.

[109] Y.-S. Chou, J.W. Stevenson, T.R. Armstrong, L.R. Pederson, Mechanical Properties of La1-xSrxCo0.2Fe0.8O3 Mixed-Conducting Perovskites Made by the Combustion Synthesis Technique, J. Am. Ceram. Soc. 83 (2000) 1457–1464. doi:10.1111/j.1151-2916.2000.tb01410.x.

[110] Y. Kimura, T. Kushi, S. Hashimoto, K. Amezawa, T. Kawada, Influences of Temperature and Oxygen Partial Pressure on Mechanical Properties of La0.6Sr0.4Co1-yFeyO3-d, J. Am. Ceram. Soc. 95 (2012) 2608–2613. doi:10.1111/j.1551-2916.2012.05265.x.

[111] M. Lipińska-Chwałek, F. Schulze-Küppers, J. Malzbender, Strength and elastic modulus of Lanthanum strontium cobalt ferrite membrane materials, Ceram. Int. 41 (2015) 1355–1360. doi:10.1016/j.ceramint.2014.09.068.

[112] Z. Chen, X. Wang, V. Bhakhri, F. Giuliani, A. Atkinson, Nanoindentation of porous bulk and thin films of La0.6Sr0.4Co0.2Fe0.8O3−δ, Acta Mater. 61 (2013) 5720–5734. doi:10.1016/j.actamat.2013.06.016.

[113] Z. Chen, X. Wang, F. Giuliani, A. Atkinson, Microstructural characteristics and elastic modulus of porous solids, Acta Mater. 89 (2015) 268–277. doi:10.1016/j.actamat.2015.02.014.

[114] D.R. Thompson, L.E. Bool, J.C. Chen, Oxygen enhanced combustion for NOx control, 2004.

[115] B. Rutkowski, J. Malzbender, T. Beck, R.W. Steinbrech, L. Singheiser, Creep behaviour of tubular Ba0.5Sr0.5Co0.8Fe0.2O3-δ gas separation membranes, J. Eur. Ceram. Soc. 31 (2011) 493–499. doi:10.1016/j.jeurceramsoc.2010.10.030.

[116] B. Rutkowski, J. Malzbender, R.W. Steinbrech, T. Beck, H.J.M. Bouwmeester, Influence of thermal history on the cubic-to-hexagonal phase transformation and creep behaviour of Ba0.5Sr0.5Co0.8Fe0.2O3−δ ceramics, J. Memb. Sci. 381 (2011) 221–225. doi:10.1016/j.memsci.2011.07.036.

[117] M. Lipińska-Chwałek, G. Pećanac, J. Malzbender, Creep behaviour of membrane and

substrate materials for oxygen separation units, J. Eur. Ceram. Soc. 33 (2013) 1841–1848. doi:10.1016/j.jeurceramsoc.2013.02.007.

[118] V. Stournari, S.F.P. ten Donkelaar, J. Malzbender, T. Beck, L. Singheiser, H.J.M. Bouwmeester, Creep behavior of perovskite-type oxides Ba0.5Sr0.5(Co0.8Fe0.2)1−xZrxO3−δ, J. Eur. Ceram. Soc. 35 (2015) 1841–1846. doi:https://doi.org/10.1016/j.jeurceramsoc.2015.01.005.

[119] T.H. Etsell, S.N. Flengas, Electrical properties of solid oxide electrolytes, Chem. Rev. 70 (1970) 339–376. doi:10.1021/cr60265a003.

[120] P. Yashar, J. Rechner, M.S. Wong, W.D. Sproul, S.A. Barnett, High-rate reactive sputtering of yttria-stabilized zirconia using pulsed d.c. power, Surf. Coatings Technol. 94–95 (1997) 333–338. doi:10.1016/S0257-8972(97)00270-3.

[121] B.C. Steele, A. Heinzel, Materials for fuel-cell technologies., Nature. 414 (2001) 345–352. doi:10.1038/35104620.

[122] T. Liu, X. Zhang, L. Yuan, J. Yu, A review of high-temperature electrochemical sensors based on stabilized zirconia, Solid State Ionics. 283 (2015) 91–102. doi:10.1016/j.ssi.2015.10.012.

[123] X. Liang, S. Yang, J. Li, H. Zhang, Q. Diao, W. Zhao, G. Lu, Mixed-potential-type zirconia-based NO2 sensor with high-performance three-phase boundary, Sensors Actuators, B Chem. 158 (2011) 1–8. doi:10.1016/j.snb.2011.02.051.

[124] X. Zhong, H. Zhao, X. Zhou, C. Liu, L. Wang, F. Shao, K. Yang, S. Tao, C. Ding, Thermal shock behavior of toughened gadolinium zirconate/YSZ double-ceramic-layered thermal barrier coating, J. Alloys Compd. 593 (2014) 50–55. doi:10.1016/j.jallcom.2014.01.060.

[125] D.R. Clarke, S.R. Phillpot, Thermal barrier coating materials, Mater. Today. 8 (2005) 22–29. doi:10.1016/S1369-7021(05)70934-2.

[126] N. Miura, T. Sato, S.A. Anggraini, H. Ikeda, S. Zhuiykov, A review of mixed-potential type zirconia-based gas sensors, Ionics (Kiel). 20 (2014) 901–925. doi:10.1007/s11581-014-1140-1.

[127] S. BLOCK, J.A.H. DA JORNADA, G.J. PIERMARINI, Pressure-Temperature Phase Diagram of Zirconia, J. Am. Ceram. Soc. 68 (1985) 497–499. doi:10.1111/j.1151-2916.1985.tb15817.x.

[128] Y. Shen, S. Shao, H. Yu, Z. Fan, H. He, J. Shao, Influences of oxygen partial pressure on structure and related properties of ZrO2 thin films prepared by electron beam evaporation deposition, Appl. Surf. Sci. 254 (2007) 552–556. doi:10.1016/j.apsusc.2007.06.029.

[129] R.H.J. Hannink, P.M. Kelly, B.C. Muddle, Transformation Toughening in Zirconia-Containing Ceramics, J. Am. Ceram. Soc. 83 (2000) 461–487. doi:10.1111/j.1151-2916.1987.tb04865.x.

[130] S.P.S. Badwal, Zirconia-based solid electrolytes: microstructure, stability and ionic conductivity, Solid State Ionics. 52 (1992) 23–32. doi:10.1016/0167-2738(92)90088-7.

[131] J. Chevalier, L. Gremillard, A. V. Virkar, D.R. Clarke, The tetragonal-monoclinic transformation in zirconia: Lessons learned and future trends, J. Am. Ceram. Soc. 92 (2009) 1901–1920. doi:10.1111/j.1551-2916.2009.03278.x.

[132] S.R. and A.H. N. Christiansen, S. Primdahl, M. Wandel, Status of the Solid Oxide Fuel Cell Development at Topsoe Fuel Cell A/S and DTU Energy Conversion N. Christiansen, ECS Trans. 57 (2013) 43–52. doi:10.1149/05701.0043ecst.

[133] H.G. Scott, Phase relationships in the zirconia-yttria system, J. Mater. Sci. 10 (1975) 1527–1535. doi:10.1007/BF01031853.

[134] E.C. Subbarao, Zirconia, An Overview, in: Sci. Technol. Zirconia, 1981: pp. 1–24.

[135] T.K. Gupta, F.F. Lange, J.H. Bechtold, Effect of stress-induced phase transformation on the properties of polycrystalline zirconia containing metastable tetragonal phase, J. Mater. Sci. 13 (1978) 1464–1470. doi:10.1007/BF00553200.

[136] a. Selçuk, a. Atkinson, Elastic properties of ceramic oxides used in solid oxide fuel cells (SOFC), J. Eur. Ceram. Soc. 17 (1997) 1523–1532. doi:10.1016/S0955-2219(96)00247-6.

[137] J. Seuba, S. Deville, C. Guizard, A.J. Stevenson, Mechanical properties and failure behavior of unidirectional porous ceramics, Sci. Rep. 6 (2016) 24326. http://dx.doi.org/10.1038/srep24326.

[138] J. Seuba, S. Deville, C. Guizard, A.J. Stevenson, The effect of wall thickness distribution on mechanical reliability and strength in unidirectional porous ceramics, Sci. Technol. Adv. Mater. 17 (2016) 128–135. doi:10.1080/14686996.2016.1140309.

[139] T.G. Nieh, J. Wadsworth, O.D. Sherby, Superplasticity in Metals and Ceramics, Cambridge University Press, 2005. https://books.google.de/books?id=AdRnwSSbHPoC.

[140] I. Charit, A.H. Chokshi, Experimental evidence for diffusion creep in the superplastic 3 mol% yttria-stabilized tetragonal zirconia, Acta Mater. 49 (2001) 2239–2249. doi:10.1016/S1359-6454(01)00131-8.

[141] A.H. Chokshi, The role of diffusion creep in the superplastic deformation of 3 mol% yttria stabilized tetragonal zirconia, Scr. Mater. 42 (2000) 241–248. doi:https://doi.org/10.1016/S1359-6462(99)00340-1.

[142] D.M. Owen, A.H. Chokshi, The high temperature mechanical characteristics of superplastic 3 mol% yttria stabilized zirconia, Acta Mater. 46 (1998) 667–679. doi:10.1016/S1359-6454(97)00251-6.

[143] K. Morita, K. Hiraga, Critical assessment of high-temperature deformation and deformed microstructure in high-purity tetragonal zirconia containing 3 mol.% yttria, Acta Mater.

50 (2002) 1075–1085. doi:10.1016/S1359-6454(01)00407-4.

[144] A.H. Chokshi, A.K. Mukherjee, T.G. Langdon, Superplasticity in advanced materials, Mater. Sci. Eng. R. 10 (1993) 237–274. doi:10.1016/0927-796X(93)90009-R.

[145] M.S. SELTZER, P.K. TALTY, High-Temperature Creep of Y2O3-Stabilized ZrO2, J. Am. Ceram. Soc. 58 (1975) 124–130. doi:10.1111/j.1151-2916.1975.tb19574.x.

[146] M. Jiménez-Melendo, A. Domínguez-Rodríguez, A. Bravo-León, Superplastic Flow of Fine-Grained Yttria-Stabilized Zirconia Polycrystals: Constitutive Equation and Deformation Mechanisms, J. Am. Ceram. Soc. 81 (1998) 2761–2776. doi:10.1111/j.1151-2916.1998.tb02695.x.

[147] A. Morales-Rodríguez, A. Bravo-León, A. Domínguez-Rodríguez, S. López-Esteban, J.S. Moya, M. Jiménez-Melendo, High-temperature mechanical properties of zirconia/nickel composites, J. Eur. Ceram. Soc. 23 (2003) 2849–2856. doi:10.1016/S0955-2219(03)00309-1.

[148] J. Laurencin, G. Delette, F. Usseglio-Viretta, S. Di Iorio, Creep behaviour of porous SOFC electrodes: Measurement and application to Ni-8YSZ cermets, J. Eur. Ceram. Soc. 31 (2011) 1741–1752. doi:10.1016/j.jeurceramsoc.2011.02.036.

[149] Y. Ma, T.G. Langdon, An Investigation of the Mechanical Behavior of a Superplastic Yttria-Stabilized Zirconia, MRS Proc. 196 (1990). doi:DOI: 10.1557/PROC-196-325.

[150] F.S.-K. W. Schafbauer S. Baumann, W.A. Meulenberg, N.H. Menzler, H.P. Buchkremer and D. Stöver, Tape Casting as a Multi Purpose Shaping Technology for Different Applications in Energy Issues, Mater. Sci. Forum. 706–709 (2012) 1035–1040. doi:10.4028/www.scientific.net/MSF.706-709.1035.

[151] P. Niehoff, F. Schulze-Küppers, S. Baumann, W.A. Meulenberg, O. Guillon, R. Vaßen, Fabrication of laboratory-scale planar oxygen separation membrane modules, Am. Ceram. Soc. Bull. 94 (2015) 28–31.

[152] C. Gaudillere, J. Garcia-Fayos, J.M. Serra, Oxygen permeation improvement under CO2-rich environments through catalytic activation of hierarchically structured perovskite membranes, Chempluschem. 79 (2014) 1720–1725. doi:10.1002/cplu.201402142.

[153] C. Gaudillere, J. Garcia-Fayos, M. Balaguer, J.M. Serra, Enhanced Oxygen Separation through Robust Freeze-Cast Bilayered Dual-Phase Membranes, ChemSusChem. (2014). doi:10.1002/cssc.201402324.

[154] S. Deville, E. Maire, A. Lasalle, A. Bogner, C. Gauthier, J. Leloup, C. Guizard, In situ X-ray radiography and tomography observations of the solidification of aqueous alumina particle suspensions - Part I: Initial instants, J. Am. Ceram. Soc. 92 (2009) 2489–2496. doi:10.1111/j.1551-2916.2009.03163.x.

[155] A. Lichtner, D. Roussel, D. Jauffrès, C.L. Martin, R.K. Bordia, Effect of Macropore

Anisotropy on the Mechanical Response of Hierarchically Porous Ceramics, J. Am. Ceram. Soc. 99 (2016) 979–987. doi:10.1111/jace.14004.

[156] ASTM International, ASTM C1499 - 05 Standard Test Method for Monotonic Equibiaxial Flexural Strength of Advanced Ceramics at Ambient Temperature, ASTM Stand. (2005). doi:10.1520/C1499-05.

[157] DIN51105:2010-08 Hochleistungskeramik - Mechanische Eigenschaften monolithischer Keramik bei Raumtemperatur - Bestimmung der Doppelring-Biegefestigkeit, Dtsch. NORM. (2010).

[158] ASTM International, ASTM C1161-13, Standard Test Method for Flexural Strength of Advanced Ceramics at Ambient Temperature, ASTM Stand. (2013). doi:10.1520/C1161.

[159] B. Rutkowski, {M}echanical properties and microstructure of dense ceramic membranes for oxygen separation in zero-emission power plants, Wydawnictwo Naukowe AKAPIT, 2013. http://publications.rwth-aachen.de/record/211861.

[160] G. Pećanac, L. Kiesel, J. Malzbender, Steady-state creep of porous and an extended analysis on the creep of dense BSCFZ perovskite, J. Memb. Sci. 456 (2014) 134–138. doi:10.1016/j.memsci.2014.01.021.

[161] C. Gaudillere, J. Garcia-Fayos, J.M. Serra, Enhancing oxygen permeation through hierarchically-structured perovskite membranes elaborated by freeze-casting, J. Mater. Chem. A. 2 (2014) 3828. doi:10.1039/c3ta14069e.

[162] M.M. Woolfson, An Introduction to X-Ray Crystallography, 2nd ed., Cambridge University Press, 1997. doi:10.1017/CBO9780511622557.

[163] Development of X-ray crystallography, 2017 Univ. Illinois Board Trust. (2017). https://publish.illinois.edu/x-raycrystallography/.

[164] G. Bergerhoff, I.D. Brown, Crystallographic Databases, Data Commission of the International Union of Crystallography, 1987.

[165] A. Belsky, M. Hellenbrandt, V.L. Karen, P. Luksch, New developments in the Inorganic Crystal Structure Database (ICSD): accessibility in support of materials research and design, Acta Crystallogr. Sect. B. 58 (2002) 364–369. doi:10.1107/S0108768102006948.

[166] B. Hafner, Scanning Electron Microscopy Primer, Univ. Minnesota. (2007). http://www.charfac.umn.edu/instruments/sem_primer.pdf.

[167] J. Schindelin, I. Arganda-Carreras, E. Frise, V. Kaynig, M. Longair, T. Pietzsch, S. Preibisch, C. Rueden, S. Saalfeld, B. Schmid, J.-Y. Tinevez, D.J. White, V. Hartenstein, K. Eliceiri, P. Tomancak, A. Cardona, Fiji: an open-source platform for biological-image analysis, Nat Meth. 9 (2012) 676–682.

[168] X. Chen, T. Grande, Anisotropic Chemical Expansion of La1–xSrxCoO3−δ, Chem. Mater.

25 (2013) 927–934. doi:10.1021/cm304040p.

[169] G. Pećanac, S. Baumann, J. Malzbender, Mechanical properties and lifetime predictions for Ba0.5Sr0.5Co0.8Fe0.2O3-δ membrane material, J. Memb. Sci. 385–386 (2011) 263–268. doi:10.1016/j.memsci.2011.10.005.

[170] S.P. Jiang, X. Chen, Chromium deposition and poisoning of cathodes of solid oxide fuel cells - A review, Int. J. Hydrogen Energy. 39 (2014) 505–531. doi:10.1016/j.ijhydene.2013.10.042.

[171] P.A.W. Van Der Heide, Systematic x-ray photoelectron spectroscopic study of La1-xSrx-based perovskite-type oxides, Surf. Interface Anal. 33 (2002) 414–425. doi:10.1002/sia.1227.

[172] G. Majkic, Stress-induced diffusion and defect chemistry of La0.2Sr0.8Fe0.8Cr0.2O3−δ 2. Structural, elemental and chemical analysis, Solid State Ionics. 167 (2004) 243–254. doi:10.1016/j.ssi.2003.12.022.

[173] F.-K. Zhuang, S.-T. Tu, G.-Y. Zhou, Q.-Q. Wang, Assessment of creep constitutive properties from three-point bending creep test with miniaturized specimens, J. Strain Anal. Eng. Des. 49 (2014) 482–491. doi:10.1177/0309324714537056.

[174] S. Deville, Freeze-casting of porous ceramics: A review of current achievements and issues, in: Adv. Eng. Mater., 2008: pp. 155–169. doi:10.1002/adem.200700270.

[175] S. Deville, C. Viazzi, C. Guizard, Ice-Structuring Mechanism for Zirconium Acetate, Langmuir. 28 (2012) 14892–14898. doi:10.1021/la302275d.

[176] J.W. Fergus, Electrolytes for solid oxide fuel cells, J. Power Sources. 162 (2006) 30–40. doi:10.1016/j.jpowsour.2006.06.062.

[177] D.W. STRICKLER, W.G. CARLSON, Ionic Conductivity of Cubic Solid Solutions in the System CaO-Y2O3-ZrO2, J. Am. Ceram. Soc. 47 (1964) 122–127. doi:10.1111/j.1151-2916.1964.tb14368.x.

[178] J.M. Dixon, L.D. LaGrange, U. Merten, C.F. Miller, J.T. Porter II, Electrical Resistivity of Stabilized Zirconia at Elevated Temperatures, J. Electrochem. Soc. 110 (1963) 276–280.

[179] M. Roos, C. Schatz, B. Stawarczyk, Two Independent Prospectively Planned Blinded Weibull Statistical Analyses of Flexural Strength Data of Zirconia Materials, Materials (Basel). 9 (2016) 512. doi:10.3390/ma9070512.

[180] J. Zhang, J. Malzbender, Mechanical characterization of micro- and nano-porous alumina, Ceram. Int. 41 (2015) 10725–10729. doi:10.1016/j.ceramint.2015.05.007.

Publications & Conference

Y. Zou, F. Schulze-Kuppers, J. Malzbender, Creep behavior of porous $La_{0.6}Sr_{0.4}Co_{0.2}Fe_{0.8}O_{3-\sigma}$ oxygen transport membrane supports, Ceramics International 41 (2015) 4064 – 4069.

Y. Zou, J. Malzbender, Development and optimization of porosity measurement techniques, Ceramics International 42 (2016) 2861 – 2870.

Y. Zou, Wakako Araki, Maria Balaguer, Jürgen Malzbender, Elastic properties of freeze-cast $La_{0.6}Sr_{0.4}Co_{0.2}Fe_{0.8}O_{3-\sigma}$, Journal of the European Ceramic Society 36 (2016) 1651–1657.

Y. Zou, Wakako Araki, Maria Balaguer, Jürgen Malzbender, Elastic properties of freeze-cast $La_{0.6}Sr_{0.4}Co_{0.2}Fe_{0.8}O_{3-\sigma}$ (Poster), 229th ECS meeting, San Diego, USA, 2016.

Y. Zou, C. Gaudillere, J. M. Serra, J. Malzbender, Microstructure, Mechanical behavior and Flow Resistance of Freeze Cast Porous 3YSZ Substrates for Membrane Applications, Journal of the European Ceramic Society 37 (2017) 3167–3176.

Y. Zou, F. Schulze-Kuppers, M. Balaguer, J. Malzbender, Thermomechanical characterization of porous LSCF with different pore structures and porosity (Oral presentation), ICACC 2017, Daytona Beach, USA, 2017.

Curriculum Vitae

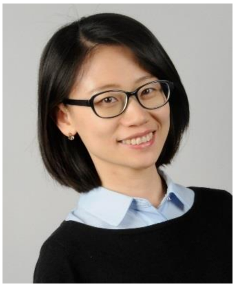

Ying Zou

Data of Birth:	04. Nov. 1987
Place of Birth:	Shandong, China
Nationality:	Chinese

Education:

Ph.D. in **Mechanical Engineering**
Dissertation: "Thermomechanical characterization of oxygen transport membrane materials for energy efficient new generation carbon capture process"
Forschungszentrum Jülich GmbH & RWTH Aachen, Germany
03.2014 – 08.2017

M.Sc. in **Physical Metallurgy and Materials**
RWTH Aachen, Germany
09.2010 – 11.2013

B.Sc. in **Materials Science and Engineering**
University of Science and Technology Beijing (USTB), China
09.2006 – 07.2010

Practice and Project Experience:

PhD Project	PhD work involved and financially supported by project "GREEN-CC" under European Union's Research and Innovation funding programme FP7. **Forschungszentrum Jülich GmbH, Germany** *03.2014 – 08.2017*
Scientific Visit	**Saitama University, Japan** *05.2015 – 06.2015*
Industrial Internship	**Philips Business Center Automotive Aachen, Germany** *03.2012 – 12.2012*

Band / Volume 390
Potential use of nitrification inhibitors for mitigating N_2O emission from soils
D. Wu (2017), 206 pp
ISBN: 978-3-95806-264-1

Band / Volume 391
Mechanical Characterization of Solid Oxide Fuel Cells and Sealants
J. Wei (2017), II, 151 pp
ISBN: 978-3-95806-266-5

Band / Volume 392
Microcrystalline Silicon Carbide for Silicon Heterojunction Solar Cells
M. B. Pomaska (2017), 150 pp
ISBN: 978-3-95806-267-2

Band / Volume 393
Einfluss der Kristallisation auf das Fließverhalten oxidischer Schmelzen
S. Seebold (2017), 168 pp
ISBN: 978-3-95806-268-9

Band / Volume 394
Water vapour in the UTLS – Climatologies and Transport
P. R. Neis (2017), x, 124 pp
ISBN: 978-3-95806-269-6

Band / Volume 395
Neutronenaktivierungsanalyse mit gepulsten 14 MeV Neutronen zur Charakterisierung heterogener radioaktiver Abfälle
F. Mildenberger (2017), vi, 128 pp
ISBN: 978-3-95806-271-9

Band / Volume 396
Coupled biotic-abiotic mechanisms of nitrous oxide production in soils during nitrification involving the reactive intermediates hydroxylamine and nitrite
S. Liu (2017), xvii, 148 pp
ISBN: 978-3-95806-272-6

Band / Volume 397
Mixed-phase and ice cloud observations with NIXE-CAPS
A. Costa (2017), xviii, 117 pp
ISBN: 978-3-95806-273-3

Band / Volume 398
Deposition Mechanisms of Thermal Barrier Coatings (TBCs) Manufactured by Plasma Spray-Physical Vapor Deposition (PS-PVD)
W. He (2017), ix, 162 pp
ISBN: 978-3-95806-275-7

Band / Volume 399
Carbonyl Sulfide in the Stratosphere: airborne instrument development and satellite based data analysis
C. Kloss (2017), vi, 84, 1-14 pp
ISBN: 978-3-95806-276-4

Band / Volume 400
Lagrangian transport of trace gases in the upper troposphere and lower stratosphere (UTLS)
P. Konopka (2017), 70 pp
ISBN: 978-3-95806-279-5

Band / Volume 401
Numerical Simulation of Plasma Spray-Physical Vapor Deposition
P. Wang (2017), IX, 127 pp
ISBN: 978-3-95806-282-5

Band / Volume 402
The Selective Separation of Am(III) from Highly Radioactive PUREX Raffinate
P. Kaufholz (2017), IV, 173 pp
ISBN: 978-3-95806-284-9

Band / Volume 403
Spatio-Temporal Estimation and Validation of Remotely Sensed Vegetation and Hydrological Fluxes in the Rur Catchment, Germany
M. Ali (2018), xvi, 116 pp
ISBN: 978-3-95806-287-0

Band / Volume 404
Thermomechanical Characterization of Advanced Ceramic Membrane Materials
Y. Zou (2018), xviii, 168 pp
ISBN: 978-3-95806-288-7

Weitere ***Schriften des Verlags im Forschungszentrum Jülich*** unter
http://wwwzb1.fz-juelich.de/verlagextern1/index.asp

Energie & Umwelt / Energy & Environment
Band / Volume 404
ISBN 978-3-95806-288-7

Mitglied der Helmholtz-Gemeinschaft

JÜLICH
Forschungszentrum